Kallåk, Vetle

Parametric Design and Analysis of Wave-Induced Responses of a Semi-Submersible Floating Wind Turbine Platform

Master's thesis

NTNU
Norwegian University of
Science and Technology

Kallåk, Vetle

Parametric Design and Analysis of Wave-Induced Responses of a Semi-Submersible Floating Wind Turbine Platform

Master's thesis in Marine Technology
Supervisor: Bachynski, Erin
June 2020

Norwegian University of Science and Technology
Faculty of Engineering
Department of Marine Technology

NTNU
Norwegian University of
Science and Technology

Summary

This thesis explores how the change of specific design parameters impact the wave-induced motions and internal hull loads of a semi-submersible floating 10 MW wind turbine platform. The purpose of the investigation is to optimize the hull form to minimize cost, while complying with strength and safety requirements. The need for more sustainable energy sources is increasing. Offshore wind brings several advantages over onshore, and recent studies show that the potential for harvesting offshore wind energy is huge. Most of this potential comes from deep water sites, where floating structures are advantageous. However, for floating wind to compete with other energy sources it needs to be cost-competitive. Therefore, a parametric study is carried out to better understand how the design parameters influence the responses of the structure and how the design could be improved.

The WindFloat semi-submersible platform was chosen as the baseline design for the study and upscaled to support a 10 MW reference wind turbine. In this study, the hull was parameterized by defining four main dimensions: 1) the column diameter, 2) the draft, 3) the distance between the columns, and 4) the heave plate size. Also, the effect of a wind-induced mean tilt angle on the responses was investigated.

The first-order potential theory program *Wadam* was used to calculate the hydrodynamic added mass, damping, and excitation loads on the columns and heave plates. The mass and restoring properties were calculated in *MATLAB*. To simplify calculations, the motions and internal hull loads were calculated in the frequency domain. The hydrodynamic loads on the truss members connecting the columns and viscous loads on the heave plates were included by linearizing Morison's equation. Evaluating one parameter at the time, the influence on the hydrostatic properties and wave-induced responses was studied. The standard deviations of the motions, nacelle accelerations, and internal hull loads for each design and three environmental conditions were used to compare the designs.

The most significant finding from the parametric study shows that a 28 % reduction in steel mass can be achieved by: 1) reduce the column diameter and heave plate size, 2) increase the distance between the columns, and 3) reduce the draft. Further, the improved design has lower internal loads, similar motions, and slightly higher nacelle accelerations compared to the initial upscaled design. A smaller column diameter and a larger distance between the columns reduces the steel mass while still counteracting the overturning moment from the wind turbine thrust. Increasing the distance between the columns did not result in a higher bending moment in the cross-section. It should be noted that a rigid body is assumed, and the truss members were not included in the sectional load analysis. A smaller column diameter increases the heave and pitch motions and nacelle accelerations. However, the heave plates could then also be reduced in size while keeping the heave natural period outside the wave energy range. Smaller heave plates decrease motions and nacelle accelerations more than by increasing the column diameter. Both reducing the column diameter and heave plate size decrease the cross-sectional bending moment. Increasing the draft is the most efficient parameter for reducing the motions and nacelle acceleration, at the cost of increased steel mass and higher split forces between the columns.

The most important finding from the mean tilt analysis shows a 31 % increase in the nacelle acceleration standard deviation when analyzing the structure with a -10 degrees tilt angle. The potential wave loads are sensitive to the vertical displacement of the heave plates when the platform is tilted, especially at higher frequencies in the wave energy range. The heave force was doubled for a wave frequency of one rad/s when the platform was tilted 10 degrees.

Sammendrag

Denne masteroppgaven undersøker hvordan endringer av ulike design parametere påvirker bevegelsene og de interne lastene fra bølger til en halvt nedsenkbar flytende 10 MW vindturbin. Hensikten med undersøkelsen er å optimere skroget med tanke på kostnad, mens krav til styrke og sikkerhet er overholdt. Det er et økende behov for fornybar energi. Havvind har flere fordeler i forhold til landbasert, og nyere studier viser at potensialet er enormt. Mesteparten av dette potensialet er fra områder med dypt vann, hvor flytende strukturer er fordelaktig. For at flytende havvind skal kunne konkurrere med andre energikilder må det være konkurransedyktig på pris. En parameterstudie er derfor gjennomført for å bedre forstå hvordan design parameterne påvirker oppførselen til strukturen og hvordan designet kan forbedres.

Den halvt nedsenkbare WindFloat plattformen ble valgt som grunndesign og ble oppskalert for å bære en 10 MW referanse vindturbin. I studien har skroget blitt gjort parametrisk ved å definere fire hoveddimensjoner: 1) søylediameteren, 2) dypgangen, 3) avstanden mellom søylene og 4) størrelsen på hivplatene. I tillegg har effekten av en vindindusert krengevinkel på oppførselen til plattformen blitt undersøkt.

Førsteordens, potensialteori programmet *Wadam* ble brukt for å beregne hydrodynamisk tilleggsmasse, demping og eksitasjons laster på søylene og hivplatene. Masse- og stivhetsegenskapene ble beregnet i *MATLAB*. For å forenkle beregningene ble bevegelsene og de interne lastene beregnet i frekvensdomenet. De hydrodynamiske lastene på bjelkene mellom søylene og de viskøse kreftene på hivplatene ble inkludert ved linearisering av Morisons likning. Ved å evaluere en parameter av gangen, ble påvirkningen på de hydrostatiske og bølgeinduserte responsene til strukturen studert. Standardavviket til bevegelsene, nacelle akselerasjonene og de interne lastene for hvert design og tre ulike sjøtilstander ble brukt for å sammenligne plattformene.

Den viktigste funnet fra parameterstudien er at stålmassen kan reduseres med 28 % ved å: 1) redusere søylediameteren og hivplate størrelsen, 2) øke avstanden mellom søylene, og 3) redusere dypgangen. Det forbedrede designet har lavere interne laster, like bevegelser og litt høyere akselerasjoner i nacellen i forhold til det første, oppskalerte designet. En lavere søylediameter og større avstand mellom søylene reduserer stålvekten, mens plattformen opprettholder nok stivhet til å motvirke momentet fra vindturbinen. Å øke avstanden mellom søylene ga ikke større bøyemoment i tverrsnittet. Det skal nevnes at stivt legeme er antatt og bjelkene mellom søylene var ikke med i beregningene av interne laster. En mindre søylediameter øker hiv og stamp bevegelsene og nacelle akselerasjonene. Imidlertid, kan da også hivplatene reduseres i størrelse mens hiv egenperioden holdes utenfor bølgeenergi området. Mindre hivplater minker bevegelsene og nacelle akselerasjonene mer enn ved å øke søylediameteren. Både mindre søylediameter og hivplater reduserer bøyemomentet i tverrsnittet. Å øke dypgangen er det mest effektive for å redusere bevegelsene og nacelle akselerasjonene, på bekostning av mer stål og høyere splittkrefter mellom søylene.

Det viktigste funnet fra analysene med krengevinkel ga 31 % økning i standardavviket til nacelle akselerasjonene når en krengevinkel på -10 grader ble brukt. Potensial bølgekreftene er følsomme for endringer i dypgangen til hivplatene når plattformen krenger, spesielt ved høyere frekvenser i bølgeenergi området. Kraften i hiv-retning ble doblet ved en bølgefrekvens på en rad/s når plattformen ble krenget 10 grader.

Preface

This master's thesis is written as the final work of the five-years master's degree program Marine Technology at the Norwegian University of Science and Technology (NTNU). The master's thesis is written during the spring semester of 2020. I have found the topic of floating wind turbines very interesting and see great potential for this technology. Through the parametric study, I have gained a deeper understanding of the hydrodynamics of floating wind turbine hulls, which I hope will be valuable knowledge in my future work career.

Special gratitude goes out to Professor Erin Bachynski at NTNU for guidance and supervising during the master's thesis work the spring of 2020. Our weekly meetings, first at the office and then online due to the COVID-pandemic, are much appreciated. I am very grateful for the knowledge Professor Bachynski has shared about floating wind turbines and the use of different software. I am also thankful for the discussions and feedback I have received about the thesis.

I would also like to thank Jørgen Kvaleid, COWI, for introducing the topic of floating wind turbines and for sharing valuable information concerning general hydrodynamics related to the topic. I hope to be able to explore this topic further in COWI.

Vetle Kallåk
Trondheim, June 9th, 2020

Master's Thesis Description

NTNU Trondheim
Norwegian University of Science and Technology
Department of Marine Technology – Group of Marine Structures

MASTER THESIS IN MARINE TECHNOLOGY

SPRING 2020

FOR

STUD.TECHN. Vetle Kallåk

Parametric design of semi-submersible floating wind turbines
Parametrisk design av halvt nedsenkbare flyttende vindturbiner

Background:

The wind industry has developed very fast in recent years, moving from onshore to offshore in shallow water and then to floating wind turbines (FWTs) in deep water. Semi-submersible floating wind turbines are a promising technology due to their wide applicability across different water depths and relatively simple installation. A wide variety of designs have been proposed, and there is increasing interest in optimization of the hull form to minimize cost, while still satisfying important strength and safety requirements.

In order to better understand the consequences of changes in the hull design on the overall responses of semi-submersible floating wind turbines, a parametric study of the hydrodynamic loads and wave-induced responses is proposed. For one (or more) parametrized hull shapes, several different floater designs for a 10 MW wind turbine will be proposed, and the effects of the hull shape on the first order response amplitude operator (RAO) will be assessed. In addition to global motions, first order wave loads within the hull should also be considered.

Assignment:

The following tasks should be addressed:

1. Literature review regarding semi-submersible floating wind turbine designs, response analysis, and design criteria. Review of theoretical considerations related to first and second order potential flow theory.
2. Identification of one (or more) hull form(s), and a baseline design for a 10 MW wind turbine. Definition of design parameters and design criteria.
3. Development of parametric inputs to i.e. Genie and HydroD for generating hull geometry and computing first order wave loads. Comparison of results for the baseline design against literature.
4. Parametric studies regarding influence of design parameters on the first order response amplitude operators (RAOs) for motions, and for internal hull loads. The effect of mean tilt angle on the RAOs should be considered.
5. If time permits, carry out global analysis of two selected designs in SIMA (including wind loads), and assess the importance of the wave loads compared to wind loads.
6. Report and conclude on the investigation.

The work scope could be larger than anticipated. Subject to approval from the supervisor, topics may be deleted from the list above or reduced in extent.

In the project, the candidate shall present his personal contribution to the resolution of problem within the scope of the project work.

Theories and conclusions should be based on mathematical derivations and/or logic reasoning identifying the various steps in the deduction.

The candidate should utilize the existing possibilities for obtaining relevant literature.

The project report should be organized in a rational manner to give a clear exposition of results, assessments, and conclusions. The text should be brief and to the point, with a clear language. Telegraphic language should be avoided.

The project report shall contain the following elements: A text defining the scope, preface, list of contents, main body of the project report, conclusions with recommendations for further work, list of symbols and acronyms, reference and (optional) appendices. All figures, tables and equations shall be numerated.

The supervisor may require that the candidate, in an early stage of the work, present a written plan for the completion of the work. The plan should include a budget for the use of computer and laboratory resources that will be charged to the department. Overruns shall be reported to the supervisor.

The original contribution of the candidate and material taken from other sources shall be clearly defined. Work from other sources shall be properly referenced using an acknowledged referencing system.

Erin Bachynski
Supervisor

Deadline: June 10th 2020

2

Contents

List of Figures

List of Tables

Nomenclature

Abbreviations

CFD	computational fluid dynamics
COB	center of buoyancy
COG	center of gravity
DCC	distance between center of columns
DOF	degree of freedom
EC	environmental condition
FWT	floating wind turbine
HP	heave plate
IEA	International Energy Agency
IRENA	International Renewable Energy Agency
KC	Keulegan-Carpenter
LHP	length of heave plate edge
MSL	mean sea level
MW	megawatt
RAO	response amplitude operator
RNA	rotor nacelle assembly
RWT	reference wind turbine
TLP	tension-leg platform
WT	wind turbine

Greek Letters

$\boldsymbol{\eta}, \dot{\boldsymbol{\eta}}, \ddot{\boldsymbol{\eta}}$	body displacement, velocity, acceleration matrix (6x1)
$\eta_k, \dot{\eta}_k, \ddot{\eta}_k$	body displacement, velocity, acceleration, $k = 1, ..., 6$ (surge, sway, heave, roll, pitch, and yaw, respectively)
λ	wavelength [m]
∇	volume displacement [m^3]
ω	wave frequency [rad/s]
ρ	density [kg/m^3]
σ	standard deviation
θ	phase angle [rad]
ζ	incident wave profile [m]

Latin Letters

$\boldsymbol{A}$	added mass matrix (6x6)
$\boldsymbol{B}$	linear damping matrix (6x6)
$\boldsymbol{C}$	hydrostatic restoring matrix (6x6)
$\boldsymbol{F}$	force matrix (6x1)

$\boldsymbol{M}$	mass matrix (6x6)
$\overline{GM}$	metacentric height [m]
A	area [m^2]
C_a	added mass coefficient [-]
C_D	drag coefficient [-]
D	diameter [m]
k	wave number [rad/m]
M	mass [kg]
r_{ii}	radius of gyration [m]
$S_w(\omega)$	wave spectrum [m^{2}s/rad]
$S_x(\omega)$	response spectrum [m^{2}s/rad]
t	time [sec]
z_{hub}	hub height above MSL [m]

Subscripts

a	amplitude
c	restoring
col	column
cs	cross-section
hp	heave plate
I	inertia
p	pressure
T	thrust

1 Introduction

1.1 Background

The world needs to move its energy supply from fossil to more sustainable energy sources. Onshore wind energy has proven to be a competitive solution to today's coal and gas industries. However, onshore wind requires large areas and has a large footprint on the land. In recent years, the wind industry has been moving offshore, building bottom-fixed wind turbines in shallow waters, where space limitations are less and the wind conditions are more favorable.

In 2018, offshore wind had a total installed capacity of 23 GW, providing 0.3 % of global electricity supply. However, the International Energy Agency, IEA, published a report in October 2019 stating that offshore wind has the potential to generate more than 420 000 TWh per year worldwide, more than 18 times the global electricity demand today (IEA, 2019). Of this, 80 % of the potential is from sites located in deep waters, above 60 meters, where floating wind turbines, FWTs, are said to be more economically feasible than bottom-fixed (Cruz and Atcheson, 2016). Further, IEA (2019) claims that under current policies the offshore wind market will expand by 13 % per year and become a \$1 trillion business by 2040.

In the search of higher exploitation of wind energy, the wind industry is moving further out in the oceans, and FWTs are being developed. With the huge potential of harvesting deep water offshore wind energy, there is an increasing interest in optimization of the hull form to minimize cost, while still satisfying important strength and safety requirements.

1.2 Scope and Objectives

Several promising concepts exist for FWT hulls. The semi-submersible design has proven to be a competitive concept, due to its low draft and simple, well-known mooring system. Therefore, the scope of this thesis is to investigate how changes in the hull design affect the overall wave-induced responses of a semi-submersible FWT design. For a parameterized hull shape designed for a 10 MW wind turbine, the effects of changes to the hull shape on the first-order response amplitude operators, RAOs, will be assessed. In addition to global motions, first-order wave loads within the hull will also be considered. This will give a better understanding of how different parameters influence the responses and how the hull could be optimized.

The objectives of this thesis are:

- Give an overview of existing semi-submersible floating wind turbine designs.

- Choose a favorable semi-submersible design and upscale it to support a 10 MW wind turbine.

- Calculate the wave-induced motion RAOs and internal hull loads on the parameterized platform.

- Discuss and compare the influence different design parameters have on the responses of the semi-submersible platform design.

- Suggest a cost-effective design while complying with strength and safety regulations.

- Assess the importance of including a wind-induced mean tilt angle in the analyses of the platform on the RAOs.

1.3   Structure of the Report

The thesis is structured as follows: First, the topic is introduced and the scope and objectives of the thesis are defined in Section 1. Secondly, Section 2 provides an overview of the offshore wind industry, different semi-submersible designs, and related research on the topic. In Section 3, the theory used for the calculations is presented and Section 4 explains the methods and software used for obtaining the results of the thesis. The results are presented and discussed in Section 5. First, the 10 MW upscaled design and general findings are presented in Section 5.1. The results from the parametric study are given in Section 5.2, and an improved design is suggested in Section 5.3. The effects of including a mean tilt angle are assessed and discussed in Section 5.4. The conclusion and recommendations to further work are given in Section 6. At the end of the report is the Appendix.

2 Literature Review

The literature review presents a further introduction to the offshore wind industry. Existing semi-submersible FWT platform designs are presented and compared in Section 2.2. Research related to this thesis is summarized in Section 2.3. In Section 2.4 and Section 2.5 are upscaling procedures of FWT hulls and the effects of heave plates discussed, respectively.

2.1 Offshore Wind Industry

The offshore wind industry has the advantage of the open sea, giving stronger and more reliable winds than those onshore. This results in higher capacity factors for offshore wind turbines compared to onshore wind turbines. The capacity factor is the average output over the year relative to the maximum rated power capacity. In 2018, the average global capacity factor for offshore wind turbines was 33 %, while for onshore wind turbines it was 25 % (IEA, 2019). In addition, new offshore wind projects are assumed to have capacity factors even above 50 %. The offshore wind marked grew by almost 30 % per year between 2010 and 2018 and the IEA predicts offshore wind to be competitive with fossil fuels within the next decade.

The first offshore wind farm was installed in Denmark in 1991, consisting of 11 turbines with a total capacity of 4.95 MW (Cruz and Atcheson, 2016). Since then, there has been a huge technological development, for instance with increasing turbine sizes. The average offshore wind turbine, WT, size grew from 1.6 MW in 2000 to 5.5 MW in 2018, and the industry is aiming for turbines with 15-20 MW capacity for 2030 (IRENA, 2019). Larger turbines leads to overall lower costs of the electricity produced and higher capacity factors, which are advantages for offshore WTs, and especially FWTs as they have the potential to be scaled larger than onshore and bottom-fixed WTs.

2.1.1 Floating Wind Turbines

Floating wind turbines, FWT, are more economically feasible than bottom-fixed for depths larger than 50-60 meters (Cruz and Atcheson, 2016). Therefore, it is normal to divide the available waters into shallow water, depths below 60 meters, and deep water, depths from 60 to 2 000 meters. This thesis focus on FWTs, as the potential for harvesting wind energy in deep water is nearly limitless.
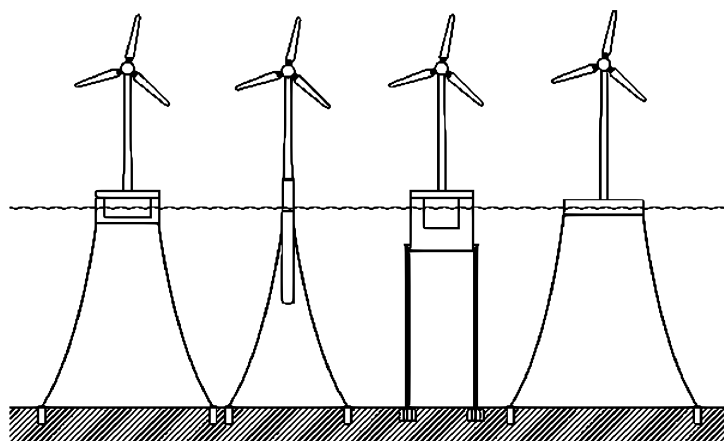
Figure 2.1: The most common floater types for wind turbines. From the left, semi-submersible, spar, tension-leg and barge platform (DNV GL AS, 2018).

A FWT structure consists of a rotor nacelle assembly (RNA), a tower, a hull, and a mooring system. The FWT structures could be divided into four concepts based on how they achieve

necessary stability, see Figure 2.1. The designs are taken from the offshore oil and gas industry (Cruz and Atcheson, 2016).

- Semi-submersible platform, buoyancy-stabilized by having a large water-plane area.

- Spar platform, ballast-stabilized by having a large draft.

- Tension-leg platform, TLP, mooring-stabilized by use of taut moorings.

- Barge platform, also buoyancy stabilized.

There also exist intermediate designs. The different concepts have their advantages and disadvantages. The spar platform requires large depths for installation, towing, and operation, but the fabrication is simpler than for the TLP or semi-submersible designs. The spar and TLP have more suited natural periods than the semi-submersible, but the semi-submersible has simpler mooring than the TLP. The semi-submersible design is stable at low draft and can be fully assembled onshore (Cruz and Atcheson, 2016). Due to these factors, it is not necessarily one design that is better than the others, site conditions and turbine size could be determining factors for selecting a design.

FWTs is a newly developing industry. In 2017, Equinor installed the first operational floating wind farm, the Hywind Scotland, consisting of 5 spar FWTs with a total installed capacity of 30 MW (Equinor, 2020). And in October 2019, Equinor (2019) announced their next FWT farm, the Hywind Tampen, consisting of 11 spar FWTs with a total capacity of 88 MW. Due to gained experience and scale effects, Equinor aims to halve capital expenditure per MW for Hywind Tampen.

Several other designs have been proposed in recent years and several demonstration projects are underway. For instance, the company Ideol has developed a barge floating structure for FWTs. In 2018, they installed the Floatgen in France with a 2 MW turbine and the Hibiki in Japan with a 3 MW turbine and are planning a 24 MW wind farm of 4 units outside France (Ideol, 2018). Principle Power is another company in the FWT industry with its semi-submersible concept WindFloat that is further explained in Section 2.2.3 and is used as the baseline design for this thesis. They deployed a 2 MW prototype in 2011 outside the coast of Portugal (Principle Power, 2019). In late 2019, they installed the world's largest FWT, with an 8.4 MW wind turbine. This was the first of three FWTs that will make up the WindFloat Atlantic wind farm outside Portugal with a total installed capacity of 25 MW (Principle Power, 2020). The WindFloat concept is also to be used for a 10 MW WT outside the south coast of France (Veselina Petrova, 2019).

Even though the FWT structures are inspired by the oil and gas industry, there are some important differences in the design criteria, which will help reduce costs when designing FWTs. These differences are (Cruz and Atcheson, 2016, pp. 7–8),

- FWTs are un-manned, giving lower risk to human life and several safety mechanisms are not required.

- The potential damages due to failure of a FWT is much lower than for an oil and gas production facility.

2.2   Existing Semi-Submersible Designs

The semi-submersible designs for FWTs are characterized by three to five primary columns, with the turbine either at the center or over one of the offset columns. They are fabricated from either steel or concrete and often designed with heave plates to reduce motions as explained in

Section 2.5. They have a relatively low draft and use standard catenary mooring lines. Due to the large water-plane area, wave loads will be relatively high, hence, bracing is often necessary to reduce the load effects (Cruz and Atcheson, 2016). The following sections give a summary of five distinct, promising semi-submersible designs that exist today. A comparison of the different designs is presented in Section 2.2.6.

(a) OO-Star (Dr.techn.Olav Olsen, 2020)   **(b)** NAUTILUS (Yu et al., 2018)   **(c)** WindFloat (Roddier, Peiffer, et al., 2011).
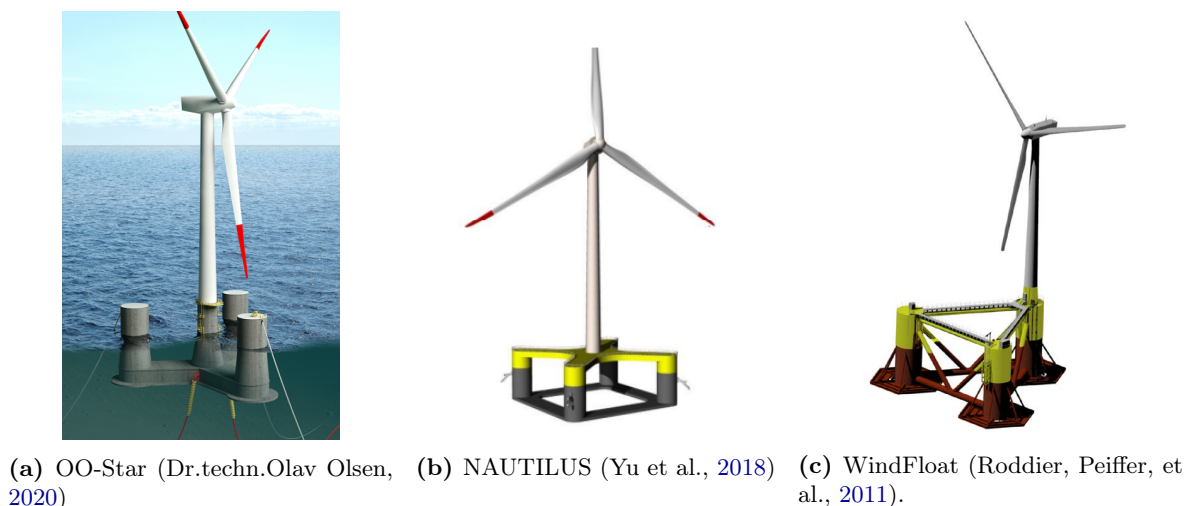
Figure 2.2: Three different existing semi-submersible FWT designs.

2.2.1   Olav Olsen OO-Star

The Olav Olsen OO-Star semi-submersible platform is developed by the company Dr.techn. Olav Olsen as part of the research project LIFES50+. LIFES50+ was part of the European Union funded program Horizon 2020 (LIFES50+, 2020). One of the objectives of the project was to optimize and qualify two innovative substructure designs for 10 MW turbines.

The design is shown in Figure 2.2a. It consists of a star-shaped base pontoon, which connects a central column with three outer columns, separated by a 120 degrees angle. The wind turbine, WT, is mounted on the center column, letting the buoyancy force of the center column absorb most of the WT weight. A disadvantage with the design is it could be difficult accessing the WT since one has to maneuver in between the outer columns. The outer columns have heave plates at the bottom. The platform is designed with post-tensioned concrete and a catenary mooring system with three mooring lines will be used. Concrete is chosen as the material to increase the lifetime of the structure since concrete has better fatigue properties. On the other side, using concrete yields a higher volume displacement and total substructure mass. The side columns have a diameter of 13.4 meters and the distance from the center column to the outer column is 37 meters. Yu et al. (2018) give a detailed description of platform geometry and structural and hydrodynamic properties.

2.2.2   NAUTILUS

The NAUTILUS semi-submersible substructure is the other design from the LIFES50+ project. The design is shown in Figure 2.2b. It is a four-columns structure in steel with the WT placed in the center, making the platform symmetrical. The WT is not supported by a central column, giving large stresses in the cross-shaped structure connecting the outer columns. A quadratic ring pontoon is mounted between the columns at the bottom, functioning as a heave plate. Notable about the design is that no bracing is used, simplifying construction. The WT is easily accessed from a ladder at one of the columns. Active seawater ballast is used to reduce mean trim from wind loads and a standard catenary mooring system with four mooring lines is utilized.

The columns have a diameter of 10.5 meters and the distance between them is 54.8 meters. Yu et al. (2018) and Galván et al. (2018) give detailed descriptions of the platform geometry and structural and hydrodynamic properties.

2.2.3 WindFloat

The WindFloat semi-submersible platform for FWTs is developed by Principle Power, Inc. The design is shown in Figure 2.2c. It is a three-columns steel structure with heave plates and the WT mounted on one of the columns (Principle Power, 2019). With the WT above one of the side columns, the structure is not symmetrical, but the weight of the WT is absorbed by the buoyancy force of the column. Further, installing the WT on top of the substructure becomes easier, since the lift is shorter. The WT is easily accessed from a ladder at one of the other columns. A summary of a feasibility study for the WindFloat concept is presented in the papers: Roddier, Cermelli, et al. (2009), Cermelli et al. (2009) and Aubault et al. (2009). The first paper describes the design basis, the second a hydrodynamic analysis, and the third a structural analysis. Further, Roddier, Peiffer, et al. (2011) present the dimensions and hydrodynamic performance of the WindFloat concept equipped with a generic 5 MW wind turbine. The columns have a diameter of 10 meters and the distance between them is 46.0 meters.

The design utilizes four standard, catenary mooring lines. The columns contain permanent water ballast, to achieve the operational draft. An active internal water ballast system is used to move water between the columns to counteract the mean drag loads on the WT. The system has a 20 minutes reaction time, to only account for significant changes in wind speed and direction.
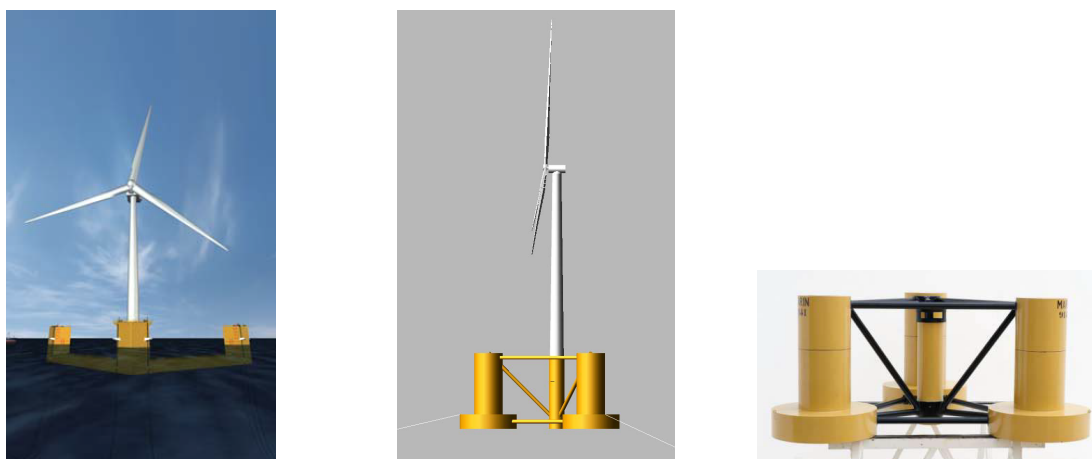
(a) Fukushima (Fukushima Off-shore Wind Consortium, 2020) **(b)** OC4-DeepCwind (Robertson et al., 2014) **(c)** OC4-DeepCwind (Robertson et al., 2014).

Figure 2.3: Two different existing semi-submersible FWT designs. In (c), a picture of a 1/50 scale model of the OC4-DeepCwind support structure is given.

2.2.4 Fukushima

The Fukushima offshore wind consortium in Japan has designed a V-shaped semi-submersible support structure for a 7 MW offshore wind turbine. The design is shown in Figure 2.3a. It is a simple design with three columns mounted in a V-shape, whereas the turbine is mounted on top of the center column. The development of the design is described by Ohta et al. (2013). As for the WindFloat, mounting the WT onto the platform requires a shorter lift than for the other designs. The platform consists of only flat surfaces, making manufacturing simple and mass production cheap. The design is also without bracing, lowering the risk of fatigue damages, and simplifies construction. Seawater ballast is used for regulating the draft and the trim of the platform due to mean drag forces on the WT. The platform is moored with 8 pieces of catenary

mooring. Karimirad and Michailides (2015) also report that using a braceless V-shaped semi-submersible platform for FWT is a feasible solution. Internal forces could become a problem as the two end columns are only mounted to the center column, giving possibly large bending moments on the pontoons.

2.2.5 OC4-DeepCwind

The OC4-DeepCwind semi-submersible is designed by the DeepCwind consortium for the Off-shore Code Comparison Collaboration Continuation, OC4, project. The design is shown in Figure 2.3b and Figure 2.3c. It is designed for a 5 MW wind turbine, which is mounted on a center column. There are three offset columns that are connected with the center column through cross members. There are in total 15 members, six connecting the offset columns in a triangle form, and nine connecting them to the center column. This makes the structure complex and increases production costs. A base column is designed at the bottom of each offset column, to reduce motions of the platform in waves by working as heave plates. The platform is moored with three catenary mooring lines and passive water ballast is used to obtain the desired draft. The structural and hydrodynamic properties of the platform are described by Robertson et al. (2014).

2.2.6 Comparison of Existing Designs

In Table 2.1 are the five FWT semi-submersible designs compared with respect to different parameters.

Table 2.1: Comparison of the five semi-submersible FWT designs. The substructure mass is without tower and mooring mass, but with ballast. Displacement is given for operation.

Parameter	OO-Star	NAUTILUS	WindFloat	Fukushima	OC4
WT Power [MW]	10	10	5	7	5
Number of columns [-]	4	4	3	3	4
Material [-]	Concrete	Steel	Steel	Steel	Steel
Hull material mass [kg]	-	2.70E+06	-	-	3.85E+06
Substructure mass [kg]	2.17E+07	6.58E+06	3.94E+06	-	1.35E+07
Displacement [m^3]	23 509	8 113	4 527	26 000	13 917
Draft [m]	22	15	17	17	20

2.3 Related Studies

Karimi et al. (2017) carried out a multi-objective design optimization for offshore FWT support structures to support a 5 MW WT. The optimization process builds on the work by Hall et al. (2013), but with a new optimization algorithm and an updated frequency domain dynamic model, which changed the Pareto optimal platform designs. First-order wave loads on three types of parameterized platform structures, tension-leg, spar buoy, and semi-submersible, were calculated using *WAMIT*. Viscous effects were accounted for by using a linear representation of Morison's equation. Changing the design parameters for the three types of structures, they calculated and compared the cost of construction and mooring system against the standard deviation of the nacelle fore-aft accelerations. The study showed that a four-column semi-submersible and tension-leg structures are more advantageous than a spar design. For the cheapest possible platform, the four-column semi-submersible platforms gave the best combination with low nacelle accelerations. The TLP-platforms could give lower nacelle accelerations, but then at a higher cost.

The semi-submersible design space consisted of a center column and three to five outer columns

with heave plates. The results showed a negative relationship between nacelle accelerations and overall cost, as for the other platforms. The four-column designs gave the most optimal combinations of low nacelle accelerations and low cost. For the semi-submersible optimal design points, reduced nacelle acceleration, at the price of higher cost, was achieved by the trend of increasing the draft, reducing the column diameters, and increasing the heave plate diameter. The draft and the heave plate diameter were increased by a higher factor than the reduction in column diameter. The radius from the center column to the outer columns was constantly around 28 meters for all the optimal design points. For all the four-column optimal design points an angled taut mooring system was suggested. While for the five and six columns designs, slack catenary mooring was used but moved towards taut mooring for more expensive designs. For the five and six columns designs, for achieving lower nacelle accelerations the heave plates were increased more in size, while the draft was adjusted less, implying that the heave plates were most important in obtaining lower nacelle accelerations. The outer column diameters were also increased, but much less than the heave plates.

Hall et al. (2014) performed an optimization process for FWT platforms by combining and linearly interpolating the hydrodynamic coefficients of six basis platforms, to explore new possible designs. The calculations were carried out in the frequency domain, with the objective of minimizing the nacelle accelerations. The results for a slack catenary mooring system and tension-leg mooring system gave similar results, with lowest nacelle accelerations by combining a large submerged volume with a widely distributed waterplane area.

Tracy (2007) presents a parametric study of the design space for a FWT structure. The parameterized structure consisted of a concrete ballasted cylinder, with three types of mooring configurations, slack catenary, tensions-leg, and taut catenary. Also here, linear hydrodynamics and *WAMIT* were used for calculating the hydrodynamic coefficients and the motions were calculated in the frequency domain. The standard deviations of the nacelle accelerations were compared against mooring line tensions and platform displacement. For all of the above-mentioned analyses, Pareto optimal designs are presented, where several parameters are adjusted for each design. Therefore, the influence each parameter has on the design is not studied, only the overall trends.

Wang (2014) presents the design process of a pontoon-type semi-submersible platform designed to support a 10 MW wind turbine. The design is based on the 5-MW-CSC hull presented by Luan, Gao, et al. (2016). The motions of the platform and internal loads were calculated using first-order potential theory and *Wadam*. Second-order wave loads were calculated, a mooring system proposed, and coupled wind-wave dynamic analysis performed. Also, a sensitivity analysis of how the different main dimensions affect the structure mass, displacement, maximum static pitch angle, and heave natural period was carried out based on hand calculations and used for the initial design. However, the effects on the hydrodynamic coefficients and excitation loads were not discussed, as in this thesis. The draft of the 10 MW design was decreased to 20 meters to make a less over-conservative design. The column diameters and distance between them were increased to account for the increased overturning moment from the WT.

The doctoral thesis by Bachynski (2014) deals with the design and dynamic analysis of FWT tension-leg platforms. Among other things, the effects of changing different design parameters on the behavior of FWT tension-leg platforms were investigated. The results from this investigation are also presented in Bachynski and Moan (2012). The designs were analyzed in waves and wind, using first- and higher-order theories. Even though only first-order waves are included in this thesis, the work by Bachynski (2014) is used as inspiration for how to present the results of the parametric study.

Antonutti et al. (2014) studied the effect of a wind-induced mean tilt angle on the hydrodynamics of the Dutch Tri-floater semi-submersible FWT design with heave plates. The influence of the submergence of the heave plates was also investigated. The analyses were conducted using first-order potential theory, and a boundary element solver. The study showed that the mean tilt angle could have important effects on the hydrodynamic coefficients and excitation forces, especially due to the vertical displacement of the heave plates and that this should be accounted for. The study was extended to analyses in the time domain in Antonutti et al. (2016), also showing that the mean tilt angle can affect the dynamics of the structure.

2.4   Upscaling Procedure

When upscaling a structure, geometric self-similarity is a usual procedure to use. A scaling factor, k, is then defined as the ratio of lengths,

$$k = \frac{l_{upscaled}}{l_{initial}}, \tag{2.1}$$

which is used to upscale all dimensions. Following this procedure, the scale factors for other relevant parameters are given in Table 2.2.

Table 2.2: Scale factors for different relevant parameters using geometric self-similarity scaling laws. C_P is the power coefficient of a wind turbine and v_{wind} is the velocity of the wind.

Parameter	Equation	Scale factor
Length	l	k
Volume	$V = l^3$	k^3
Mass	$M = \rho V$	k^3
Power	$P = \frac{\rho_{air}}{2} C_p \frac{\pi D_{rotor}^2}{4} v_{wind}^3$	k^2

When upscaling a wind turbine, a standard procedure is choosing a scaling factor based on the power rating of the upscaled wind turbine and the base wind turbine design, in other words, $k = \sqrt{P_{WT,upscaled}/P_{WT,initial}}$ (Bak et al., 2013). However, Leimeister (2016) presents an upscaling procedure for semi-submersible floaters when designed for a larger wind turbine. Instead of the scaling factor being based on the power ratio, Leimeister suggests it should be based on the mass ratio as,

$$k = \sqrt[3]{\frac{M_{WT,upscaled}}{M_{WT,initial}}}. \tag{2.2}$$

Following scaling theory, see Table 2.2, this should give the same scale factor as using the power ratio. However, due to technological developments in materials and efficiency, larger, new WT designs are improved with respect to the weight per power-output.

Leimeister (2016) based her work on the DeepCwind OC4 platform. The platform is an over-conservative suggested design, with a large mass and low maximum static pitch angle. It also has a low natural period in heave. Therefore, Leimeister first suggests an optimized design, where the upper side column diameters were scaled down, resulting in lower mass, higher maximum pitch angle, and higher heave natural period. The downscaling was based on obtaining a heave natural period of at least 20 seconds and a maximum static pitch angle of 5 degrees. The optimized design showed a reduction in the heave standard deviation.

For an optimized upscaling of a semi-submersible structure, Leimeister suggests using a different scaling factor on the diameters and wall thicknesses of the columns breaking the free surface. The center column diameter should scale with the diameter of the WT tower, so they still have the same diameter at the connection point. For the side columns, a scale factor that maintain the static pitch angle of the initial design is proposed, since it is assumed to be critically optimized for the initial design.

A design for the WindFloat concept supporting a 10 MW WT is presented by Son et al. (2018). The diameter of the columns is kept at 10 meters, the distance between the columns is increased to 70 meters, and the lightship weight is 2000 tons. More information is not given, as this is the property of Principle Power. The work presents RAOs and nacelle accelerations without axes for comparing results from different software.

2.5 Effects of Heave Plates

Heave plates are popular appendages used on semi-submersible and spar platforms. Heave plates provide the structure with increased added mass and damping in heave, roll, and pitch. The increase in added mass comes from the large amount of water that is displaced as the platform moves. Therefore, heave plates are often called water entrapment plates. The increase in added mass gives a higher natural period in heave, roll, and pitch, moving the natural periods out of the wave energy spectrum. Also, the sharp edges of the heave plates increase vortex shedding which gives a larger damping force and reduces the platform motions (Roddier, Peiffer, et al., 2011).

Due to the highly non-linear problem of heave plates, since viscous forces are important, experiments and CFD calculations are necessary for estimating the added mass and damping. Several studies have been conducted about the subject, as heave plates have been commonly used in the oil and gas industry, and are popular in the design of FWT support structures. When comparing results from calculations on heave plates, two non-dimensional parameters are often used, the Keulegan-Carpenter (KC) number and β,

$$KC = \frac{2\pi\eta_3}{D_{hp}} \quad \& \quad \beta = \frac{D_{hp}^2 f}{\nu}, \tag{2.3}$$

where η_3 is the heave amplitude of oscillation, D_{hp} is the diameter of the heave plate, f is the frequency of oscillation and ν is the kinematic viscosity of the fluid. The Reynolds number could be obtained by $Re = KC\,\beta$.

The hydrodynamic properties of a heave plate depend on, among others, the plate thickness-diameter ratio, the ratio between the diameters of the heave plate and the column it is attached to, the porosity, and the oscillation amplitude and frequency. Numerical studies on a single column with a circular heave plate attached to the keel are presented by, for instance, Tao and K. Thiagarajan (2003), Tao and Cai (2004), and Tao, Molin, et al. (2007). The thickness-diameter ratio of the plate affects the generation of vortices, in the sense that for a very thin heave plate, the two edges of the plate act as one sharp edge, giving another flow field than for a thicker plate. The studies showed a trend of increasing added mass and damping for lower thickness-diameter ratios due to viscous effects and mainly for low ratios. The impact was largest on the viscous damping. The column attached to the heave plate will reduce the effect of the heave plate on the column side since less water will be entrapped, reducing mainly the added mass. The theoretical added mass of a circular disk oscillating vertically in infinite water is (DNV GL AS, 2019a),

$$A_{33} = \frac{1}{3}\rho D_{hp}^3. \tag{2.4}$$

Tao, Molin, et al. (2007) suggest the theoretical added mass of a cylinder with a circular disk attached at its base could be estimated as,

$$A_{33} = \frac{1}{12}\rho(2D_{hp}^3 + 3\pi D_{hp}^2 z - \pi^3 z^3 - 3\pi D_{col}^2 z), \tag{2.5}$$

where $z = \frac{1}{\pi}\sqrt{D_{hp}^2 - D_{col}^2}$, and D_{col} is the diameter of the column. Tao and Cai (2004) found that the damping also increases with increasing D_{hp}/D_{col}, but tends to flatten for higher ratios and that this value depends on the KC number. For KC equal 1, 0.5, and 0.1, the flattening occurs at $D_{hp}/D_{col} \approx 1.65$, $D_{hp}/D_{col} \approx 1.45$, and $D_{hp}/D_{col} \approx 1.3$, respectively. At low ratios, the boundary layer from the columns reduce the vortex shedding at the edges, lowering the damping.

Tao and Dray (2008) found through model tests that heave plates with high porosity increase the damping at very low KC numbers, while it, in general, gives lower added mass for all KC numbers. When the oscillation amplitude goes to zero, the added mass from the heave plates will also become zero, implying that added mass found from experiments is very dependent on the KC number. The added mass and damping coefficients were found to increase linearly with increasing KC numbers for the tested area of $0.2 < KC < 1.2$. The quadratic drag coefficients for the heave plates when oscillated at 1 Hz are plotted for different KC numbers in Figure 2.4a. The drag coefficient decreases non-linearly with increasing KC number.

All the above-mentioned experiments were conducted in deep water conditions, with the heave plate being deeply submerged. Wadhwa and K. P. Thiagarajan (2009) studied the effects of a disk oscillating close to the free surface experimentally, with submergence-diameter ratios from 0.1 to 1. Both added mass and damping coefficients increased with lower submergence, and a good agreement with the results from Tao and Dray (2008) was shown for the submergence-diameter ratio of 1, meaning this could be assumed as the heave plate being deeply submerged.

Lopez-Pavon and Souto-Iglesias (2015) studied the effects of heave plates on a three-column semi-submersible FWT. Model tests of one of the columns with a plain and a reinforced heave plate were completed. The results were compared to numerical simulations. Both a frequency domain first-order panel method in *Wadam* and a Reynolds-Averaged Navier-Stokes CFD method in *ANSYS CFX* were used. The results for the added mass and damping coefficients showed a weak link with the oscillation frequency and a large dependence with the KC number. The low dependency of frequency is explained with the high submergence-diameter ratio of the heave plate, being 0.775. Further, for a plain disk the *Wadam* calculated added mass was close to the theoretical value for a column-plate structure, equation (2.5), also with a low dependency of frequency. The added mass from experiments and CFD showed good agreement and were higher than the theoretical value and increased with higher KC numbers. A higher KC number gave a higher heave damping coefficient also, as found by Tao, Molin, et al. (2007) and Tao and Dray (2008). The potential radiation damping from *Wadam* was found to be negligible, again because of the relatively large distance to the surface. The reinforced plate gave higher added mass than the plain for low KC numbers and in *Wadam*, while the damping of the reinforced plate was lower for all KC numbers since the vortex shedding was reduced. The differences in added mass were much lower than for the damping. The drag coefficients found from the experiments are plotted for different frequencies and KC numbers in Figure 2.4b.

The mentioned studies have been conducted with circular heave plates. Moreno et al. (2016) present experimental results for the heave added mass and damping of a column-heave plate structure with a circular and a hexagonal heave plate made for FWT platforms. The hexagonal

heave plate was based on the WindFloat concept. The comparison showed that a circular and hexagonal heave plate of the same equivalent diameter have similar hydrodynamic properties over the range of $0.05 < KC < 1.2$ and $1\,\mathrm{Hz} < f < 6\,\mathrm{Hz}$ tested. The largest difference found was 8 % in damping. Further, the results showed that the added mass and damping coefficients are very dependent on β for $KC < 0.3$, where increasing frequency gave higher added mass and damping. The submergence-diameter ratio of the heave plates was 0.9. This trend could also be seen in Figure 2.4b for $KC = 0.309$, based on the experiments by Lopez-Pavon and Souto-Iglesias (2015).

Figure 2.4 shows the quadratic drag coefficients found with model experiments by Tao and Dray (2008) and Lopez-Pavon and Souto-Iglesias (2015) for circular heave plates. As seen from the figure, the drag coefficients from the two different experiments are similar for the same KC numbers. Even though the experiments were completed with models of different D_{hp}/D_{col} ratio, thickness-diameter ratio, submergence-diameter ratio, and frequency, implying that the KC number is the most important parameter in the tested range.

(a) Tao and Dray (2008)   **(b)** Lopez-Pavon and Souto-Iglesias (2015)
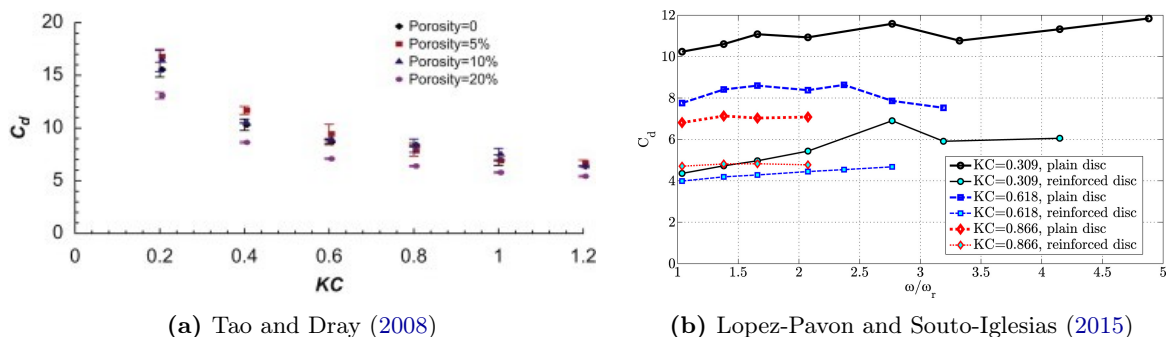
Figure 2.4: Drag coefficients for circular heave plates from experiments. The results from Tao and Dray (2008) are given for a oscillation frequency of 1 Hz and for heave plates of different porosity. The results from Lopez-Pavon and Souto-Iglesias (2015) are given for a frequency made non-dimensional with the theoretical heave natural frequency. The drag coefficients are given for different KC numbers, and a plain and reinforced disk.

To summarize, the potential added mass is highly influenced by the D_{hp}/D_{col} ratio. As found by Lopez-Pavon and Souto-Iglesias (2015), modeling heave plates in potential theory will give errors, as viscous effects change the pressure field around the heave plates. The potential added mass calculated for the heave plates was lower than found from experiments. Using experimental data and potential calculations one could calculate a correction of added mass for the heave plates. One could also find parametric data for heave plates, and use this for correcting the added mass. However, this demands to find data for a heave plate with the same geometrical parameters and in the same conditions, as discussed above. Since a parametric study is conducted in this thesis, the potential added mass from *Wadam* will be used without correction to simplify the procedure.

Potential damping could be neglected, at least if the submergence-diameter ratio is above 1. For these cases, viscous drag loads from the vortex shedding at the edges are most important. The drag coefficient is mainly dependent on the thickness-diameter ratio of the heave plate and the KC number. For low KC numbers, the D_{hp}/D_{col} ratio and the oscillation frequency could also be important. As seen from the comparison in Figure 2.4, the KC number seems to be the most important factor in the tested range.

3   Theory

This section will describe the theory used for the calculations. First, the rigid body equations of motions and how they are solved in the frequency domain are described. Secondly, the hydrodynamic theory used is presented. The coordinate system follows the right-hand rule, with $z = 0$ at the mean sea level and the z-axis pointing upwards.

3.1   Structural Dynamics

3.1.1   Rigid Body Equations of Motions

In this thesis, it is assumed that the platform with the wind turbine behaves as a rigid body. Further, by assuming steady-state harmonic responses, the coupled equations of rigid body motions for the floating platform in six degrees of freedom are given as (Faltinsen, 1990, p. 66),

$$\sum_{k=1}^{6} [(M_{jk} + A_{jk}(\omega))\ddot{\eta}_k + B_{jk}(\omega)\dot{\eta}_k + C_{jk}\eta_k] = F_j(\omega)e^{iwt}; \text{ for } j = 1, ..., 6. \qquad (3.1)$$

Where η_k are the motions, the k subscript denotes the mode of the six degrees of freedom, being surge, sway, heave, roll, pitch and yaw in the increasing order of k, respectively, and the dot(s) represent time derivative(s). The j subscript denotes the force direction. The equations for $j = 1, 2, 3$ results from Newton's second law, while the equations for $j = 4, 5, 6$ follows from the equation of angular momentum. M_{jk} are the components of the mass and inertia matrix for the structure, A_{jk} are the added mass and inertia coefficients, B_{jk} are the damping coefficients, C_{jk} are the hydrostatic restoring coefficients, F_j are the complex amplitudes of the excitation forces and moments on the structure and ω is the frequency of the harmonic excitation. The mass matrix is defined in this section, while the other terms are further explained in Section 3.2.3 and Section 3.2.4.

The uncoupled and undamped natural frequency, ω_{nk} of the k degree of freedom for the platform is given by,

$$\omega_{nk} = \sqrt{\frac{C_{kk}}{M_{kk} + A_{kk}}}. \qquad (3.2)$$

Assuming coupling effects do not significantly modify the natural frequency, excitation forces at this frequency will result in large motions unless the damping is high or the excitation force is low due to for instance cancellation effects.

The mass matrix for a floating structure with the center of gravity located at (x_G, y_G, z_G) is given as,

$$\boldsymbol{M} = \begin{bmatrix} M & 0 & 0 & 0 & Mz_G & -My_G \\ 0 & M & 0 & -Mz_G & 0 & Mx_G \\ 0 & 0 & M & My_G & -Mx_G & 0 \\ 0 & -Mz_G & My_G & I_{44} & I_{45} & I_{46} \\ Mz_G & 0 & -Mx_G & I_{54} & I_{55} & I_{56} \\ -My_G & Mx_G & 0 & I_{64} & I_{65} & I_{66} \end{bmatrix}. \qquad (3.3)$$

Where M is the total mass of the structure, and I_{kk} are the moments of inertia and I_{jk} are the products of inertia with respect to the coordinate system (x, y, z). The moment of inertia terms are defined as,

$$I_{kk} = Mr_{kk}^2, \tag{3.4}$$

where r_{kk} is the radius of gyration for the mode k. The radii of gyration are found by calculating local inertia and using the parallel axis theorem,

$$r_{kk} = \sqrt{\frac{1}{M}\left(\Sigma_{n=1}^N I_{kk,local,n} + d_n^2 \Delta m_n\right)}. \tag{3.5}$$

Here, $I_{kk,local,n}$ is the moment of inertia of the component n in the kth mode about its centroidal axis, d_n is the distance between the local and global axes, and Δm_n is the mass of the component. The products of inertia are defined as,

$$I_{jk} = Mr_{jk}|r_{jk}|, \tag{3.6}$$

where

$$r_{jk} = -\sqrt{\frac{\Sigma_{n=1}^N x_{j,n} x_{k,n} \Delta m_n}{M}} \operatorname{sign}\left(\Sigma_{n=1}^N x_{j,n} x_{k,n} \Delta m_n\right). \tag{3.7}$$

3.1.2   Frequency Domain Method

When analyzing FWTs, it is normal to carry out a time domain analysis, to account for non-linear effects from waves and wind, however, these calculations are time-consuming (Cruz and Atcheson, 2016). For a parametric study, focusing only on wave-induced responses and since several designs are to be studied, a faster, more convenient method is neglecting or linearizing nonlinear effects and calculate the motions of the structure in the frequency domain (Faltinsen, 1990). By neglecting or linearizing nonlinear terms, the excitation forces and the motions of the structure will harmonically oscillate with the frequency of the incoming waves, the motions could then be written as a six times one matrix,

$$\boldsymbol{\eta}(\omega) = \begin{bmatrix} ... \\ \eta_{ka} e^{i(\omega t + \theta_k)} \\ ... \end{bmatrix}; \quad \text{for} \ \ k = 1, ..., 6. \tag{3.8}$$

Where η_{ka} is the motion amplitude in mode k of the six degrees of freedom, and θ_k is the phase angle of the motion, defined in this thesis as the phase lead of the motion relative to an incident wave with the wave crest at the origin of the global coordinate system, in accordance with how it is defined in *Wadam* (DNV GL AS, 2019d). The excitation force could be written similarly, as a six times one matrix,

$$\boldsymbol{F}(\omega) = \begin{bmatrix} ... \\ F_{ja} e^{i(\omega t + \theta_{F_j})} \\ ... \end{bmatrix}; \quad \text{for} \ \ j = 1, ..., 6. \tag{3.9}$$

The excitation forces are calculated by *Wadam* and given as complex numbers. The absolute value represents the force/moment amplitude and the phase angle give the phase lead of the force/moment relative to the incident wave, as for the motions.

The system of second order coupled differential equations could then be solved by inserting equation (3.8) and (3.9) into equation (3.1). Then, the $e^{i\omega t}$ term on both sides of the equation are canceled out and equation (3.1) could be written in matrix form in the frequency domain as,

$$[-\omega^2(\boldsymbol{M} + \boldsymbol{A}(\omega)) + i\omega \boldsymbol{B}(\omega) + \boldsymbol{C}]\boldsymbol{\eta}(\omega) = \boldsymbol{F}(\omega). \tag{3.10}$$

Where $\boldsymbol{M}$, $\boldsymbol{A}$, $\boldsymbol{B}$, $\boldsymbol{C}$ are the six times six mass, added mass, damping and restoring matrices, respectively. Since the excitation loads are linearly dependent on the wave amplitude in linear theory, the equation is solved concerning the motions as,

$$\boldsymbol{\eta}(\omega) = \underbrace{[-\omega^2(\boldsymbol{M} + \boldsymbol{A}(\omega)) + i\omega \boldsymbol{B}(\omega) + \boldsymbol{C}]^{-1}\boldsymbol{F}(\omega)}_{\boldsymbol{H}(\omega)}\zeta_a. \tag{3.11}$$

Where ζ_a is the wave amplitude and $\boldsymbol{H}(\omega)$ are the six times one response amplitude operators, RAOs, of the structure motions, representing the linear relation between the wave amplitude and the motion amplitudes, and also the phase difference.

The horizontal nacelle acceleration RAO is calculated as (Karimi et al., 2017),

$$RAO_{a,nacelle}(\omega) = -\omega^2(\eta_1(\omega) + z_{hub}\eta_5(\omega)), \tag{3.12}$$

where z_{hub} is the hub height above the mean sea level.

3.2 Hydrodynamics

3.2.1 Linear Wave Theory

First-order potential theory is used for calculating the loads on the structure, both by *Wadam* and in the *MATLAB* code. Linear wave theory is used in first-order potential theory. The incident wave profile, ζ, is defined to have a wave crest at the origin for $t = 0$ as (DNV GL AS, 2019d),

$$\zeta = \Re[\zeta_a e^{i(\omega t - k(x\cos\beta + y\sin\beta))}], \tag{3.13}$$

where ζ_a is the wave amplitude, $\omega = \frac{2\pi}{T}$ is the angular frequency of the incident wave, $k = \frac{2\pi}{\lambda}$ is the wave number and β is the angle between the positive x-axis and the propagating direction of the incoming waves. T and λ are the wave period and wavelength, respectively. The linear wave dispersion relation is given as,

$$\omega^2 = kg\tanh(kd), \tag{3.14}$$

where d is the water depth. A complex velocity potential, ϕ, could be defined separated from the time-dependent velocity potential, Φ, for the fluid velocity potential since the waves are harmonic,

$$\Phi = \Re[\phi e^{i\omega t}], \tag{3.15}$$

where the complex velocity potential for the linear incident waves is given as,

$$\phi_0 = i\frac{g\zeta_a}{\omega}\frac{\cosh\left(k(z+d)\right)}{\cosh\left(kd\right)}e^{-ik(x\cos\beta+y\sin\beta)}. \tag{3.16}$$

The complex velocity potential for a potential flow is in general found by solving the Laplace equation with relevant boundary conditions on the fluid. For linear waves, these boundary conditions are the linearized free-surface condition and the sea bottom condition, explained by for instance Faltinsen (1990).

3.2.2   Statistical Description of Waves and Responses

A practical parameter for comparing dynamic varying responses is through the standard deviation. For first-order harmonic responses, the expected value is zero. The standard deviation describes the variation of the response from the expected value. A high standard deviation implies a higher probability for larger response amplitudes. The standard deviation of the response depends on the RAOs and a wave spectrum.

With linear theory, a long-crested irregular sea could be described as the sum of regular sinusoidal waves with different amplitudes and frequencies. The distribution of the different wave amplitudes and frequencies could be expressed by a wave spectrum, $S_w(\omega)$, defined as,

$$\frac{1}{2}\zeta_{a,j}^2 = S_w(\omega_j)\Delta\omega, \tag{3.17}$$

where $\Delta\omega$ is a constant frequency interval (Faltinsen, 1990). Since the wave spectrum is related to the wave amplitude squared, it is connected to the energy of the sea state per unit area. The area under the wave spectrum gives the total energy of the linear sea state per unit area when multiplied with gravitational acceleration and the seawater density. Further, the sea surface is assumed Gaussian distributed with expected value zero. The variance could be shown to be,

$$\sigma_w^2 = \int_0^\infty S_w(\omega)d\omega, \tag{3.18}$$

when the number of regular waves goes to infinity and $\Delta\omega \to 0$.

By defining a response spectrum, S_x, in the same way as the wave spectrum and knowing that $x = |RAO|\zeta_a$, the following relation is obtained,

$$S_x(\omega) = |RAO(\omega)|^2 S_w(\omega). \tag{3.19}$$

The standard deviation of the response is then calculated as,

$$\sigma_x = \sqrt{\int_0^\infty S_x(\omega)d\omega}. \tag{3.20}$$

3.2.3   Hydrostatic Restoring Forces and Moments

The hydrostatic forces on the body are the forces and moments from the pressure field of the water at rest. The hydrostatic restoring coefficients, defined in equation (3.1), results from the changes in the buoyancy force due to the hydrostatic pressure as the body move. The only

non-zero hydrostatic restoring coefficients for a structure with a xz-symmetry plane for the submerged volume are calculated as (Faltinsen, 1990),

$$C_{33} = \rho g A_{WP}, \tag{3.21}$$

$$C_{35} = C_{53} = -\rho g \iint_{A_{WP}} x \, ds, \tag{3.22}$$

$$C_{44} = \rho g \nabla (z_B - z_G) + \rho g \iint_{A_{WP}} y^2 \, ds = \rho g \nabla \overline{GM}_T, \tag{3.23}$$

$$C_{55} = \rho g \nabla (z_B - z_G) + \rho g \iint_{A_{WP}} x^2 \, ds = \rho g \nabla \overline{GM}_L. \tag{3.24}$$

Where A_{WP} is the waterplane area, ∇ is the displaced volume of the structure, z_B and z_G are the z-coordinates of the center of buoyancy and center of gravity, respectively. $\overline{GM}_T$ and $\overline{GM}_L$ are the transverse and longitudinal metacentric heights, respectively.

3.2.4 First-Order Effects

First-order effects are calculated by only accounting for forces linear proportional to the wave amplitude. This is called linear theory and results in the wave-induced motions and load amplitudes to be linearly proportional to the wave amplitude. For this to be a good assumption, the wave steepness must be small and the wave amplitudes small compared to the body dimensions (Faltinsen, 1990).

When linearity is assumed, the superposition principle can be used to split the hydrodynamic problem of a floating structure in waves into two parts, the diffraction problem and the radiation problem. The diffraction problem calculates the forces and moments from the incident waves on the body restrained from oscillating. In the radiation problem, the forces and moments on the body when forced to oscillate in all degrees of freedom with the wave frequency are calculated with no incident waves. The pressure forces from the seawater are only calculated to the mean sea level since the problem is linearized (Faltinsen, 1990).

From the radiation problem, the added mass (A_{jk}), damping (B_{jk}) and restoring (C_{jk}) terms are obtained. The added mass and damping terms are pressure forces and moments acting on the structure from the seawater opposing the forced, harmonic motions of the structure. The added mass and damping forces and moments are proportional to the acceleration and velocity of the forced motion, respectively, as seen in equation (3.1). Due to this, the values of the added mass and damping coefficients depends on the wave frequency. The restoring terms are calculated from hydrostatic considerations, as described in Section 3.2.3, and do not depend on the wave frequency. The damping obtained from linear theory is only related to the generation of surface waves, as the fluid is assumed inviscid.

From the diffraction problem, the wave excitation forces and moments (F_j) are calculated. The excitation loads could be divided into two parts, Froude-Kriloff and diffraction loads. Froude-Kriloff loads correspond to loads on the structure from the undisturbed pressure field of the incident waves as if the structure was not present. The diffraction forces are due to the structure changes the wave pressure field. This force is found in the same manner as the added mass and damping coefficients since one has to solve a boundary value problem for the velocity potential. Hence, it is related to added mass and damping (Faltinsen, 1990).

3.2.5 Second-Order Effects

Non-linear effects become important in severe sea states and for calculating drift motions of structures, which are important for the dimensioning of the mooring system. The most used method for calculating non-linear effects is by still assuming potential theory and use second-order theory. In second-order theory, all terms in the velocity potential, fluid pressure, and wave loads that are linear with or proportional to the square of the wave amplitude are kept. Solving the second-order problem results in mean forces, difference, and sum-frequency forces, in addition to the linear solution (Faltinsen, 1990). Second-order effects are not included in this thesis due to time limitations and since the mooring system is not part of the analyses. Further, Faltinsen (1990) writes: "Linear theory can, to a large extent, describe the wave-induced motions and loads on semi-submersibles".

3.2.6 Viscous Forces

Viscous forces are important for high sea states, with large wave heights and long waves. They are also important for determining the hydrodynamic damping of the platform motions, especially in heave, roll, and pitch, where potential damping is low. Therefore, quadratic viscous drag forces are accounted for by using a linearized Morison's equation.

3.2.7 Morison's Equation

For calculating wave forces on slender cylindrical structures, Morison's equation is often used as an alternative to potential flow theories, since it also account for viscous forces. A cylinder is assumed slender when the wave length is more than five times larger than the diameter of the cylinder, $\lambda > 5D$ (Faltinsen, 1990). The horizontal force from an incident wave on a strip with length dz of a vertical floating cylinder is given by Morison's equation as (Pettersen, 2007),

$$dF_x = \underbrace{\rho \frac{\pi D^2}{4}(1 + C_a)a_1 dz - \rho \frac{\pi D^2}{4}C_a \dot{v}_1 dz}_{Inertia\ forces} + \underbrace{\frac{1}{2}\rho C_D D|u - v_1|(u - v_1)dz}_{Drag\ force}. \qquad (3.25)$$

Where ρ is the seawater density, D is the cylinder diameter, a_1 and u are the horizontal acceleration and velocity of the undisturbed fluid at the mid-point of the strip, and v_1 is the horizontal body velocity at the mid-point of the strip. C_a and C_D are the added mass and drag coefficients, respectively. $C_a = C_M - 1$, where C_M is the mass coefficient. Morison's equation is semi-empirical, in the sense that the first term of the inertia forces could be derived from linear potential theory, and equals the Froude-Kriloff force plus the diffraction force on a strip of the cylinder when $C_a = 1$, while the two coefficients are empirical and adjusted to fit the relevant problem. The added mass and drag coefficients are discussed in Section 3.2.8. The second term of the inertia forces is the correction for added mass due to the movement of the cylinder in the water. Morison's equation account for viscous forces on the structure with a quadratic drag force term.

To integrate the forces from Morison's equation in the equations of motion, equation (3.1), the terms proportional to the body and incident wave fluid motions are separated since the body motions are not known. The procedure of using Morison's equation in the frequency domain on inclined cylinders is described, among others, by Borgman (1958) and Housseine et al. (2015), and is summarized in the following text.

$$F_{Morison} = F_{wave} + F_{motion}. \qquad (3.26)$$

The forces from equation (3.25) are calculated on each relevant, slender element, denoted by the

subscript k. Each element is discretized into N slices with a fixed length h_k. The slices are indicated by the subscript $j = 1, ..., N$. The forces are then calculated at the center, (x_{Gj}, y_{Gj}, z_{Gj}), of each of these slices and then summed up for obtaining the total force on the element. As the forces are calculated at the center of each slice, summing together the forces at each slice equals using the trapezoidal rule on the element.

Morison's equation calculate the forces on the cylinder from the flow perpendicular on the cylinder axis, hence the forces in x-, y- and z-directions are calculated by finding the flow perpendicular on the cylinder axis,

$$\boldsymbol{U}_{n,j} = \overrightarrow{\boldsymbol{n}_k} \times \boldsymbol{U}_j \times \overrightarrow{\boldsymbol{n}_k} = \boldsymbol{P}_k \boldsymbol{U}_j, \tag{3.27}$$

where $\overrightarrow{\boldsymbol{n}_k} = \begin{bmatrix} x_{\overrightarrow{n_k}} & y_{\overrightarrow{n_k}} & z_{\overrightarrow{n_k}} \end{bmatrix}^T$ is the unit vector along the cylinder axis and $\boldsymbol{U}_j = \begin{bmatrix} u & v & w \end{bmatrix}^T$ is the velocity vector of the undisturbed fluid flow at the center of the strip calculated from the velocity potential for the incident waves. $\boldsymbol{P}_k$ is the projection matrix defined as,

$$\boldsymbol{P}_k = \begin{bmatrix} y_{\overrightarrow{n_k}}^2 + z_{\overrightarrow{n_k}}^2 & -x_{\overrightarrow{n_k}} y_{\overrightarrow{n_k}} & -x_{\overrightarrow{n_k}} z_{\overrightarrow{n_k}} \\ -x_{\overrightarrow{n_k}} y_{\overrightarrow{n_k}} & x_{\overrightarrow{n_k}}^2 + z_{\overrightarrow{n_k}}^2 & -y_{\overrightarrow{n_k}} z_{\overrightarrow{n_k}} \\ -x_{\overrightarrow{n_k}} z_{\overrightarrow{n_k}} & -y_{\overrightarrow{n_k}} z_{\overrightarrow{n_k}} & x_{\overrightarrow{n_k}}^2 + y_{\overrightarrow{n_k}}^2 \end{bmatrix}. \tag{3.28}$$

The forces on the strip from the incoming waves could then be written in the frequency domain as,

$$\begin{bmatrix} dF_{1,wave,j} \\ dF_{2,wave,j} \\ dF_{3,wave,j} \end{bmatrix} = i\omega\rho \frac{\pi D_k^2}{4} h_k (1 + C_{a,k})(\boldsymbol{P}_k \boldsymbol{U}_j) + \frac{1}{2} \rho C_{D,k} D_k h_k |\boldsymbol{P}_k(\boldsymbol{U}_j - \boldsymbol{v}_j)|(\boldsymbol{P}_k \boldsymbol{U}_j). \tag{3.29}$$

Here, it has been used that $\boldsymbol{a}_j = i\omega \boldsymbol{U}_j$. For calculating the moments and the motions of the slice j, the matrix $\boldsymbol{S}_j$ is defined to give the location of the slice relative to a reference point (x_G, y_G, z_G) in a global coordinate system,

$$\boldsymbol{S}_j = \begin{bmatrix} 0 & z_{Gj} - z_G & -(y_{Gj} - y_G) \\ -(z_{Gj} - z_G) & 0 & x_{Gj} - x_G \\ y_{Gj} - y_G & -(x_{Gj} - x_G) & 0 \end{bmatrix}. \tag{3.30}$$

The global moments from the forces on each slice are then calculated as,

$$\begin{bmatrix} dF_{4,wave,j} \\ dF_{5,wave,j} \\ dF_{6,wave,j} \end{bmatrix} = -\boldsymbol{S}_j \begin{bmatrix} dF_{1,wave,j} \\ dF_{2,wave,j} \\ dF_{3,wave,j} \end{bmatrix}, \tag{3.31}$$

and the rigid body translation velocities of each slice are found by,

$$\boldsymbol{v}_j = \begin{bmatrix} v_{1,j} \\ v_{2,j} \\ v_{3,j} \end{bmatrix} = i\omega \begin{bmatrix} \boldsymbol{I}_3 & \boldsymbol{S}_j \end{bmatrix} \boldsymbol{\eta}, \tag{3.32}$$

where $\boldsymbol{I}_3$ is the three times three identity matrix and $\boldsymbol{\eta}$ is the six times one rigid body motions matrix.

Further, in order to solve to equations of motions in the frequency domain, the quadratic drag term has to be linearized. This is done by introducing a linear damping term that absorbs the same amount of energy over one period as the nonlinear term. This is called an equivalent linearization, and is given by,

$$|\boldsymbol{P}_k(\boldsymbol{U}_j - \boldsymbol{v}_j)| \approx \boldsymbol{K}_j = \frac{8}{3\pi}\boldsymbol{V}_{max} = \frac{8}{3\pi}|\boldsymbol{P}_k(\boldsymbol{U}_j - i\omega\begin{bmatrix}\boldsymbol{I}_3 & \boldsymbol{S}_j\end{bmatrix}\boldsymbol{\eta})|, \tag{3.33}$$

where $\boldsymbol{K}_j$ is a three times one matrix and $\boldsymbol{V}_{max}$ is the velocity amplitude at the slice. As seen from the equation, the linearized term depends on the amplitude of the structure motions. Therefore, an iteration process is required. The first time, the motions are guessed, and the forces from Morison's equation calculated, then the equations of motion are solved with the new forces calculated. This processes is repeated until convergence. The forces related to the motions of the structure could be written as,

$$\begin{aligned} d\boldsymbol{F}_{motion,j} = \omega^2 \underbrace{\rho\frac{\pi D_k^2}{4}h_k C_{a,k}\begin{bmatrix}\boldsymbol{P}_k & \boldsymbol{P}_k\boldsymbol{S}_j \\ -\boldsymbol{S}_j\boldsymbol{P}_k & -\boldsymbol{S}_j\boldsymbol{P}_k\boldsymbol{S}_j\end{bmatrix}\boldsymbol{\eta}}_{d\boldsymbol{A}_{mor,j}} \\ - i\omega\underbrace{\frac{1}{2}\rho C_{D,k}D_k h_k\begin{bmatrix}\boldsymbol{K}_j\boldsymbol{P}_k & \boldsymbol{K}_j\boldsymbol{P}_k\boldsymbol{S}_j \\ -\boldsymbol{S}_j\boldsymbol{K}_j\boldsymbol{P}_k & -\boldsymbol{S}_j\boldsymbol{K}_j\boldsymbol{P}_k\boldsymbol{S}_j\end{bmatrix}\boldsymbol{\eta}}_{d\boldsymbol{B}_{mor,j}}, \end{aligned} \tag{3.34}$$

where $d\boldsymbol{F}_{motion,j}$ is a six times one matrix, with both the forces and moments on the slice. $d\boldsymbol{A}_{mor,j}$ and $d\boldsymbol{B}_{mor,j}$ are the six times six added mass and damping matrices for the slice, respectively. The total wave inertia and drag forces and the added mass and damping matrices are finally found by summing together the forces from each element. Inserting the new terms from the Morison's equation into the equations of motion (3.10) gives,

$$[-\omega^2(\boldsymbol{M} + \boldsymbol{A}(\omega) + \boldsymbol{A}_{mor}) + i\omega(\boldsymbol{B}(\omega) + \boldsymbol{B}_{mor}(\omega)) + \boldsymbol{C}]\boldsymbol{\eta}(\omega) = \boldsymbol{F}(\omega) + \boldsymbol{F}_{wave}(\omega), \tag{3.35}$$

which quickly can be solved for the motions, as described in Section 3.1.2.

3.2.8   Added Mass and Drag Coefficients

The added mass and drag coefficients depend, among others, on the roughness of the cylinder, the Reynolds number,

$$Re = \frac{u_0 D}{\nu}, \tag{3.36}$$

and the Keulegan-Carpenter number,

$$KC = \frac{u_0 T}{D}, \tag{3.37}$$

where u_0 is the wave particle amplitude velocity, ν is the kinematic viscosity of sea water and T is the wave period.

Literature often describe the flow by the parameter β defined as,

$$\beta = \frac{Re}{KC} = \frac{D^2}{\nu T}. \tag{3.38}$$

Suggestions of values for the added mass and the drag coefficients are given in the *DNV GL* recommended practice: Environmental conditions and environmental loads (DNV GL AS, 2019a). The coefficients depend on the roughness, Reynolds number, and the KC number. Sarpkaya (1986) also presents mass and drag coefficients for circular cylinders at low KC numbers. The coefficients are found from experiments and given as a function of β and KC number.

The Reynolds number and KC number depend on the size of the diameter, the waves, and the depth. Hence, the effect of different sea states and cylinder diameters is checked, and the added mass and drag coefficients found. For simplicity, one added mass coefficient and one drag coefficient are chosen for each member, even though the bracing have varying depth. Further, the relative flow motion formulation of the drag term in Morison's equation (3.25) is not always valid if the motions of the member are lower than the diameter (DNV GL AS, 2019a). However, this formulation is used in this thesis. When calculating the Reynolds number and KC number, the motions of the structure are neglected. Lastly, all cylinders are assumed to be smooth.

Using the sea states as defined from the LIFES50+ report by Yu et al. (2018) and varying the draft and diameters, the KC number and Reynolds numbers where calculated and the values for the added mass and drag coefficients found. For the pontoons, with a diameter between 2 and 4 meters, at a depth of 15 to 20 meters, the Reynolds number is high ($Re > 10^6$) and $1 < KC < 8$. Using DNV GL AS (2019a) and Sarpkaya (1986), both result in $C_M \approx 2.0$ for all conditions. For the drag coefficient, *DNV GL* gives $C_D = 0.65$, while reading of Sarpkaya gives $0.8 < C_D < 1.2$. For the bracing, similar results were obtained.

4   Method

4.1   Choice and Definitions of FWT Floater Baseline Design

It was decided to use the WindFloat semi-submersible as a baseline design for the thesis. This design was chosen based on the comparison of existing designs given in Section 2.2. Advantages of the WindFloat design are that the WT is directly supported by a column, it has only three columns, and the WT is mounted over one of the side columns instead of in the center for easier mounting.

A global Earth-fixed coordinate system with the origin at the geometrical center of the water-plane area when the model is in calm water is defined. The x-axis is pointing towards the wind turbine, and the z-axis is pointing upwards with $z = 0$ at the mean sea level. The y-axis is defined from the right-handed coordinate system. The rotations around the axes are defined positive by the right-hand rule. This coordinate system is used for all of the calculations in the thesis.

The coordinate system and names of the main elements of the WindFloat concept are shown in Figure 4.1a and a three-dimensional model is shown in Figure 4.1b.
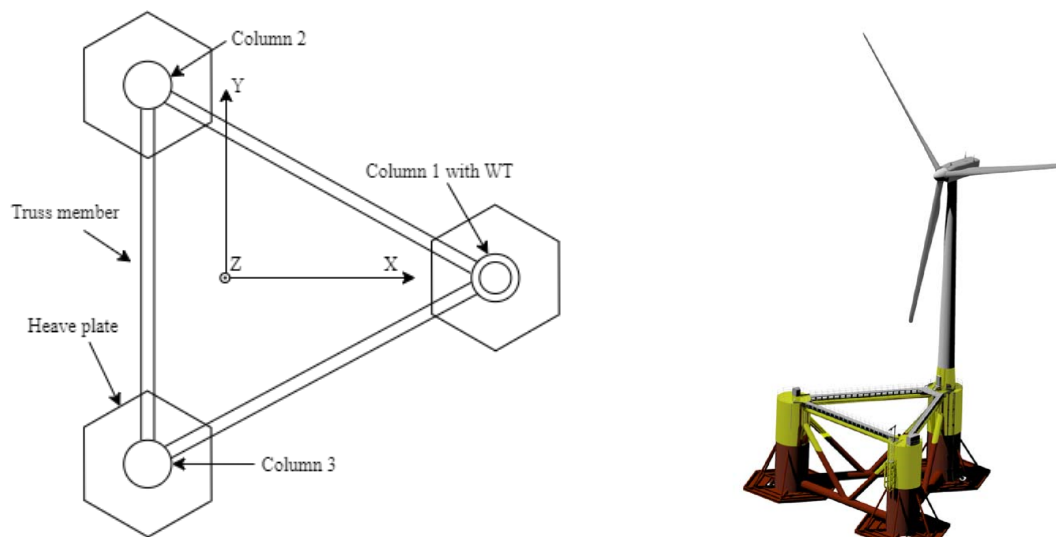
(a) Illustration of the WindFloat concept seen from above. The z-axis points out of the plane.

(b) WindFloat (Roddier, Peiffer, et al., 2011).

Figure 4.1: In (a), the WindFloat concept is illustrated from above with the names and the defined coordinate system. The z-axis points out of the plane and $z = 0$ at the mean sea level. In (b), a three-dimensional model of the WindFloat concept is shown.

The WindFloat concept consists of three columns, with the WT at column one. Each column has a hexagonal heave plate at the lower end. The columns are connected by the truss members, consisting of three horizontal beams at the top of the columns, three horizontal pontoons at the bottom of the columns, and six bracings connected between the pontoons and the columns. The columns and truss members form an equilateral triangle. The main dimensions are further explained in Section 4.6.1.

4.2   Procedure

To evaluating how different design parameters influence the wave-induced responses of the semi-submersible FWT design, hydrodynamic analyses are carried out in the frequency domain to simplify calculations and save computational time. To calculate the first-order, potential theory added mass, damping, and excitation loads, the *DNV GL* software package *Sesam* is used. Mainly the programs *GeniE* and *HydroD* are used for modeling and analyzing the structure, respectively. In the calculations with *Sesam*, the truss members are not included for two reasons. One is for not creating a too complex panel model, and the other because of their relatively small influence on the wave-radiation/diffraction problem (Karimi et al., 2017). The wave loads on the truss members are calculated in *MATLAB* using Morison's equation, see Section 3.2.7. Morison's equation is also used for calculating the viscous forces on the heave plates.

The design parameters are adjusted, mass and hydrostatic properties are calculated, and the design criteria checked in *MATLAB*. Command files are written for running *GeniE* and *HydroD* in batch mode from *MATLAB*. When all required matrices are found, the motion RAOs and internal hull loads are calculated with *MATLAB*. All post-processing is carried out in *MATLAB*. The main script for the calculations in *MATLAB* is given in Section D.1.

4.2.1   GeniE

GeniE is part of the *Sesam* system package and could be used for modeling, structural analysis, code checking, and presentation of results (DNV GL AS, 2019c). In this thesis, the *GeniE* software (DNV GL AS, 2019b) is used to create panel finite element models of the FWT support structures for the hydrodynamic analyses executed in *HydroD*. Only the structure below the waterline is necessary for the calculations in *HydroD*. Further, if the model is symmetric about the xz- and/or yz-plane only half/one-fourth of the panel model is necessary to model in *GeniE*, and this will save computational time in *HydroD*. All panels have to have the wet surface property load defined as load case number one. The largest element diagonal should be smaller than 1/6 of the smallest wavelength analyzed, large changes in element size for neighboring elements should be avoided, and small element sizes are important close to the surface and sharp edges (DNV GL AS, 2019d).

The panel models are created in *GeniE* by writing the draft, the column diameter, the distance between the columns, the length of the heave plate edge, the heave plate thickness, and the mesh densities to the command file from *MATLAB*. The mesh is automatically generated by *GeniE*, based on the defined mesh densities. Feature edges are used to control the mesh. An example of the model and mesh created with *GeniE* is shown in Figure 4.2. It is seen that smaller elements are used close to the heave plate edge. The effect of different mesh densities is discussed in Section 4.7.2.

A problem when meshing the heave plates in *GeniE* was the small element size required close to the heave plate edges, to avoid large changes in neighboring element sizes. From the doctoral thesis by Kvittem (2014), who studied the fatigue design of a 5 MW FWT inspired by the WindFloat concept, a 0.05 meters effective thickness of the heave plates is reported. However, using this thickness implies elements with this size close to the heave plate edges and too many elements overall, which increases the computational time. Cermelli et al. (2009) modeled the heave plates of the WindFloat concept as dipole panels with zero thickness in *WAMIT*, since they are thin elements. However, this is not a possibility in *Sesam*. Vangdal (2019) also models the 5 MW WindFloat in *GeniE*, and calculates the hydrodynamic coefficients in *HydroD* for analyzing FWTs in extreme conditions. Vangdal suggests using a heave plate thickness of 0.4 meters, based on obtaining the same diameter/thickness ratio as used in the experiments by Moreno et al. (2016). This thickness is also used in this thesis.

4.2.2   HydroD and Wadam

HydroD (DNV GL AS, 2017a) is part of the *Sesam* system package, and is used for wave load and stability analysis of fixed and floating structures (DNV GL AS, 2017b). The wave loads and motions are computed by *Wadam* or *Wasim*, which are also part of *Sesam* package, and run in batch mode from *HydroD*. *Wadam* could be used for structures of arbitrary shape, while *Wasim* is used for vessels.

In this thesis, *Wadam* (DNV GL AS, 2019e) is used for calculating the wave loads on the FWT hull in the frequency domain. *Wadam* stands for Wave Analysis by Diffraction and Morison Theory (DNV GL AS, 2019d), and uses Morison's equation and first- and second-order three-dimensional potential theory for calculating the wave loads (DNV GL AS, 2017b). In this thesis, only first-order potential theory is used and global response analyses are carried out for obtaining the added mass, damping, and wave loads on the columns with heave plates. Also, the pressure distribution on the panels is written to the result file to be used for the calculations of internal hull loads.

The environmental conditions are defined in *HydroD*. These are the draft, seawater properties, and air properties. The angular wave frequencies used for the calculations are defined. For the thesis, 33 wave frequencies going from 0.05 rad/s to 1.3 rad/s with steps of 0.05 rad/s, and from 1.4 rad/s to 2 rad/s with steps of 0.1 rad/s are used. The wave frequencies were selected based on what was found to be the most interesting range, while not using too many frequencies to decrease the computational time. The waves propagate along the positive x-axis. The mass properties, including mass, radii of gyration, and specific product of inertia are written to the *HydroD* command file from *MATLAB*.
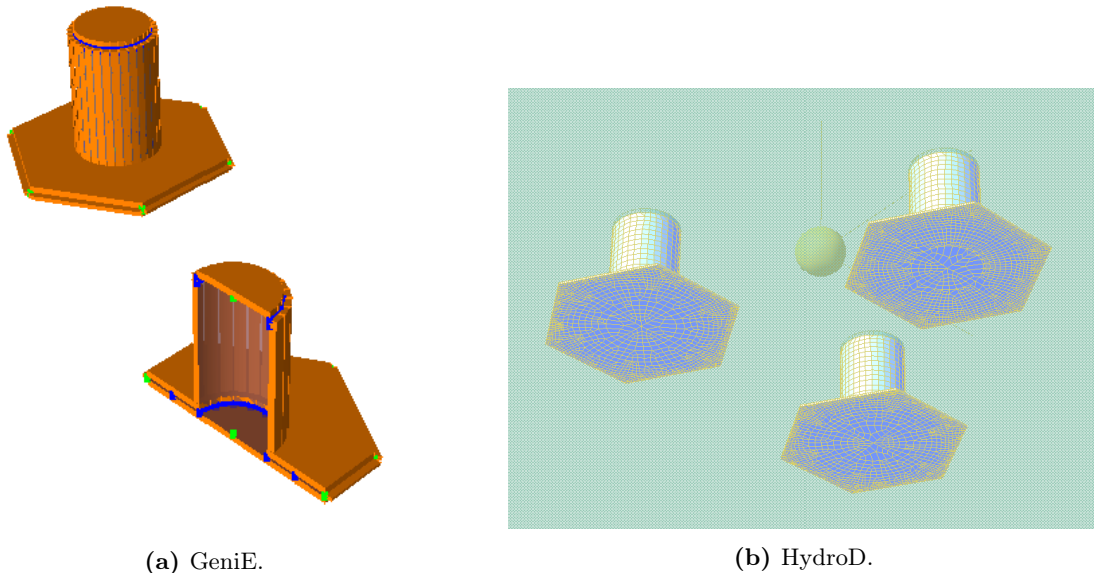
(a) GeniE.

(b) HydroD.

Figure 4.2: Screenshots of the WindFloat model in *GeniE* and *HydroD*. The wet surface is shown by the orange elements in *GeniE*. The mesh is seen in the *HydroD* screenshot, with the surface in light green.

4.2.3   MATLAB

MATLAB (The MathWorks Inc., 2016) is used for calculating the mass and hydrostatic properties of the FWT structure. It is also used for calculating the wave loads on the truss members and viscous loads on the heave plates with Morison's equation and the coefficients given in Ta-

ble 4.4. *MATLAB* calculates the motions and internal hull loads, explained in Section 3.1.2 and Section 4.2.4, respectively.

The total displacement, center of gravity, radii of gyration, and product of inertia of the structure are calculated in *MATLAB* to create the six times six mass matrix, as explained in Section 3.1.1. The mass displacement is also calculated with a heave plate thickness of 0.4 meters to be used for the calculations in *HydroD*. The restoring matrix is also calculated in *MATLAB*, as given in Section 3.2.3. These matrices are calculated by the code given in Section D.2. The codes for calculating Morison's equation and the internal hull loads are given in Section D.3 and Section D.4, respectively.

For the heave plates, only the viscous loads are calculated since the inertia loads are calculated by potential theory in *Wadam*. The viscous effect of the heave plates is included because of their important damping effect, especially at low frequencies where potential damping is low. Only the viscous force in the z-direction is calculated for the heave plates since the thickness is low. The water particle velocity at the center of the heave plates is used, as the heave plates are most important in long waves, hence, one could assume the same velocity field under the entire heave plate. Instead of using the diameter and the step length, h, the drag loads are calculated by multiplying by the projected area of the heave plate.

A wave amplitude of one meter is used for all the calculations with Morison's equation, to include the matrices in the calculations of the RAOs. However, if finding the exact responses was the main objective, a wave spectrum should have been defined, and the motions and wave loads should have been calculated in irregular waves to get a more realistic result.

The added mass and damping matrices are linearly interpolated between the frequencies calculated in *Wadam*. The coefficients are found for 15 new frequencies between the frequencies calculated in *Wadam* for a better resolution of the final responses. The excitation loads are interpolated using spline interpolation in *MATLAB*, and the real and imaginary parts are interpolated individually. Morison's equation is calculated for the same frequencies as in *Wadam*, the output is then interpolated in the same manner as for the results from *Wadam*.

When all of the matrices are found and interpolated, the equations of motions are solved in *MATLAB* as explained in Section 3.1.2. After the motion RAOs are calculated, the internal hull loads could be calculated.

4.2.4 Internal Hull Loads

Only comparing the motion responses of the different designs is not sufficient. For instance, for a semi-submersible platform, the potential excitation force in the heave is zero for certain wave frequencies due to cancellation effects between the columns/pontoons. However, in these cases, the internal force between the pontoons is large (DNV GL AS, 2018). This force is called the split force and is illustrated in Figure 4.3.
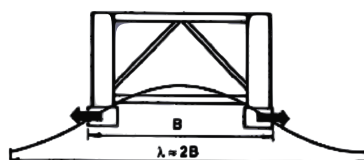
Figure 4.3: Split force between pontoons (DNV GL AS, 2018).

Since the waves are propagating in the positive x-direction, only forces in x- and z-direction and bending moment about the y-axis are of interest. The procedure is inspired by the time domain

method for calculating forces and moments in FWT hulls developed by Luan, Chabaud, et al. (2017) and Luan, Gao, et al. (2017), only that in this thesis the calculations are carried out in the frequency domain and more simplified. The internal loads of the FWT structures are calculated in a cross-section in the yz-plane at $x = 0$, and with the bending moment calculated about the origin of the coordinate system. The cross-section divides the platform into part A and part B, whereas part A includes the components with positive x-coordinates. The forces in x- and z-direction, and the bending moment in the cross-section are found by knowing that the sectional loads must be in equilibrium to the external and inertia loads acting on the column with the WT (part A). The same if part B was considered.

$$\boldsymbol{F}_{CS} + \boldsymbol{F}_{ex} = \boldsymbol{F}_I. \tag{4.1}$$

$\boldsymbol{F}_{CS}$, $\boldsymbol{F}_{ex}$, and $\boldsymbol{F}_I$ are the cross-sectional loads, external loads, and inertia loads, respectively, and are all six times one matrices consisting of complex numbers, and depending on the wave frequency. The external loads consist of wave excitation loads, radiation loads, hydrostatic pressure loads, viscous drag loads, gravitational loads, and atmospheric pressure loads (Luan, Chabaud, et al., 2017). In this work, the gravitational loads and atmospheric pressure loads are not included since it is assumed that the gravitational loads are balanced by the buoyancy loads, however, the variation of the buoyancy loads are accounted for as restoring loads. It is assumed atmospheric pressure inside the columns, canceling the need to include this in the calculations. Only first-order wave excitation loads are included, except viscous loads on the heave plate. The hull and WT are assumed to be rigid bodies, so hydroelastic effects and structural flexibility are neglected. Further, external and inertia loads on the bracing, beams, and pontoons on the positive side of the cross-section are also neglected. *Wadam* writes the pressure transfer functions on the panels to the result file. The loads on the structure from the pressure on the panels could then be calculated as,

$$\boldsymbol{F}_p = \begin{bmatrix} \Sigma_{k=1}^{k=N} \, p_k \, \overrightarrow{\boldsymbol{n}_k} \, A_k \\ \Sigma_{k=1}^{k=N} \, p_k \, \boldsymbol{r}_k \times \overrightarrow{\boldsymbol{n}_k} \, A_k \end{bmatrix}, \tag{4.2}$$

where p_k is the complex pressure at panel k, $\overrightarrow{\boldsymbol{n}_k}$ is the unit normal vector of the panel pointing from the fluid onto the wet panel sides, $\boldsymbol{r}_k = \begin{bmatrix} x & y & z \end{bmatrix}^T$ are the centroidal coordinates of the panel in the global coordinate system, A_k is the wet area of the panel, and N is the number of panels. When cross-sectional loads are calculated, only the panels on column 1 are included in the summations.

The pressure transfer functions include both the diffraction and radiation problem, while fluctuating hydrostatic pressures due to the body motions are not included (DNV GL AS, 2019d). Therefore, the pressure loads contain the following terms,

$$\boldsymbol{F}_p = \boldsymbol{F}_{excitation} - \boldsymbol{A}\ddot{\boldsymbol{\eta}} - \boldsymbol{B}\dot{\boldsymbol{\eta}}. \tag{4.3}$$

The pressures written to the result file are calculated after the motion RAOs are found since they contain the radiation pressure loads. The model and RAOs calculated by *Wadam* are not correct, since the slender elements and viscous forces are not accounted for, yielding large motions around resonance. Therefore, each hull design has been analyzed two times. The second time the damping matrix calculated with Morison's equation is added to the analysis in *Wadam*, to obtain RAOs closer to the one calculated in *MATLAB* and radiation pressure loads closer to

the real solution. This can be seen in Figure 4.8c, where the radiation loads are calculated for the first and second *Wadam* run, and when using the RAOs calculated after Morison's equation is included. However, there will still be a small error as the Morison damping varies for different frequencies, and only the damping matrix at heave natural frequency is used as input to *Wadam* for all frequencies. Further, the mass and stiffness matrices in *Wadam* are not entirely correct either, also influencing the RAOs calculated by *Wadam*.

The restoring loads are calculated manually, since they are not included in the pressure distribution on the panel model. Only restoring loads on the column are calculated and only in heave and pitch direction. Restoring loads from mooring are neglected since the mooring system is not designed in this thesis. The restoring loads are calculated as,

$$F_{c,3} = -\rho g A_w(\eta_3 + y\eta_4 - x\eta_5), \tag{4.4}$$

$$F_{c,5} = -xF_{c,3} - (\rho g V_{partA} z_{B,partA} - m_{partA} g z_{G,partA})\eta_5, \tag{4.5}$$

where A_w is the waterplane area of the column, x and y are the mean global coordinates of the column. V_{partA}, m_{partA}, $z_{B,partA}$, and $z_{G,partA}$ are the wet volume, mass, z-coordinate of center of buoyancy and center of gravity for the part A, respectively. Part A contains the column, heave plate, WT, and ballast in column 1.

The inertia loads are calculated for part A, using the center of gravity of each component j as the point where the inertia loads are calculated. The inertia forces in x- and z-direction, and inertia moment about y are calculated as,

$$F_{I,1,j} = -\omega^2 m_j(\eta_1 + z_j\eta_5 - y_j\eta_6), \tag{4.6}$$

$$F_{I,3,j} = -\omega^2 m_j(\eta_3 + y_j\eta_4 - x_j\eta_5), \tag{4.7}$$

$$F_{I,5,j} = z_j F_{I,1,j} - x_j F_{I,3,j}, \tag{4.8}$$

where m_j is the mass of component j, and x_j, y_j, z_j are the coordinates of the center of gravity for each component. The total inertia loads are found by summing up the loads from each component. The ballast is assumed a solid mass only contributing to inertia loads, and the effects of free surface or hydrostatic pressure are neglected.

The viscous loads on the heave plate are also included in the calculations as,

$$\boldsymbol{F}_{morison,HP} = \boldsymbol{F}_{drag,HP} - i\omega \boldsymbol{B}_{morison,HP}\boldsymbol{\eta}, \tag{4.9}$$

where $\boldsymbol{F}_{drag,HP}$ are the drag loads on the heave plate and $\boldsymbol{B}_{morison,HP}$ is the damping matrix from Morison's equation for the heave plate.

Finally, the loads in the cross section can then be calculated as,

$$\boldsymbol{F}_{CS} = \boldsymbol{F}_I - (\boldsymbol{F}_P + \boldsymbol{F}_c + \boldsymbol{F}_{morison,HP}). \tag{4.10}$$

The different calculations of the section loads are verified in Section 4.7.3 and the *MATLAB* code is given in Section D.4.

4.2.5   Mean Tilt Angle

In first-order potential theory, the pressure forces are calculated on the mean wet body of the structure, in other words, up to the mean sea level (DNV GL AS, 2019d). In most studies, first-order effects are calculated using a first-order potential theory program and modeling the structure in upright position. However, for a FWT structure the mean position during operation is not upright. Because of the wind loads on the blades and tower, a FWT structure normally operate under a constant pitch angle. Therefore, the influence of modeling and calculating first-order effects on a tilted model is also investigated in this thesis.

When wind loads act on the structure, the displacement of the structure is not increased. Therefore, the point of rotation has to maintain the same volume displacement of the structure. Neglecting the bracing, the point of rotation is found to be about the y-axis at the origin, being at the MSL. The origin is the upright waterplane center.

For the analyses, the mass and stiffness matrices are kept constant. The radii of gyration will not change, while the center of mass will move, but the difference is neglected. For the restoring coefficients, it is assumed small angles of inclination and the restoring coefficients are assumed constant. The start and end points for the slender elements calculated with Morison's equation are moved based on rotation of axes. For the pontoons and heave plates, the new x- and z-coordinates are calculated as,

$$x_{new} = x\cos(\theta) + z\sin(\theta), \tag{4.11}$$
$$z_{new} = -x\sin(\theta) + z\cos(\theta), \tag{4.12}$$

where θ is the tilt angle about the y-axis. For the bracing, the start point at the pontoons were shifted as above, while the end point was controlled if under water and stopped at the column or stopped at the free surface. Therefore, the y-coordinates were also changed. For the heave plates, a normal vector was introduced as $\overrightarrow{n_k} = \begin{bmatrix} \cos(\theta) & 0 & -\sin(\theta) \end{bmatrix}^T$. For the cases of zero tilt, the heave plates will only contribute with viscous forces in the z-direction, while with tilt there will also be viscous forces in the x-direction.

For the analyses with the *Sesam* package, the model is rotated in *GeniE* about the y-axis and the structure is cut at the free surface. Feature edges are assigned the columns at the free surface for controlling the mesh.

4.3   10 MW Reference Wind Turbine

The DTU 10 MW Reference Wind Turbine (DTU 10MW RWT) is used for the calculations of the upscaled 10 MW WindFloat concept. The reference wind turbine was designed for the Light Rotor project by DTU Wind Energy and Vestas. It was designed for offshore-siting for an IEC wind class 1A, being the highest class, as future sites for such a large WT were assumed to be offshore. Further, the reference wind turbine is a traditional three-bladed, upwind wind turbine. The DTU 10MW RWT is described by Bak et al. (2013) and the main parameters are summarized in Table 4.1.

Table 4.1: Main parameters of the DTU 10 MW Reference Wind Turbine (Bak et al., 2013). The origin of the coordinate system for the centers of gravity, COG, is placed at the center of the tower base, with the x-axis pointing downwind and z-axis upwards.

Parameter	Value
Rated power [MW]	10
Rated thrust, $F_{T,rated}$ [kN]	1 500
Cut-in, rated and cut-out wind speed [m/s]	4, 11.4, 25
Number of blades [-]	3
Rotor diameter [m]	178.3
Hub height, Z_{hub} [m]	119.0
Hub overhang [m]	7.1
Rotor mass [kg]	227 962
Rotor COG [m]	(-7.07, 0.00, 119.00)
Nacelle mass [kg]	446 036
Nacelle COG [m]	(2.69, 0.00, 118.08)
Tower mass [kg]	628 442
Tower height [m]	115.63

However, as the wind turbine is mounted on top of a freely floating structure in this thesis and DTU 10MW RWT describes a land-based tower, the dimensions of the tower were modified since a floating substructure presents a lower stiffness compared to rigid ground. Yu et al. (2018) present two modified towers for the DTU 10 MW RWT used on the 10 MW OO-Star and NAUTILUS structures in the LIFES50+ project. Both the outer diameters and wall thicknesses are increased compared to the DTU 10MW RWT tower, to increase the stiffness of the tower and avoid fatigue damages. Further, it is desired to keep the hub height as the distance above MSL. Therefore, the lower part of the tower is replaced by the freeboard of the platform. The properties of the towers for the LIFES50+ structures are given in Table 4.2. The steel density of the towers is increased to account for secondary structures as bolts, stiffeners, flanges, etc.

Table 4.2: Tower properties given for the LIFES50+ 10 MW structures (Yu et al., 2018).

Parameter	OO-Star	NAUTILUS
Elevation of tower top above MSL [m]	115.63	115.63
Density [kg/m^3]	8 243	8 500
Tower height [m]	104.63	107
Tower base outer diameter [m]	11.5	10.5
Tower top outer diameter [m]	5.4	5.5
Wall thickness, base - top [m]	0.075 - 0.029	0.040 - 0.037
Total mass [kg]	1 257 000	879 381
Vertical center of mass above MSL [m]	49.8	54.9

The diameter of the towers varies linearly with the height. For OO-Star, the thickness is constant for each segment, while it is assumed that the thickness varies linearly for the NAUTILUS tower. Since the freeboard is a variable for the upscaled WindFloat design, the height of the tower could vary. Therefore, the weight of the tower is found by calculating the volume of the tower as a truncated hollow cone cylinder with a constant thickness equal to 0.04 meters. Further calculations are based on the values for the NAUTILUS tower, as this is also a steel structure

and the weight of the tower is easier to calculate. The tower base diameter is interpolated based on the difference in tower height between the desired height and the NAUTILUS tower height.

4.4   Environmental Conditions

Three environmental conditions (ECs) are defined, to evaluate the RAOs in different conditions. A sea state could be described by the significant wave height and the peak period. The significant wave height is defined as the average wave height of the one-third largest waves in the sea state and the peak period is the period of the wave spectrum peak. Three widely different environmental conditions are defined in Table 4.3. The values are taken from Faltinsen (1990), and give annual sea state occurrences and corresponding values for mean wind, wave height and period for the North Atlantic and North Pacific. The two first describe typical sea states, both with around 20 % probability of occurrence. EC3 is an extreme condition with about 1 % probability of occurrence.

Table 4.3: The three environmental conditions (EC) defined. The mean wind speed, $\overline{U}$, is given at hub height, and the corresponding significant wave height, H_s, and wave peak period, T_p are taken from Faltinsen (1990, p. 32).

Environmental condition	Type	$\overline{U}$ [m/s]	H_s [m]	T_p [sec]
EC1	Calm	9	0.88	7.5
EC2	Moderate	16	3.25	9.7
EC3	Rare	39	11.5	16.4

There exist several wave spectra for describing the sea surface. The Pierson-Moskowitz (PM) spectrum and JONSWAP (Joint North Sea Wave Project) are the most commonly used for describing wind-generated seas. The PM spectrum is based on data from the North Atlantic Ocean and used for a fully-developed sea. The JONSWAP spectrum is based on the PM spectrum, but with a higher peak around the peak frequency to give a better fit to the North Sea data collected. The JONSWAP spectrum is often used to describe developing sea states (Pettersen, 2007). When swell components also are important, a two peak spectrum may be applied (DNV GL AS, 2019a). In this thesis, the JONSWAP spectrum, as defined in DNV GL AS (2019a) is used. However, based on the values for significant wave height and peak period, the PM spectrum is used for EC1 and EC2 since they lay outside the recommended JONSWAP area. The wave spectra for the three environmental conditions are shown in Figure 4.4.
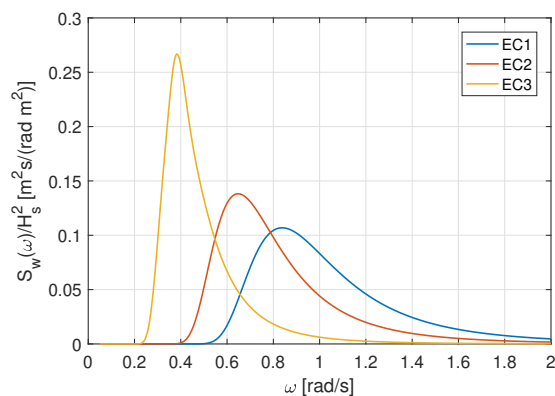
Figure 4.4: Wave spectra for the three different environmental conditions. The wave spectra are normalized by dividing on the significant wave height squared.

All three conditions show a rapid drop in the wave spectrum for frequencies lower than the peak frequency, meaning it is little energy in the low-frequency waves. For EC1 and EC2, the wave spectra are almost zero when $\omega < 0.4$ rad/s or $T_w > 15$ seconds. In the extreme condition, EC3, the energy is almost zero for $\omega < 0.25$ rad/s or $T_w > 25$ seconds. All spectra decrease with ω^{-5} for high frequencies. From the figure, it could be assumed that in most conditions the wave energy is distributed in the interval $0.3 < \omega < 1.4$ rad/s or $5 < T_w < 20$ seconds, and in the following text this will be referred to as the wave energy range.

4.5 Design Criteria

Some design criteria are defined in this section to make sure the proposed designs are feasible, and for evaluating the different hull designs.

4.5.1 Static Pitch Angle

The mean wind turbine thrust overturning moment could be considered the most important design driver for a FWT hull (Cruz and Atcheson, 2016). The moment gives a static pitch angle, which reduces the projected area of the WT blades and decreases the effect of the WT. Therefore, it is desired to keep the maximum static pitch angle below 10 degrees for a ballast condition as for zero wind. Active ballast could be used to reduce the mean tilt angle, but the effects of active ballast are not included in this thesis.

The demand to the maximum static pitch angle gives a requirement for the pitch restoring coefficient, assuming small inclination angles and minimal coupling with surge,

$$C_{55} \geq \frac{M_I}{\eta_{5,max}}. \tag{4.13}$$

Where M_I is the overturning moment, calculated as,

$$M_I = F_{T,rated} z_{hub} \cos \eta_5 \tag{4.14}$$

where $F_{T,rated}$ is the rated thrust and z_{hub} is the moment arm, taken as the distance from MSL to the hub since the coordinate system has its origin at MSL. Using $\eta_5 = 0$ radians gives the highest inclining moment, and thus the highest demand for the restoring coefficient. The drag force on the wind tower is assumed negligible in comparison to the thrust force at rated wind, as shown for the 5 MW NREL WT by Luan, Gao, et al. (2016).

4.5.2 Natural Periods

It is desired to keep the natural periods of the structure outside the wave energy range. This depends on the site location and weather, but waves contain the most energy typically in the range 5 to 20 seconds, see Section 4.4. Therefore, the minimum natural period should be above 20 seconds.

Semi-submersible platforms typically have a heave natural period in the area above 20 seconds, and above 30 seconds in roll and pitch. The natural periods in the horizontal degrees surge, sway and yaw are controlled by the mooring system since a freely floating platform does not have restoring forces in these modes as seen in Section 3.2.3. Typically, these modes have natural periods around 100 seconds. For a semi-submersible platform, the heave natural period is the most difficult to maintain outside the wave energy range and will be the critical natural period to control.

Further, it is not desired that the rigid body natural periods are close to the excitation periods of

the wind turbine. For the DTU 10MW RWT, the minimum rotor speed is 6 rpm, corresponding to a rotation period of 10 seconds. The 3P period is then 3.33 seconds, and these periods will not be coupled with the natural motion periods of the structure since these will be above 20 seconds. Calculations of the natural periods of the tower are not included in this thesis since a rigid body is assumed.

4.5.3   Floating Stability

The requirements from the DNV GL AS (2018) standard for floating wind turbine structures could be used for the semi-submersible support structure to ensure sufficient intact floating stability. The standard states the following for intact stability of semi-submersibles (DNV GL AS, 2018, p. 130):

- "The area under the righting moment curve to the second intercept or downflooding angle, whichever is less, shall be equal to or greater than 130 % of the area under the wind heeling moment curve to the same limiting angle."

- "The righting moment curve shall be positive over the entire range of angles from upright to the second intercept."
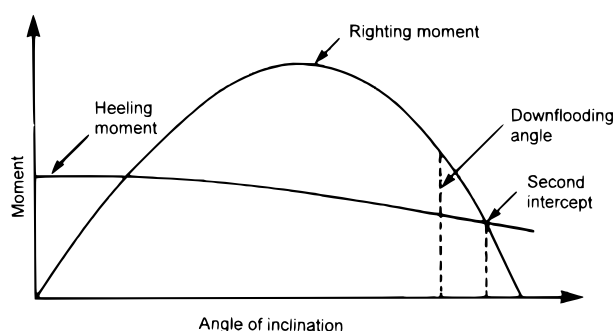
Figure 4.5: Definition of righting moment and wind heeling moment curves from DNV GL AS (2018).

The requirement of a maximum static pitch angle below 10 degrees means that the first intercept is below 10 degrees. This implies that most likely the requirements for intact stability are fulfilled, based on guidance with supervisor Erin Bachynski. Therefore, the requirements are not checked for the designs but could be controlled by stability calculations in *HydroD*. This is not carried out in this thesis due to time limitations.

Further, the DNV GL standard states that there are no requirements to damage stability for unmanned units. However, they advise to perform collision analysis and fulfill the recommended damage stability requirements given in the standard, however, this is not part of this thesis.

4.5.4   Other Criteria

Besides the given criteria, it is also desired to:

- Minimize the hull weight, to reduce the material cost.

- Keep outer dimensions within reasonable size, so the platform could be constructed in most shipyard docks.

- Minimize structure motions, especially high nacelle accelerations will cause fatigue damages and decrease the lifetime of the WT.

- The draft should be kept relatively low, to maintain the advantages of a semi-submersible

platform. Which is it can be towed in shallow waters and mounting of WT could take place at quayside.

4.6   Design Parameters

This section describes the main dimensions of the WindFloat hull, to understand which parameters are interesting to vary in the parametric study. The section also presents general assumptions about the design and assumptions for the analyses.

4.6.1   Main Dimensions

Wind Turbine

The rotor-nacelle-assembly, RNA, of the DTU 10 MW RWT is kept constant, while the tower mass and the outer base diameter depend on the freeboard of the structure, as explained in Section 4.3. Changing the length of the tower could shift the natural frequency of the tower to undesired frequencies, but this is not accounted for in this thesis since the entire structure is assumed a rigid body.

Columns

The displaced volume of the main columns is the main contributor to the volume displacement of the structure. The columns could be described by the diameter, freeboard, and draft.

The diameter of the main columns influences the waterplane area and inertia, whereas increasing the diameter increases the waterplane area and the metacentric height, $\overline{GM}$, and hence, the restoring coefficients in heave, roll, and pitch. On the other side, a larger diameter will increase some of the wave excitation loads. The column diameter has to be kept larger than the outer diameter of WT tower base.

The height of the main columns ensures sufficient space for ballast and a large enough air gap to avoid green water on the upper deck and slamming forces on the WT tower. Increasing the height/draft give better stability, as more ballast could be used at a lower z-coordinate, lowering the vertical COG. Both increasing the column diameter and height would increase the steel weight making the structure more expensive to produce. For the analyses, the freeboard will be kept constant at 10 meters, unless this gives problems with the deck or beams being to close to the surface when the platform tilts. It is not desired that the deck gets underwater, even though it is constructed waterproof. Also, the beams should be kept above the surface to avoid slamming forces. The relatively low draft of semi-submersibles is one of their main advantages over TLP and spar platforms and should not be increased too much.

Distance between Columns

Increasing the distance between the columns, DCC, gives higher restoring coefficients in roll and pitch, which could be necessary for satisfying the maximum static pitch angle requirement. However, a stiffer system lowers the natural period of these motions, possibly shifting them within the wave energy range. Another downside, a larger distance between the columns implies longer truss members, possibly increasing the bending moments in the truss members and increasing the possibility for fatigue damages. The assumption of rigid body motions will be less valid as DCC increase, and the diameters and thicknesses of the beams, bracings, and pontoons would require larger dimensions. Also, larger outer dimensions of the platform reduce the number of suitable sites for construction and could increase the cost of construction and transportation to operation cite.

Heave Plates

The heave plates increase the added mass and damping in heave, roll, and pitch. Increasing the added mass, increase the natural periods, and could be used to satisfy the criterion to the

natural periods of the structure. However, a minimum spacing between the heave plates is desired to avoid undesired interacting effects. Too large heave plates would also require more reinforcements, and increase steel mass.

The effect of changing the thickness of the heave plates will not be studied in this thesis. They are assumed to be flat plates with a thickness of 0.05 meters and are modeled in *GeniE* with a thickness of 0.4 meters, as explained in Section 4.2.1.

Truss Members
The truss members consist of the beams, bracings, and pontoons that connect the columns, and are important for the structural integrity of the hull. They need to withstand the forces and moments between the columns without breaking or deforming excessively. In this thesis, the body is assumed a rigid body, and only the weight of and the wave loads on the beams, bracings, and pontoons are included. Their dimensions are not varied or optimized in this thesis since this would require a more detailed structural analysis.

The z-coordinates of the centerline of horizontal beams and pontoons are chosen to be one diameter down and up, respectively, from the column ends. The length of the bracings is calculated so the centerline of the beam and bracing cross in the centerline of the main column. On the lower end, the bracing centerlines meet at the center of the pontoons, halfway between the columns. These assumptions are based on photos of the WindFloat design and from guidance with Erin Bachynski.

4.6.2   General Assumptions about the Design

The steel mass of the hull is assumed to be 20 % of the mass displacement, based on guidance with Erin Bachynski and since this is in the range for typical semi-submersible FWT platforms (Luan, Gao, et al., 2016),

$$M_{steel} = 0.2\rho\nabla. \tag{4.15}$$

The steel mass is not calculated based on the steel volume since the thicknesses are unknown. A constant thickness of 3 centimeters is used for all the structural parts, except 5 centimeters for the heave plates, to calculate the steel volume and distribute the estimated steel mass evenly over this volume. Then, the center of gravity of each structural part and globally could be found.

The columns are filled with ballast to make the mass displacement of the entire structure equal to the mass of displaced sea water,

$$M_{ballast} = \rho\nabla - M_{steel} - M_{WT}. \tag{4.16}$$

If the steel mass was to be calculated based on thicknesses this would then only affect the amount of ballast. Since these masses are situated in the same areas, and the mass of ballast is much higher than the steel mass, the effects on the center of gravity and radii of gyration are low. Further, it is cheaper to fill a platform with seawater ballast than using more steel, hence, this is preferable.

For the parametric study, the amount of ballast in each column is adjusted so the center of gravity in the xy-plane equals the center of buoyancy, being in the origin. The ballast is filled from the bottom of the columns, to lower the center of gravity as much as possible, and obtain better stability. When calculating the mass properties, the ballast does not contribute to any free surface effects.

A mooring stiffness in surge is included in the hydrostatic restoring matrix,

$$C_{11} = \frac{F_{T,rated}}{0.15d}, \tag{4.17}$$

where d is the depth on the selected site. The mooring stiffness in other degrees of freedom is neglected. The mooring mass is assumed small compared to total displacement and is also neglected. The moorings system is not included in the analyses due to time limitations, but could be an interesting parameter to include in future parametric studies.

When the main dimensions are varied, several controls are conducted to ensure a feasible design before analyses are conducted in *Sesam*. It is checked that there are no collisions between the components and that the design criteria are met. The amount of ballast is controlled and the critical pitch angles calculated. The critical pitch angles are defined as the pitch angles when the beams or deck get submerged or the pontoons or heave plates breach the surface. These angles should be above 10 degrees. D_{hp}/D_{col} is kept above 1.6, so the drag coefficient is not affected by the column boundary layer as found in Section 2.5.

The heave uncoupled, natural period is estimated based on the input parameters to ensure that the period is above 20 seconds before the design is analyzed in *Wadam*. The heave added mass is estimated by calculating the theoretical added mass of the column-heave plate structure (equation (2.5)) multiplied with the number of columns. The added mass of the pontoons is included using strip theory and $C_a = 1.0$ (DNV GL AS, 2019a).

4.6.3   Assumptions for the Analyses

The waterplane area of the structure is rotationally symmetric about the z-axis. Therefore, the metacentric height in roll and pitch is the same and is independent of the axis of rotation. Therefore, the stability of the platform is independent of the axis of rotation. However, the wave forces may vary depending on the direction and the roll and pitch inertia are not necessarily equal. Anyways, in the thesis, all the analyzes are carried out with waves propagating along the positive x-axis. Except for the cases where a mean negative tilt angle is introduced, then the waves propagate in the negative x-direction. A depth of 320 meters is always used, taken from Kvittem (2014).

The wind turbine is only included in the analyses as a point mass, lifting the center of gravity. The effects of wind loads or aerodynamic damping are not included in the thesis due to time limitations.

For the bracings and pontoons, the added mass and drag coefficients are set to one, similar to what done by Kvittem (2014). This also agrees with the coefficients found in Section 3.2.8, only with a slightly larger drag coefficient. Kvittem (2014) overestimated the drag coefficients, to overestimate the wave drag loads. However, it is found that this has minimal impact on the results since inertia forces are dominant.

The viscous drag forces on the heave plates are accounted for with Morison's equation. Since the diameter of the heave plates is relatively large, the KC number will be low. For a motion amplitude of 3 meters, $KC < 0.6$ even with the diameter of the 5 MW WindFloat structure. From the literature study in Section 2.5, the quadratic drag coefficient should then be $C_D > 8$. Kvittem (2014) reports a $C_D = 7.5$ for the heave plates of the 5 MW WindFloat structure, based on a technical report by Principle Power, see Kvittem and Moan (2015). The drag coefficient increases non-linearly with lower KC numbers. It is chosen to continue with $C_D = 7.5$, as a conservative choice for the heave plate. This could underestimate the damping effect of the heave

plates, which is more important than the wave drag forces on the heave plates. The effect of the oscillation frequency is not accounted for, but the dependency is low as seen in Figure 2.4b. On the other side, the dependency will be higher for low submergence-heave plate diameter ratios since free surface effects get more important, then the potential damping will increase. The viscous effects that increase the heave added mass are not included in the thesis as explained in Section 2.5.

Table 4.4: Added mass and drag coefficients used on the different element for the calculations with Morison's equation.

	Pontoons	Bracings	Heave plates (z-direction)
C_a	1.0	1.0	0.0
C_D	1.0	1.0	7.5

4.7   Verification of Procedure

This section describes some of the verification work carried out during the thesis work. First, general verification of the software used and the post-processing is described. Second, the calculation procedure is compared against the 5 MW WindFloat by Roddier, Peiffer, et al. (2011). Third, the calculations of internal loads are verified.

4.7.1   General

To verify that the downloaded *Sesam* software worked, a script modeling and meshing the OC4-DeepCwind in *GeniE* and a script for analyzing the model in *HydroD* was handed by Erin Bachynski. The scripts were used for calculating the hydrodynamic coefficients and excitation loads, and these values were compared against the ones given by Robertson et al. (2014). The results showed good agreement and the procedure used in *Sesam* and the reading of the results to *MATLAB* could be assumed to be correct.

The calculation of the motion RAOs in MATLAB gave the same results as given by *Wadam* when using the same mass and restoring matrices. The calculations with Morison's equation were verified against solving the equation by hand with integration for a vertical, horizontal, and tilted cylinder. Linear interpolation of the excitation forces was first used, however, this gave an unexpected wave shape of the motion RAOs at low frequencies. Therefore, spline interpolation is used on the excitation loads to get a better representation of the amplitudes and phases of the loads.

4.7.2   Comparison of Baseline Design against Literature

To verify the procedure and the codes written for *Sesam* and in *MATLAB*, the motion RAOs for the 5 MW WindFloat concept were calculated and compared with the results presented by Roddier, Peiffer, et al. (2011). The dimensions given by Roddier, Peiffer, et al. (2011) for a 5 MW WindFloat concept were used, see Table 4.5. However, not all required parameters are presented by Roddier, hence, some variables were taken from Kvittem (2014). Some values were given by Erin Bachynski during supervising and others were adjusted to give similar hydrostatic results as presented by Roddier, Peiffer, et al. (2011), see Table 4.6 for these parameters. Roddier, Peiffer, et al. (2011) used the generic 5 MW NREL WT, and the necessary data for the WT is found in the report by Jonkman et al. (2009).

Table 4.5: Main dimensions of the 5 MW WindFloat structure given by Roddier, Peiffer, et al. (2011).

Parameter	Value [m]
Column diameter	10.0
Length of heave plate edge	15.0
Column center to center	46.0
Main beam and pontoon diameter	2.1
Bracing diameter	1.5
Operating draft	17.0
Air gap	10.0

Table 4.6: Assumptions for the 5 MW WindFloat calculations.

Parameter	Value
Turbine tower foundation above MSL [m]	10.0[1]
Pontoon vertical position [m]	-14.9[2]
Thickness of heave plate [m]	0.05[1]
Beam vertical position [m]	7.9[2]
Length of bracing [m]	23.8[2]
Steel weight fraction [-]	0.2[2]
Ballast tank bottom vertical position [m]	-15.5[3]
Ballast fraction at column with WT [-]	0.18[3]

[1] Value taken from Kvittem (2014).

[2] Value taken from guidance with Erin Bachynski.

[3] Value adjusted to give similar results as Roddier, Peiffer, et al. (2011).

Using the assumptions for the positions of the beams, bracing, and pontoons explained in Section 4.6.1, the angle between the pontoon and bracing was 45 degrees, which seems reasonable. The steel weight of the platform was estimated to be 20 % of the displaced mass, as explained in Section 4.6.2. For the Morison elements, $C_a = 1.0$ and $C_D = 1.0$ for the pontoons and bracing, and $C_D = 7.5$ in z-direction for the heave plates were used, as explained in Section 4.6.3. Changing the drag coefficients for the pontoons and bracing to 0.65 was analyzed, which is the value recommended by DNV GL, see Section 3.2.8. This gave negligible changes in damping and wave loads in all degrees of freedom. In surge and sway, potential damping is much more important. In heave, the viscous damping for Morison's equation is most important, but this damping is mainly from the heave plates. Potential excitation forces are much higher than the drag forces in all degrees of freedom. For the comparison, the location and amount of ballast in each column were adjusted to give similar hydrostatic results for the model as given by Roddier, Peiffer, et al. (2011).

The effect of changing the mesh density was studied, where several different mesh sizes were tested. The finest mesh had 9 659 elements and took 4 039 seconds to analyze in *Wadam*, while the coarse mesh had 4 353 elements and took 477 seconds to run in *Wadam*. Intermediate mesh densities were modeled, where the number of elements on the columns and at the heave plates (HPs) was adjusted. The added mass and damping in heave for some of the different mesh densities are shown in Figure 4.6. The fine meshes had a mesh density of 0.6 meters, the medium/fine meshes had a mesh density of 0.8 meters, and the medium and coarse meshes had a mesh density of 1 meter on the columns. The number of elements at the heave plates was

adjusted, by using feature edges between the column and heave plate edges on both sides of the heave plates and give the feature edge a mesh density between the column mesh density and the heave plate thickness.

As mentioned in Section 4.2.1, the heave plates are modeled with a thickness of 0.4 meters, instead of 0.05 meters. The effect of increasing the heave plate thickness to 0.6 meters was studied and is also shown in Figure 4.6 for two different mesh sizes.

(a) Heave added mass.

(b) Heave potential damping.
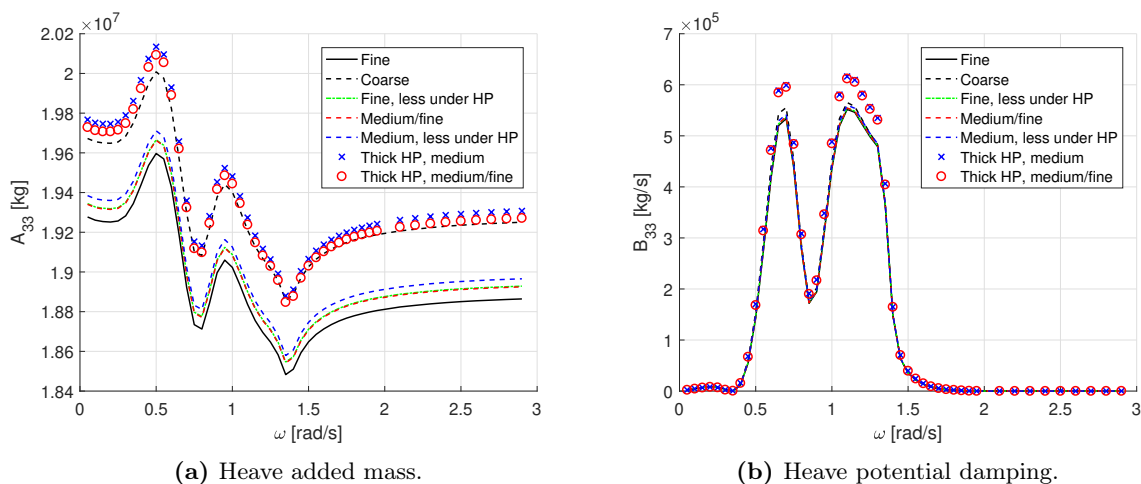
Figure 4.6: The effect of mesh size and heave plate thickness on the heave added mass and damping coefficients are shown for different wave frequencies. The number of elements on the columns and heave plates (HP) was adjusted.

Only the values for heave added mass and damping are given in the figure, as the excitation loads showed similar results as the potential damping. Surge, sway, and yaw coefficients showed small changes, implying that the 1-meter mesh density at the columns is sufficient. The roll and pitch coefficients gave similar results as for heave. It is seen that the heave added mass and damping are almost unaffected by the different mesh sizes, except the coarse mesh, which had a poorly distributed mesh at the heave plates. It was decided to continue with the medium mesh with fewer elements under the heave plate, which had 5 149 elements and took to 889 seconds to run in *Wadam*, since this mesh gave results close enough to the fine mesh at an acceptable computational time.

The heave plates are far under the surface, therefore, they are not so frequency-dependent. This is seen in the figure, as the change in heave added mass is small for different frequencies. The added mass in heave is shifted upwards by an almost constant value when the heave plate thickness is increased. This agrees well with potential theory, where the theoretical added mass coefficient for plates increases when the length in the oscillating direction increase (DNV GL AS, 2019a). However, the change is heave added mass is small and it is assumed that the change in added mass by increasing thickness from 0.05 to 0.4 meters is also small and could be neglected.

The *MATLAB* code calculates the mass and stiffness matrices. A comparison of the hydrostatic data is given in Table 4.7. The computed natural periods and added mass and inertia are compared to Roddier in Table 4.8.

Table 4.7: Comparison of hydrostatic data given by Roddier, Peiffer, et al. (2011) and calculated by the *MATLAB* code.

Parameter	Roddier	MATLAB code
Displacement [kg]	4.64E+06	4.78E+06
COG, (x_G, y_G, z_G) [m]	(-0.278, 0.00, 3.728)	(-0.154, 0.00, 3.723)
Radius of gyration, (r_{xx}, r_{yy}, r_{zz}) [m]	(34.9, 34.7, 26.5)	(34.95, 34.88, 26.24)
Product of inertia, (r_{xy}, r_{xz}, r_{yz}) [m]	-	(0.00, -17.32, 0.00)
Heave restoring coefficient, C_{33} [N/m]	2.37E+06	2.52E+06
Roll restoring coefficient, C_{44} [Nm/rad]	2.83E+08	2.81E+08
Pitch restoring coefficient, C_{55} [Nm/rad]	2.83E+08	2.81E+08

Table 4.8: Comparison of natural periods and added mass and inertia given by Roddier, Peiffer, et al. (2011) and calculated by *Wadam* and Morison's equation. The values for added mass and inertia are taken at the natural period of the motion.

	Roddier		Calculated	
	T_{ni} [sec]	A_{ii} [kg] or [kg-m^2]	T_{ni} [sec]	A_{ii} [kg] or [kg-m^2]
Heave	19.9	1.90E+07	19.7	1.99E+07
Roll	43.3	7.76E+09	44.1	7.95E+09
Pitch	43.2	7.76E+09	44.0	7.95E+09

Overall, the values calculated with *MATLAB* and *Wadam* show good agreement with the results given by Roddier, Peiffer, et al. (2011). The largest relative error is for the heave restoring coefficient with a 6.3 % relative difference. Using only the waterplane area of the columns gives the same C_{33} as Roddier, meaning the difference is in the waterplane area of the bracing, which could have been neglected by Roddier. The added mass and inertia calculated by only *Wadam* gives an even better fit with Roddier, Peiffer, et al. (2011). In general, the calculated added mass and inertia are a bit higher, but with under 5 % relative difference, which could be because of the way the heave plates are modeled. The heave natural period calculated is lower than found by Roddier since the difference in heave stiffness is relatively larger.

The resulting response amplitude operators, RAOs, for surge, heave and pitch given by Roddier, Peiffer, et al. (2011) and the ones calculated with *Wadam* and *MATLAB* are given in Figure 4.7.
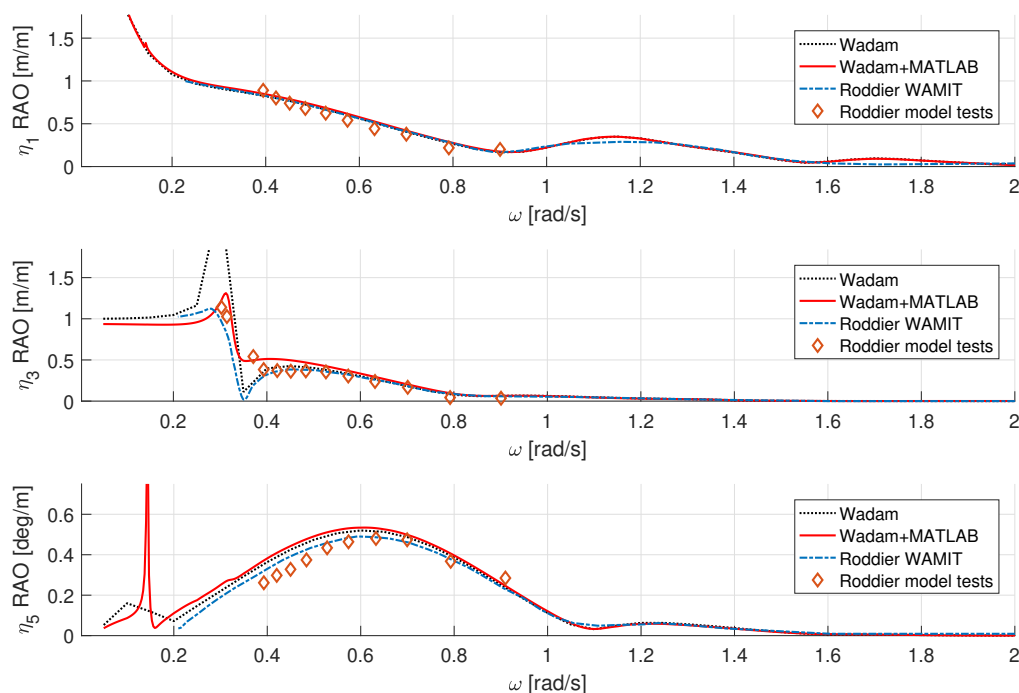
Figure 4.7: The RAOs found by Roddier, Peiffer, et al. (2011) for surge, heave and pitch motion for the 5 MW WindFloat structure, compared against those calculated with *Wadam* and *MATLAB*.

The RAO calculated by *Wadam* overestimates the motions in heave at resonance since viscous drag forces are not accounted for in potential theory. The minor changes in pitch RAO for $0.2 < \omega < 1$ rad/s are mostly because of changes to the mass and stiffness matrix in *MATLAB* compared to the mass model in *HydroD*. With viscous effects calculated by Morison's equation and correct mass and stiffness matrix, the results are similar to those presented by Roddier, Peiffer, et al. (2011), who include viscous damping effects into *WAMIT* by a matrix. The surge RAO increases for low frequencies since no mooring restoring matrix is added. It is also seen that the heave RAO is no longer zero for a frequency around 0.35 rad/s when Morison's equation is added to the potential theory solution since the drag and inertia forces are nonzero even though the potential excitation force is canceled out in heave direction. This effect is explained in Appendix C. The heave RAO calculated with *MATLAB* is lower for frequencies below the natural frequency since the heave restoring coefficient calculated is larger than in *Wadam*. However, the heave RAO goes towards one for low frequencies, meaning the structure moves with the wave amplitude as expected. Due to the interpolation, a large pitch amplitude is calculated at the pitch natural frequency. Both potential and viscous damping are low at such a low frequency, however, this is outside of the wave energy range. Overall, the results show good resemblance in the wave energy range, and the method could be assumed to be correct.

4.7.3 Verification of Internal Hull Loads Calculations

The post-processing of the *Wadam* result files and the calculation of the internal loads in the cross-section were verified in three ways. First, to verify that the integration of the pressure on the panels was correct, the model was restrained from moving, resulting in that the pressure loads on the structure should be equal to the potential excitation loads, as can be seen in Figure 4.8a. Secondly, the calculation of the restoring and inertia loads was verified by creating a simple mass model in *GeniE*, where the thickness of the columns was increased until the

correct mass displacement was achieved. Sectional loads were calculated in *Wadam* by defining a cross-section in the yz-plane at $x = 0$. The sectional pressure loads calculated by *Wadam* include changes in hydrostatic pressure (DNV GL AS, 2019d). As seen in Figure 4.8b, the pressure plus restoring loads in the cross-section calculated manually and pressure loads given by *Wadam* show good resemblance. The difference in the bending moment comes from different mass center definitions. The small difference in the x-force is unknown and should not be there, as no restoring is defined in surge direction and the integration method shows good results for the other methods. Figure 4.8b also shows the inertia loads and sectional loads calculated manually and by *Wadam*, which show similar trends, but are not equal since the mass distribution is not equal. However, it shows that the calculated inertia and sectional loads are defined correctly. Thirdly, Figure 4.8c shows that the pressure loads plus the radiation loads give the potential excitation loads ($\boldsymbol{F}_p + \boldsymbol{A}\ddot{\boldsymbol{\eta}} + \boldsymbol{B}\dot{\boldsymbol{\eta}} = \boldsymbol{F}_{excitation}$) and, therefore, that the pressure loads are correctly calculated. It also shows how the radiation loads differ when using the RAOs calculated by *Wadam* with and without extra damping, and when using the RAOs calculated when Morison's equation is included. The main difference is found in the z-direction, where viscous damping is important around resonance. The radiation force when extra damping is included has a smaller peak at heave resonance than without extra damping, giving overall better results.
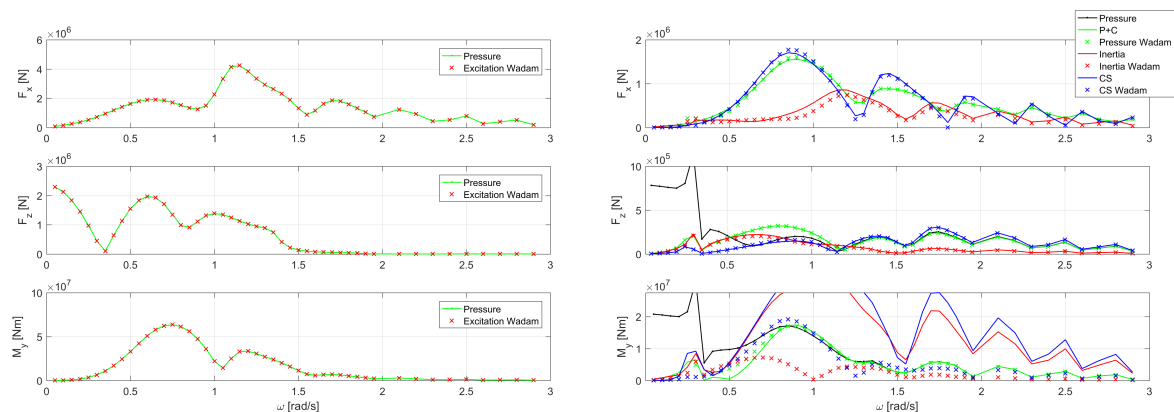
(a) Restrained model.

(b) Cross section.
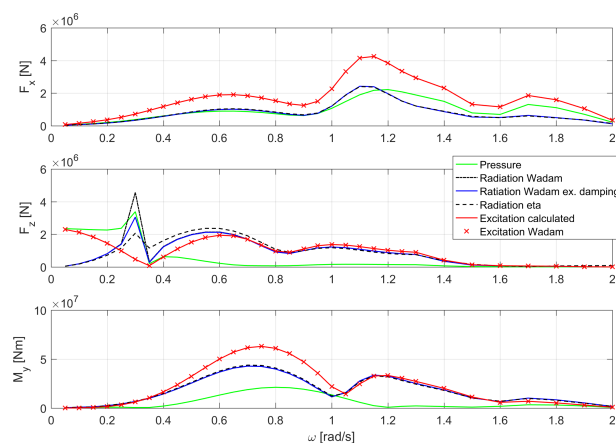
(c) General.

Figure 4.8: Verification of procedure for calculating internal loads. The pressure loads are calculated with *MATLAB*. In (a) and (c), the pressure loads are calculated for the entire body, while in (b) the pressure loads are calculated from the panels at $x > 0$. In (b), $P + C$ are the pressure plus restoring loads and CS is the cross-section. In (c), the radiation loads are calculated with the RAOs from *Wadam* with and without extra damping, and using the RAOs calculated manually (eta).

5 Results and Discussion

This section presents and discusses the results found during the thesis work. Section 5.1 presents an initial upscaled 10 MW platform and discusses general findings concerning the design. In Section 5.2, the effects of parameter variation on the behavior of the platform are examined and discussed. An improved design is then proposed in Section 5.3, based on the findings in Section 5.2. Finally, the effect of a mean tilt angle is discussed in Section 5.4.

5.1 Upscaled Design

5.1.1 Mass and Hydrostatic Properties

Using a scaling factor based on the difference in mass of the wind turbines, as explained in Section 2.4, a preliminary design of the 10 MW WindFloat structure is obtained based on the 5 MW WindFloat defined by Roddier, Peiffer, et al. (2011). The upscaled main dimensions are given in Table 5.1 and are based on the scaling factor,

$$k = \sqrt[3]{\frac{M_{WT,upscaled}}{M_{WT,initial}}} = \sqrt[3]{\frac{1.57E06}{6.97E05}} = 1.31. \tag{5.1}$$

Table 5.1: Main dimensions of the upscaled 10 MW WindFloat structure.

Parameter	Value [m]
Column diameter	13.4
Length of heave plate edge	19.7
Column center to center	60.3
Main beam and pontoon diameter	2.8
Bracing diameter	2.0
Operating draft	22.3
Freeboard	10.0

The diameter of the columns was increased more than the scale factor to meet the criterion for the maximum static pitch angle, $k = 1.34$. An error in the control of the minimum pitch restoring coefficient, that calculated the inclining moment with an arm equal to the hub height plus the freeboard, instead of using just the hub height, was found after some of the analyses were conducted. It was decided to continue with a column diameter of 13.4 meters as the baseline 10 MW upscaled design, since it was not hydrodynamically optimized design anyway, even though a diameter of 13.1 meters would be sufficient.

For comparison, the formulas given by Leimeister (2016) give a scaling factor for the column diameter of 1.29, when the center column is neglected. A column diameter of 12.9 meters results in a maximum static pitch angle of 9.6 degrees when the ballast is filled from the bottom of the columns. For the initial 5 MW WindFloat, the maximum static pitch angle is 14.7 degrees. It is seen that the same static pitch angle is not obtained. This inconsistency is due to the different geometries of the DeepCwind and the WindFloat concept. In the development of the column diameter scaling factor, Leimeister (2016) neglects the change in volume displacement of the columns, which for the upscaled design is 86 % of the total displacement.

The main design criteria for the upscaled design are listed in Table 5.2. The total mass of the structure increases by 1.328^3 compared to the 5 MW structure due to the larger column

diameter. The heave natural period has increased compared to the 5 MW WindFloat hull as the mass increases by a higher factor than the restoring coefficient. The roll and pitch natural frequencies have decreased, and are still outside the wave energy range. Column one contains 19 % of the total ballast.

Table 5.2: Main design criteria for the upscaled 10 MW design.

Design criterion	Value
Steel mass [kg]	2.24E+06
Volume displacement, ∇ [m^3]	1.09E+04
Total mass [kg]	1.12E+07
Static pitch angle [deg]	8.00
Heave natural period [sec]	22.0
Roll natural period [sec]	39.8
Pitch natural period [sec]	39.8

5.1.2   Hydrodynamic Results

When the structure is upscaled, keeping the same mesh density of 1 meter as tested for the 5 MW platform results in more elements, and longer computational time. Therefore, the upscaled structure was analyzed in *Wadam* with a mesh density of both 1 meter and 2 meters. This gave negligible changes in the coefficients, with the largest difference in the heave added mass of less than 0.5 %. For the analyses presented for the rest of the thesis, a mesh size of 1.4 meters is used on the columns for a better transition to the small elements at the heave plate edges. In the center under the heave plates a mesh size of 2.2 meters is specified, which is still under 1/6 of the shortest wavelength analyzed.

The potential excitation loads calculated by *Wadam* and the wave loads calculated with Morison's equation are given in Figure 5.1. It is seen that the potential excitation loads are of one order of magnitude larger than the loads on the slender elements, except in heave at a frequency around 0.3 rad/s. In general, the inertia loads from Morison's equation are more important than the drag loads. This is because a one-meter wave amplitude is used in the calculations. From Faltinsen (1990), viscous loads are most important when the wave height/diameter ratio is above ≈ 10 for a cylinder standing on the seafloor. This is not the case here but indicates that since the wave amplitude is low, viscous loads will be of lower importance than inertia loads. An exception is at the heave natural frequency, where the heave motion of the platform is large, which increases the linearization term. Also, the heave plates increase the drag loads in heave and pitch direction.

(a) Potential excitation loads.

(b) Morison wave loads.
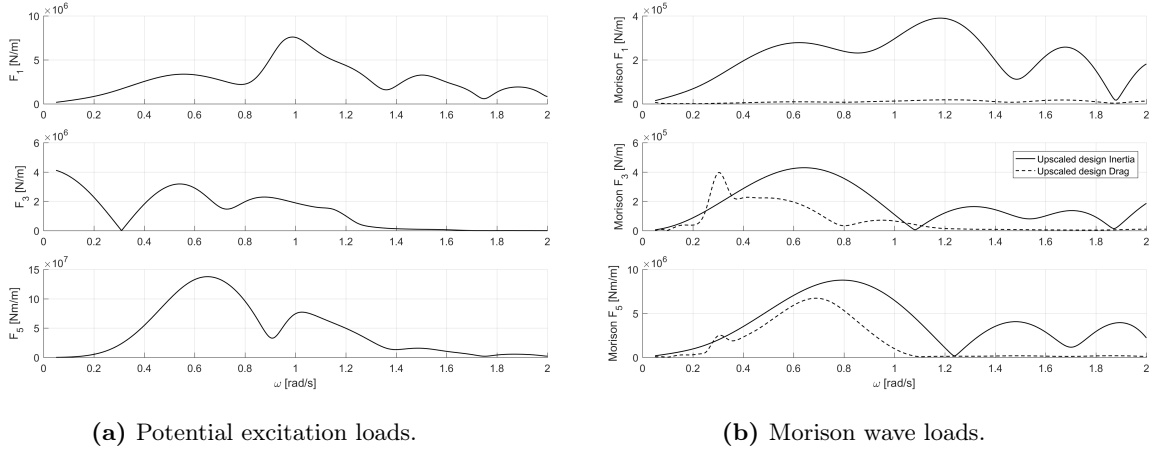
Figure 5.1: Potential excitation loads and wave loads from Morison's equation on the upscaled design.

The heave excitation force is zero at the frequency 0.31 rad/s because of counteracting forces on the bottom and top side of each heave plate. This is called the heave cancellation frequency and is derived in Appendix C. As long as the mooring stiffness is negligible in heave, the heave cancellation frequency is always at a frequency higher than the heave natural frequency. In Appendix C, the heave excitation force is estimated and given by equation (C.11). The estimated force is compared to the heave force from *Wadam* in Figure 5.2. The force amplitudes are almost equal for low frequencies, as long waves are assumed in the estimation. The estimated phase is also equal up to around 1 rad/s. At higher frequencies, the long-wave approximation is no longer valid. For instance, constant pressure cannot be assumed over the length of the heave plates. The second drop in the heave force, at 0.73 rad/s, is because of the phase difference between the columns and is close to a wavelength twice of the distance in the x-direction between the columns. The drop comes from the last term in equation (C.11) is at its minimum value. The heave force is not canceled since the hull is not symmetric about the y-axis. Around this frequency gives the maximum pitch moment, as expected. The pitch moment is a result of the combination of surge and heave forces on the different columns and heave plates.
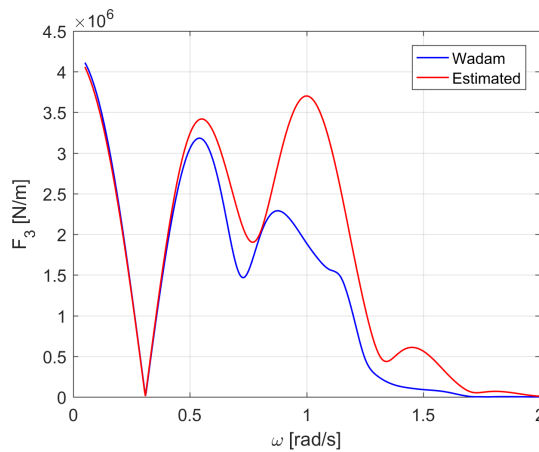
Figure 5.2: Comparison of the heave excitation force amplitudes calculated by *Wadam* against the estimated heave force derived in Appendix C.

The surge excitation force is mainly due to the pressure on the columns. In Section 5.2.1, the surge excitation force from *Wadam* is compared against using the inertia term from Morison's

equation. Similar force amplitudes and phases were obtained up to around 1 rad/s. Over this frequency, the long-wave approximation is not valid on the columns.

The hydrodynamic added mass and potential damping coefficients from *Wadam* are shown in Figure A.1 and Figure A.2, and the diagonal terms are given in Figure 5.3. It is seen that due to the rotational symmetry $A_{11} = A_{22}$, $A_{44} = A_{55}$, $B_{11} = B_{22}$, and $B_{44} = B_{55}$. Further, since there is no forward speed and due to the symmetry, $A_{15} = A_{51} = -A_{24} = -A_{42}$, and $B_{15} = B_{51} = -B_{24} = -B_{42}$. The other coupled terms are much lower, but will have similar properties as the surge/pitch and sway/roll coupling terms.

At the natural periods of the structure, the damping ratios are under 0.1. Therefore, the undamped natural periods are assumed to be equal to the damped natural periods. Anyways, the damped natural period is always larger than the undamped, so using the undamped for estimating heave natural period will, if there is any difference, be a conservative estimate. The damping coefficients go to zero when frequency goes to zero or infinity, as the structure cannot generate waves at these frequencies. In long waves, the platform follows the waves, viscous damping is then important.

(a) Added mass.
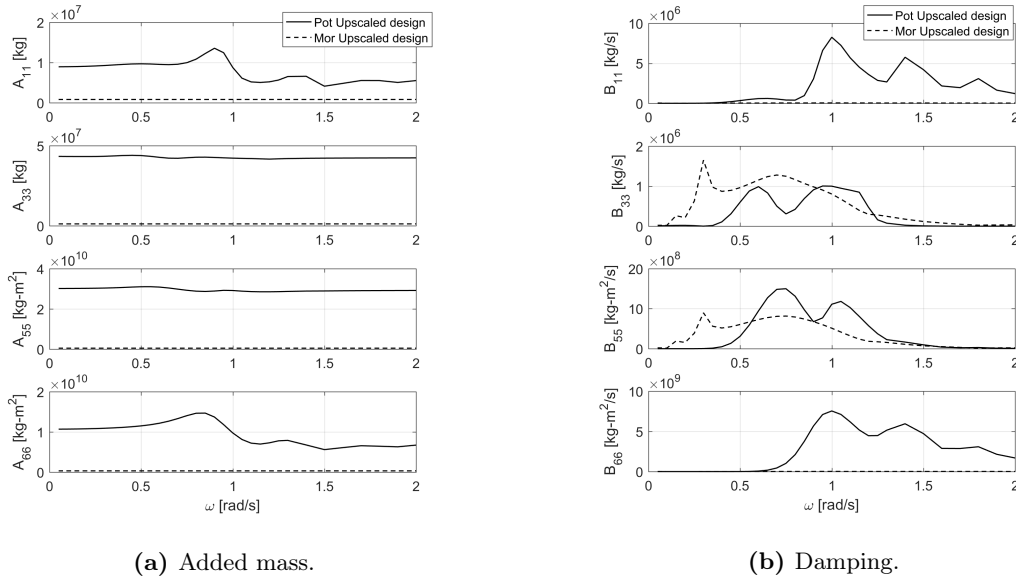
(b) Damping.

Figure 5.3: The diagonal added mass and damping terms from *Wadam* and Morison's equation for the upscaled design. From Morison's equation, the added mass terms are from the slender elements, while the damping terms are from the slender elements and the heave plates.

Figure 5.3 shows that the added masses from the slender elements not included in the *Wadam* analysis are very low. The estimated heave added mass was $4.33E + 07$ kg, while the one calculated with *Wadam* and Morison is $4.45E + 07$ kg at the heave natural frequency, showing good agreement. From the estimation, the added mass from the heave plates is 98 % of the total estimated value, yielding that the heave plates are the main contributor to the heave added mass for the structure. It should also be noted that the heave added mass is almost four times larger than the total mass of the structure.

The linearized quadratic viscous damping is important in heave and pitch because of the heave plates and especially at low frequencies. At the heave natural frequency, the potential damping is almost zero which would have resulted in a large heave motion amplitude at this frequency if viscous damping was not included, as found in Figure 4.7.

The amplitudes of the terms connected to the drag loads in Morison's equation, being the damping coefficients and drag loads, are greatly influenced by the motions being calculated at discrete frequencies, and especially around the heave and pitch natural frequencies. This is because of the linearization term. If the discrete frequencies are not close to the natural frequencies, the motions and the viscous loads will be relatively lower. The results are interpolated between the calculated frequencies, so the effect of large motion amplitudes at the heave and pitch natural frequencies will not necessarily be accounted for when calculating the linearized damping or drag loads from Morison's equation. Therefore, the maxima values of the heave and pitch damping coefficients, drag loads, and RAOs could be a bit arbitrary around the heave and pitch natural frequencies. For instance, the pitch RAO maximum seen in Figure 4.7 would be lower in reality since viscous damping would increase when the motions increase.

The terms calculated with Morison's equation should have been calculated for more frequencies than used in *Wadam* to get more accurate results around the heave and pitch natural frequencies, however, this is not done in the thesis as the problem was realized after most of the analyzes were completed. Anyways, this only affects the heave and pitch RAOs, and internal load RAOs at the natural frequencies which are designed to be outside the wave energy range between 5-20 seconds or 0.3-1.4 rad/s.

The resulting motion RAOs for the upscaled design are not given in this section as they are given in Section 5.2 as the baseline design and compared against the RAOs found when the parameters are adjusted. It was found that the pitch motion is strongly coupled to surge motion at some frequencies. It is observed the surge/pitch added mass and damping coefficients are larger than the other coupled terms. The one DOF solution gives results for surge and heave RAOs close to the six DOF solution, meaning these motions are not as affected by the coupling terms. The pitch RAO calculated with the one DOF and six DOF equations of motions are given in Figure A.3 and shows that at frequencies above the natural frequency the coupling is important. Around 0.2 rad/s, the pitch motion is almost canceled due to coupling effects with surge.

5.1.3   Internal Hull Loads for the Upscaled Design

The external and inertia loads acting on column one, together with the cross-sectional loads they are in equilibrium with, are plotted for different wave frequencies in Figure 5.4. The different load components are explained in Section 4.2.4
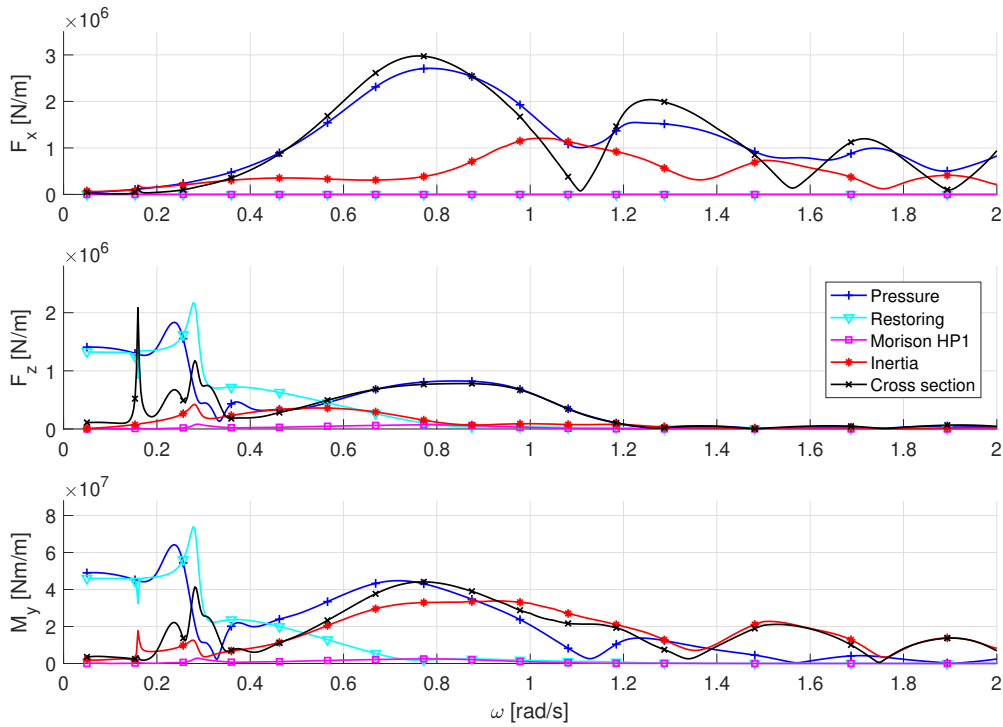
Figure 5.4: Sectional forces and moment amplitudes for different wave frequencies calculated in the yz-plane with moments about the origin for the upscaled design.

At low frequencies, the restoring loads are the most important for counteracting the external pressure, while the inertia loads are the most important at higher frequencies as expected since they are $\propto \omega^2$. It is observed that the sectional forces in the x-direction are larger than in z-direction in the wave energy range. The restoring forces from the mooring system are not included in the sectional load calculations, therefore, there are no restoring force in the x-direction. It is also seen that the viscous loads on the heave plate are low compared to the other components.

For the upscaled design, the distance in the x-direction between the centers of the columns, L_x, is 52.2 meters. As seen in Table 5.3, the cancellation effects of the cross-sectional force in the x-direction at higher frequencies come from the cancellation effects of waves with one, two or three wavelengths between the columns. The wave frequency for the maximum force amplitude in x-direction and bending moment corresponds to a wavelength twice of L_x. This is the maximum split force, as illustrated in Figure 4.3. These maxima are also at a typical wave frequency.

The cross-sectional force in z-direction has a maximum at a frequency higher than the x-force. It also has maxima at the heave and at the pitch natural frequencies mostly due to differences between the pressure force and the restoring force. A drop in the restoring loads at the pitch natural frequency causes the peak in the cross-sectional force in z-direction. The drop comes from a sudden increase in the pitch motion RAO, which as mentioned, is a bit arbitrary due to the motions being calculated at discrete frequencies and since the damping is low. At the pitch natural frequency, the pitch and heave motions are in phase with the wave surface. This means the positive pitch motion counteracts the positive heave motion of the column, resulting in lower restoring loads on the column. For the bending moment, the inertia moment increases at pitch resonance canceling the effect of the drop in the restoring force. At the heave natural

frequency, the restoring loads increase since the heave motion amplitude is large, while the pitch motion is lower and out-of-phase with heave. The pressure loads are low, giving large loads in the cross-section, even though the inertia loads increase. However, the load maxima at the heave and pitch natural frequencies are not too interesting since wave excitation loads at these frequencies are rare, especially at the pitch natural frequency.

Table 5.3: Frequencies of interest for the internal load calculations. $L_x = 52.2$ meters and is the distance between the center of the columns in x-direction.

ω [rad/s]	λ [m]	Relation
0.76	107	$\lambda = 2L_x$
1.10	51	$\lambda = L_x$
1.55	26	$\lambda = \frac{1}{2}L_x$
1.90	17	$\lambda = \frac{1}{3}L_x$

5.2   Effects of Parameter Variation on Platform Behavior

A parametric study of four main dimensions: 1) the column diameters, 2) the draft, 3) the distance between the columns, and 4) the heave plate size is carried out in this section. The parameters are chosen based on the discussion in Section 4.6.1. The changes affect both the mass and hydrostatic properties of the structure and the radiation and diffraction loads on the structure. The upscaled 10 MW structure, presented in Section 5.1, is used as a baseline design, and the different parameters are increased and decreased individually, in order to observe the influence of each parameter on the system. Only the amount of ballast in each column has also been changed to keep the center of gravity above the center of buoyancy and to achieve equilibrium between gravitational and buoyancy loads.

The results are presented and discussed individually in separate sections for each parameter. In Section 5.2.5, the effects of the different parameters are compared by studying the relative changes in the design criteria and the relative changes in the motions, nacelle accelerations, and internal loads standard deviations in the given sea states. More detailed figures used for the discussion are given in Appendix B.

5.2.1   Column Diameter

For the baseline design, the column diameter was upscaled more than the rest of the parameters to give a sufficient pitch restoring coefficient due to an error. When analyzing the effect of the column diameter, the diameter has been adjusted to its minimum and maximum values within the given design criteria. The structure has been analyzed with column diameters of 12.8, 13.4 (baseline design), 14, and 15 meters. The effects on the static results are shown in Figure 5.5.
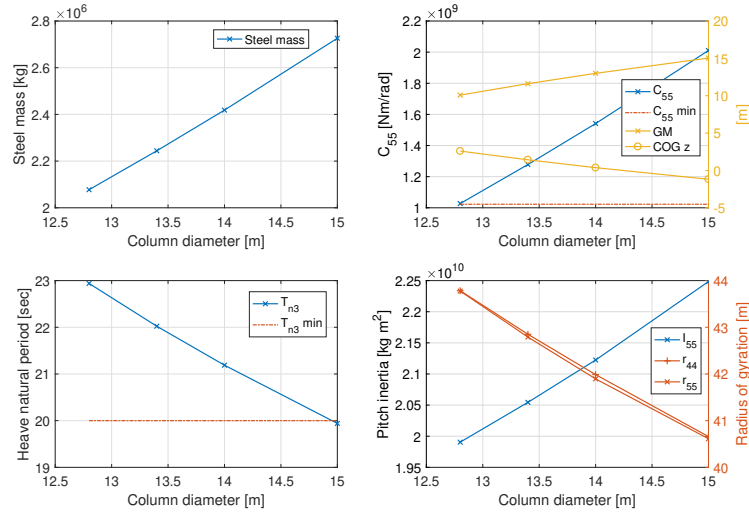
Figure 5.5: Effect of column diameter on steel mass, pitch restoring coefficient, heave natural period, and pitch inertia. The metacentric height and global z-coordinate of the center of gravity are given at the right axis of the upper right plot. The roll and pitch radii of gyration are given at the right axis of the lower right plot.

A lower limit for the column diameter exists to keep the static pitch angle below 10 degrees, and an upper limit for keeping the heave natural period above 20 seconds. This is one of the main problems of semi-submersible designs, to have enough stiffness in pitch without getting too much stiffness in heave.

An increase of the column diameter by a factor k increases the column displacement by k^2. Since the displaced volume of the structure is mainly from the columns, the total displacement and the steel mass of the structure will almost increase by k^2. C_{55} increases by a factor close to k^4 when the diameter increases by k. The metacentric height, see equation (3.24), increases because the waterplane area is increased and the larger column diameter allows more ballast to be located lower in the hull, lowering the center of gravity.

An increased column diameter gives higher platform mass and heave restoring coefficient, both increasing by approximately k^2. The heave added mass decreases due to less effective area on the top side of the heave plates, resulting in a decreasing heave natural period.

The pitch inertia increases with larger column diameters, even though, the radius of gyration decreases because the mass increases by a higher factor. The radii of gyration decrease since more mass is placed closer to the origin.

The added mass and potential damping diagonal coefficients obtained from Wadam for the different column diameters are shown in Figure 5.6.
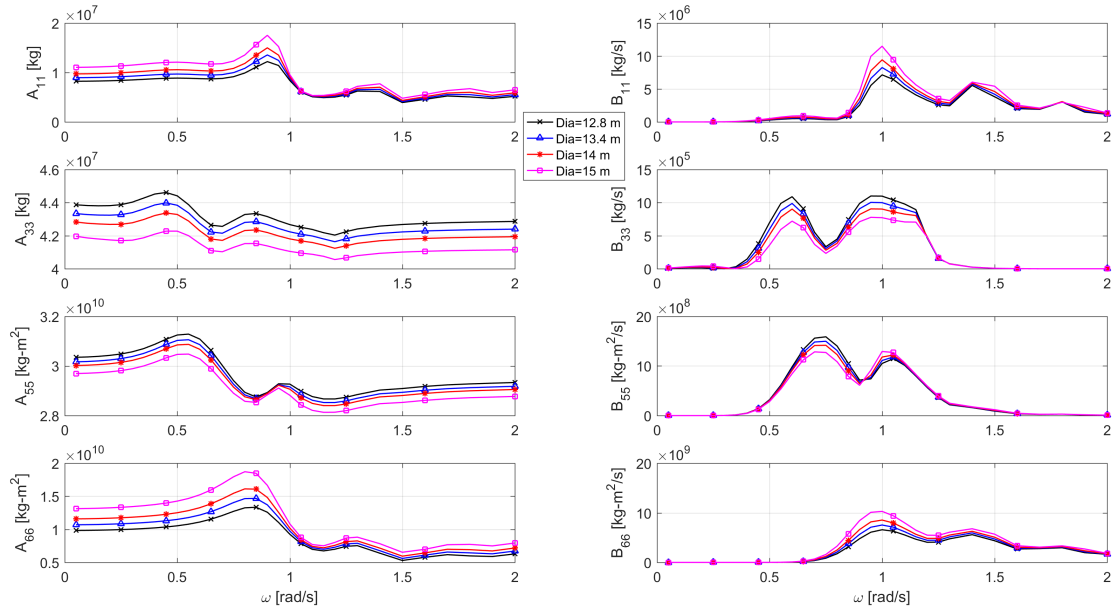
Figure 5.6: Added mass and potential damping coefficients in surge, heave, pitch, and yaw for different column diameters.

A_{11} and A_{66} increase linearly with the displacement of the structure for low wave frequencies, as can be seen in Figure B.1, where the coefficients have been normalized with respect to the column diameter. A linear increase with the displacement signifies that A_{11} and A_{66} increase by almost k^2 when the diameter increases by a factor k. The columns could be assumed slender in long waves and strip theory could be used to calculate A_{11}. Assuming a constant added mass coefficient, the added mass will increase linearly with the volume of the columns. As seen from Figure B.1 for long waves, the added mass coefficient in surge is almost 1, which corresponds well with the added mass coefficient for a circular two-dimensional body oscillating in infinite fluid (DNV GL AS, 2019a).

A_{33} and A_{55} decrease with increasing column diameter. The heave added mass comes from the heave plates. With increasing column diameter, the effective area on the top side of the heave plates decreases, giving a lower A_{33}. This effect is seen from the theoretical estimated added mass of the heave plates, equation (2.5), which gives a good estimate. A_{33} decreases by a factor lower than $\sqrt{k}$, as can be seen in Figure B.1. A_{55} decreases less than A_{33} since it also depends on A_{11}.

The potential damping terms in Figure 5.6 show the same trends as the added mass. However, it is difficult to estimate the changes in the terms since they are more frequency-dependent. In heave and pitch, the potential damping decreases with increasing column diameter. Less free surface waves are generated when the effective area of the heave plate top side decreases.

The first-order wave excitation loads in surge, heave, and pitch from the potential flow solution in *Wadam* are given for different column diameters in Figure 5.7.
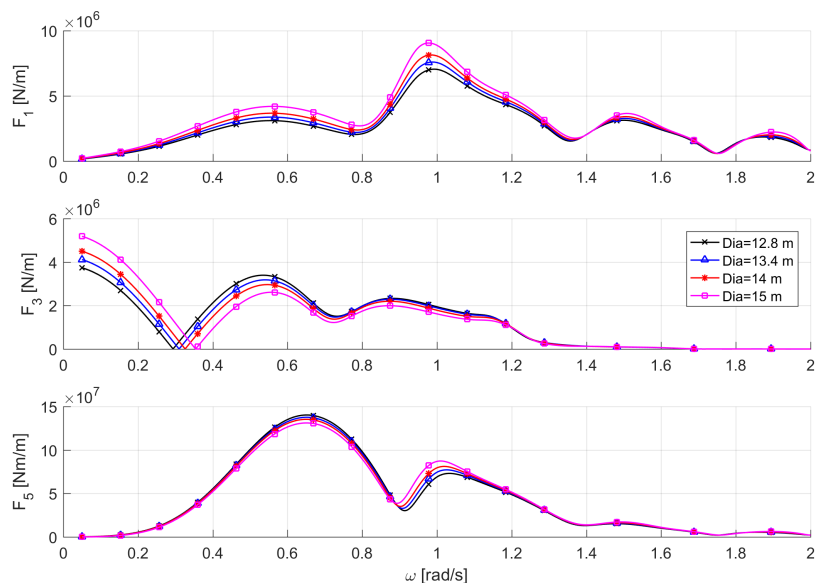
Figure 5.7: First-order wave excitation load amplitudes per unit wave amplitude in surge, heave, and pitch for different column diameters.

At low frequencies, the surge excitation force increases linearly with the increased volume of the structure and, therefore, almost by a factor k^2. This could be seen in Figure B.2, where the excitation loads are normalized with respect to the column diameter. The surge force mainly comes from the forces on the columns. By using the long-wave approximation, the Froude-Kriloff and diffraction force increase linearly with the volume, as for the surge added mass. This could be seen by using the first inertia term of Morison's equation, (3.25), which is based on potential theory. The surge inertia force on the columns is calculated using Morison's equation with an added mass coefficient of one and is compared to the surge excitation force from *Wadam* in Figure 5.8.
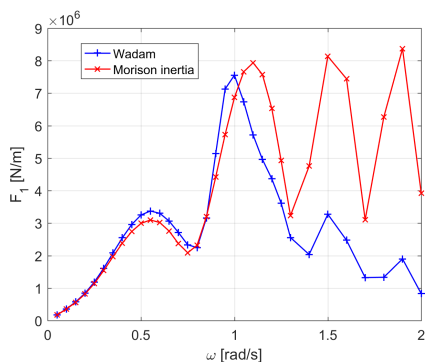
Figure 5.8: The surge wave excitation force amplitudes calculated by *Wadam* is compared with the inertia force on the columns using Morison's equation for a column diameter of 13.4 meters. $C_a = 1.0$ is used for the columns in Morison's equation.

The forces are similar for wave frequencies up to approximately 0.9 rad/s, corresponding to a wavelength of 76 meters, which is more than five times the column diameter. It is also seen that the surge added mass and potential excitation force increase linearly with the displacement up to this frequency, for higher frequencies the long-wave approximation is not valid.

The cancellation frequency of the heave excitation force shifts to a higher wave frequency for a larger column diameter, since the heave natural frequency increases. This could be seen from the equation for the heave cancellation frequency, equation (C.13). The excitation force in heave is mainly decided by the difference in pressure on the top and bottom sides of the heave plates. At frequencies lower than the cancellation frequency, the heave excitation force increases with increasing column diameter since the difference in the area on the top and bottom side of the heave plates increases. In the wave energy range, the heave excitation force in general decreases with large column diameter because of the larger difference in the heave plate area on the top and bottom side and lower heave added mass. The heave force is estimated, see Appendix C, as

$$F_{exc,3} = \zeta_a e^{kz_m}[\rho g A_{col} - \rho \omega^2 z_m A_{col} - \omega^2 \frac{1}{3}(M + A_{33})](2e^{i(\omega t - kx_{col2})} + e^{i(\omega t - kx_{col1})}). \quad (5.2)$$

As seen from the equation, these effects reduce the absolute value of the expression in the brackets for frequencies over the cancellation frequency. The second drop in the heave force is around 0.76 rad/s for all columns, which is when the expression in the last parenthesis has its minimum amplitude, as the distance between the columns is equal. Around $\omega = 0.5$ rad/s, the heave excitation force decreases by k^2.

The pitch excitation moment does not show a consistent trend with changing the column diameter since the surge force increases with the diameter and the heave force decreases in the wave energy range. Around the peak frequencies of the environmental conditions (0.6-0.8 rad/s), the pitch moment decreases with increasing column diameter since the heave force decreases. The moment arm for the heave force makes it the most important component. At higher frequencies, the surge force is more important since the wave pressure at the heave plates is low. Therefore, the pitch moment increases at higher frequencies.

The wave loads from Morison's equation are given in Figure B.3 and the Morison added mass and linearized viscous damping are given in Figure B.4. There are negligible changes in the inertia terms, as the pontoons and bracing have almost the same lengths. The drag related terms increase with increasing column diameter around heave natural frequency. This is probably, as explained in Section 5.1, because of the change in heave natural frequency that influences the heave RAO at the calculated frequencies.

The resulting RAOs for surge, heave, and pitch motions for different column diameters are given in Figure 5.9.
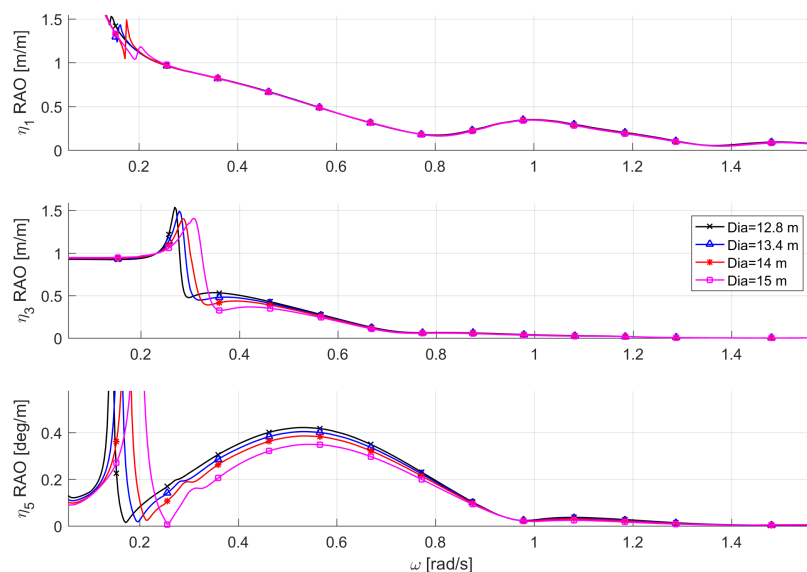
Figure 5.9: Surge, heave, and pitch RAOs for different column diameters.

The column diameter shows a small overall effect on the surge RAO, since the surge excitation force, platform mass, and added mass all increase by the same factor for low frequencies. For higher frequencies, the changes in surge excitation forces are small.

For the heave and pitch RAO, the motions are reduced with increasing column diameter in the wave energy range. The excitation loads in this range are reduced, and the structure mass, inertia, and restoring increase with higher diameter. The total mass/inertia plus added mass/inertia in heave and pitch increase with a larger column diameter since the structure mass and pitch inertia increase by a higher factor than A_{33} and A_{55} decrease. A larger column diameter shifts the heave and pitch natural frequencies closer to the wave energy range.

The forces and bending moment in the cross-section for different column diameters are shown in Figure 5.10.
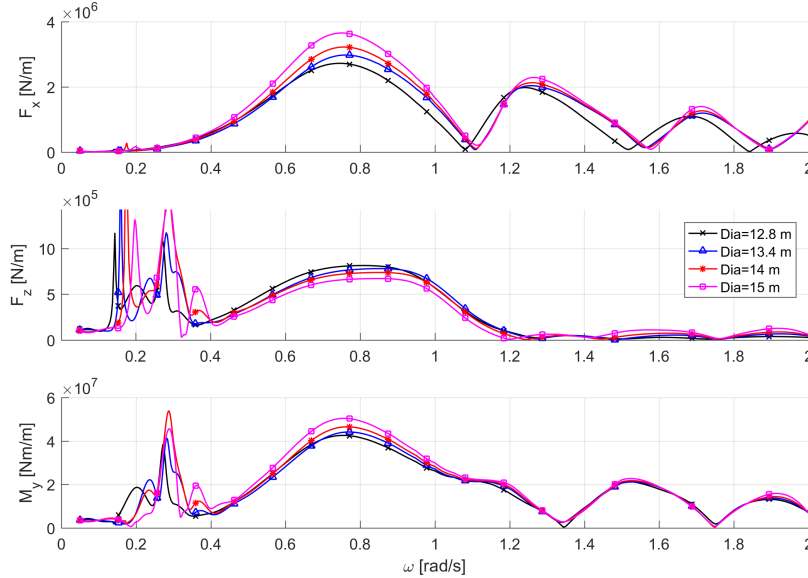
Figure 5.10: Sectional force and moment amplitudes for different column diameters.

The cross-sectional force in x-direction increases proportionally with the displacement of the structure for wave frequencies up to $\omega = 0.9$ rad/s, in the same way as the surge excitation force. In Figure B.5, the cross-sectional forces and bending moment are divided by the buoyancy force.

The cancellation frequencies of the force in x-direction for the smallest column are shifted to lower frequencies, which could be because the distance between the column surfaces is increased. However, the different cancellation frequencies for the smallest structure should not be so distinct from the others and are probably also because of the spline interpolation of the pressure forces acting on the column. Only a small difference at the calculated frequencies could result in the spline line is different.

In the wave energy range, the cross-section force in z-direction decreases because of lower pressure force, in the same manner as seen for the heave excitation force. At heave resonance, the force in z-direction increases with the diameter because of larger pressure and restoring forces.

The cross-section bending moment increases with increasing column diameter, because of increased pressure moment on column 1 that comes from increased pressure forces in x-direction. The sectional bending moment increases with a factor lower than the displacement since the pressure force in z-direction decreases with increasing column diameter. A comparison of the different loads acting on the cross-section for the smallest and largest column diameters is given in Figure B.6. It is seen that for frequencies lower than the cancellation frequency, the pressure force in z and the pressure bending moment increase with increasing diameter, and that these are counteracted by increased restoring loads. It is also seen that the inertia moment about the y-axis decreases with a larger diameter as the motions are reduced.

5.2.2   Draft

The baseline design draft is 22.3 meters, the effect of increasing the draft to 24 meters and decreasing it to 18, 16, and 14 meters is investigated. The effects of changing the draft on the hydrostatic properties are shown in Figure 5.11.
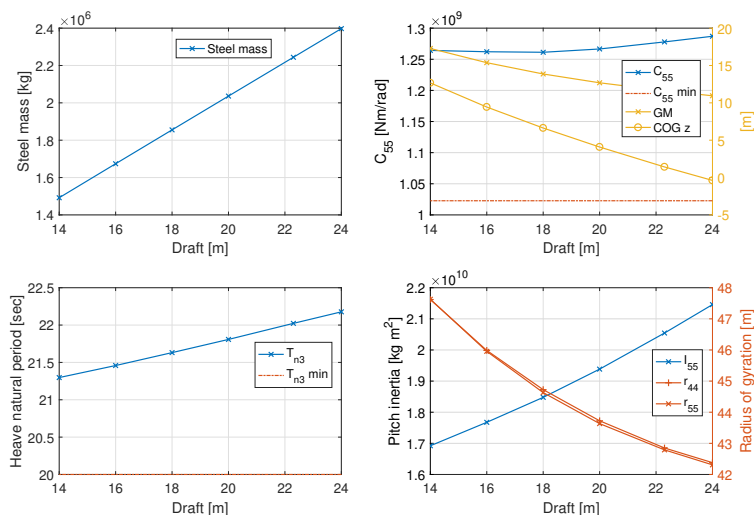
Figure 5.11: Effect of changing draft on steel mass, pitch restoring coefficient, heave natural period, and pitch inertia. The metacentric height and global z-coordinate of the center of gravity are given at the right axis of the upper right plot. The roll and pitch radii of gyration are given at the right axis of the lower right plot.

An increase of the draft by a factor k increases the column displacement by k and, therefore, the steel mass by almost the same factor. Changing the draft has little effect on C_{55}. The metacentric height decreases with an increasing draft since the waterplane area is unchanged while the displacement increases and both the center of buoyancy and gravity decrease with a larger draft. The increase in volume displacement is larger than the decrease in metacentric height, giving overall a small positive relationship between the increasing draft and C_{55}. The heave natural period increases with the draft since the mass of the structure increases. The mass increases more than the pitch radius of gyration decreases, resulting in larger pitch inertia for larger drafts. For the different drafts, the requirements to C_{55} and heave natural period are met. However, at draft 14 meters, only 10 % of the ballast was allocated in column 1, giving less room for active ballast to keep the platform upright in operation.

The added mass and potential damping diagonal coefficients obtained from Wadam for the different drafts are shown in Figure 5.12.
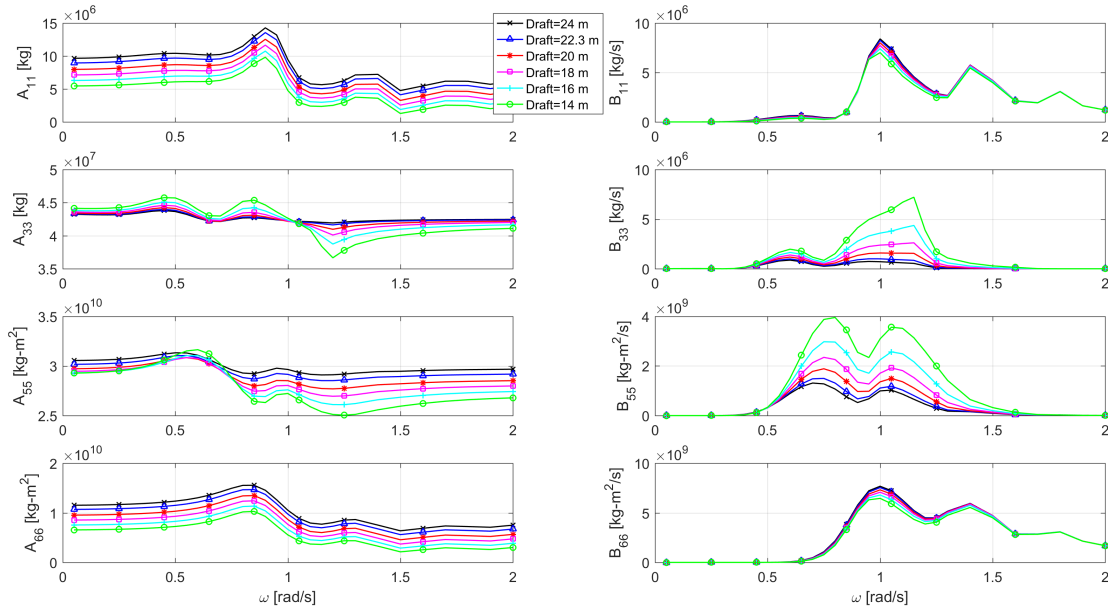
Figure 5.12: Added mass and potential damping coefficients in surge, heave, pitch, and yaw for different drafts.

A_{11} and A_{66} increase linearly with the draft or the submerged volume for low wave frequencies, similar to changing the column diameter. This could be seen in Figure B.7, where the coefficients are divided by the displaced mass of the structure. The potential damping in surge and yaw decrease with lower draft, but by a lower and more frequency dependent factor than the added mass coefficients.

A_{33} and A_{55} become more frequency dependent as draft decreases, since the heave plates get closer to the free surface. The heave plates have a side length of 19.7 meters, corresponding to a radius of 17.9 meters for an equivalent circular heave plate. For submergence-radius ratios over one, A_{33} is almost unaffected by changing draft. For lower ratios, A_{33} becomes more frequency dependent. A_{55} shows a larger frequency dependency than A_{33} at higher submergence ratios since the heave plates are not positioned in the origin of the coordinate system and experience larger vertical motions in pitch.

The heave and pitch potential damping goes to zero as draft goes to infinity, since the wave generation from the movement of the heave plates become zero. Therefore, at large drafts, the viscous damping becomes more important as it does for low wave frequencies. For lower drafts, the potential heave and pitch damping increase in the wave energy range since the heave plates are less submerged and generate more surface waves. The results for heave added mass and potential damping show similar trends as found by Antonutti et al. (2014).

The excitation loads in surge, heave, and pitch for different drafts are given in Figure 5.13.
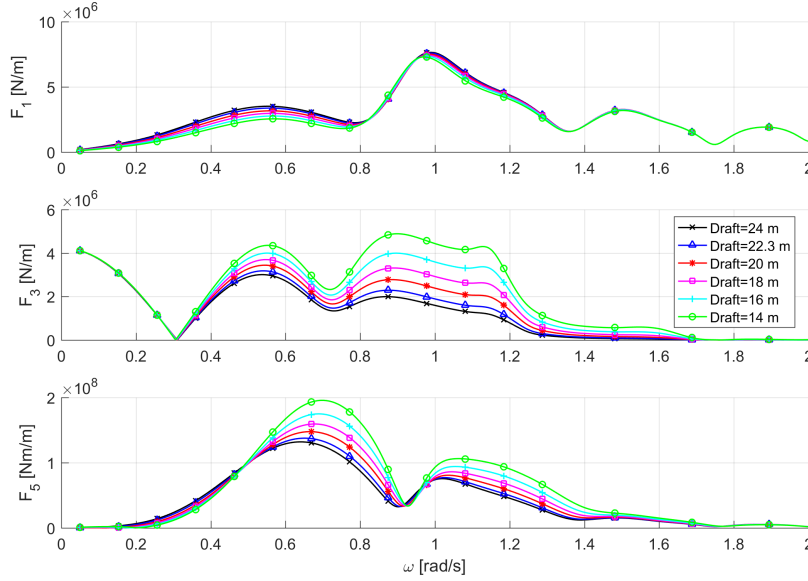
Figure 5.13: First-order wave excitation load amplitudes per unit wave amplitude in surge, heave, and pitch for different drafts.

The surge excitation force decreases with lower draft at low frequencies, due to lower volume displacement of the columns. The relation is not linear since the dynamic pressure loads are largest closest to the surface and decrease exponentially with the draft. Therefore, there are no differences in the surge force at high frequencies since the waves are small and dynamic pressure close to the draft is almost zero for all the drafts.

The heave cancellation frequency is equal for changing draft because the heave natural frequency decreases when the draft of the heave plates increases which results in the same cancellation frequency, see equation (C.13). This could also be understood by the ratio between the heave plate and column area is the same. Therefore, the frequency of canceling pressure forces between the top and lower sides of the heave plates should be the same, independent of the draft.

At lower wave frequencies than the cancellation frequency, the heave force is unchanged for different drafts since the wavelengths are much longer than the changes in the draft. For higher wave frequencies, the heave excitation force is more sensitive to changing draft since the wave number is higher, making the differences in the term e^{kz_m} larger. Therefore, the differences in the heave force between the different drafts increase up to a wave frequency of 1.2 rad/s, corresponding to $\lambda = 43$ meters. At higher frequencies, the dynamic pressure and wave-particle accelerations at the heave plates are low since the draft is then larger than half the wavelength. When the draft decreases by a factor k, the excitation force in heave increases with approximately k^2 for ω around 1 rad/s. The second drop in the heave force and maximum pitch force is still at a wavelength twice the length in x-direction between the columns. Lower draft gives higher pitch moment in the wave energy range, with an increase by around k for $\omega \approx 0.75$ rad/s and $\omega \approx 1.1$ rad/s. These trends can be seen in Figure B.8, where the excitation loads are normalized with respect to the draft.

The wave loads from Morison's equation are given in Figure B.9 and the Morison added mass and linearized viscous damping are given in Figure B.10. The inertia loads on the slender elements increase with lower draft since the wave-particle accelerations at the elements increase. The added mass from the slender elements decreases with lower draft in all modes since the

length of the bracing reduces. The linearized viscous damping in heave and pitch, and linearized drag loads increase with lower draft in the wave energy range, since the wave dynamics at the elements increase. Around the heave natural frequency, the viscous terms decrease with lower draft since the heave motion amplitudes at the closest calculated frequencies are influenced by the change of heave natural frequency.

The resulting RAOs for surge, heave, and pitch motion for different drafts are shown in Figure 5.14.
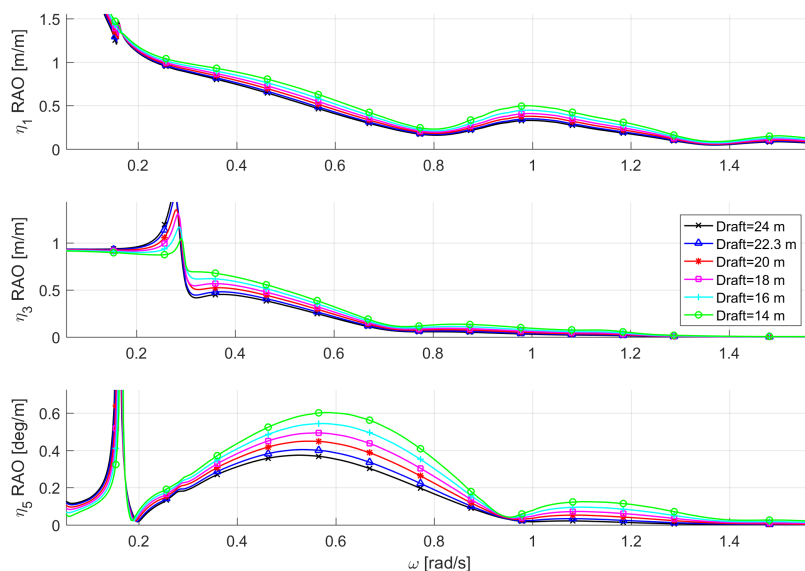
Figure 5.14: Surge, heave, and pitch RAOs for different drafts.

In general, reducing the draft increases the motion RAOs in surge, heave, and pitch in the wave energy range. The surge motion amplitudes because the mass and added mass in surge decrease by k, while the surge excitation force decreases by a lower factor.

In heave and pitch, the excitation loads increase with lower draft in the wave energy range, while the platform mass and inertia decrease, giving larger motion amplitudes. The restoring coefficients in heave and pitch are almost constant, resulting in similar behavior at low frequencies for different drafts. Higher surge and pitch motions, and especially at high frequencies will give high accelerations in the nacelle. This will become a problem with too low draft, as the pitch motion amplitude increases at typical wave frequencies around 0.75 rad/s. The peak of the heave RAO decreases with lower draft, even though the viscous damping is reduced because the potential excitation force lowers at heave resonance frequency since the natural frequency moves closer to the cancellation frequency for lower draft.

The forces and bending moment in the cross-section for different drafts are given in Figure 5.15.
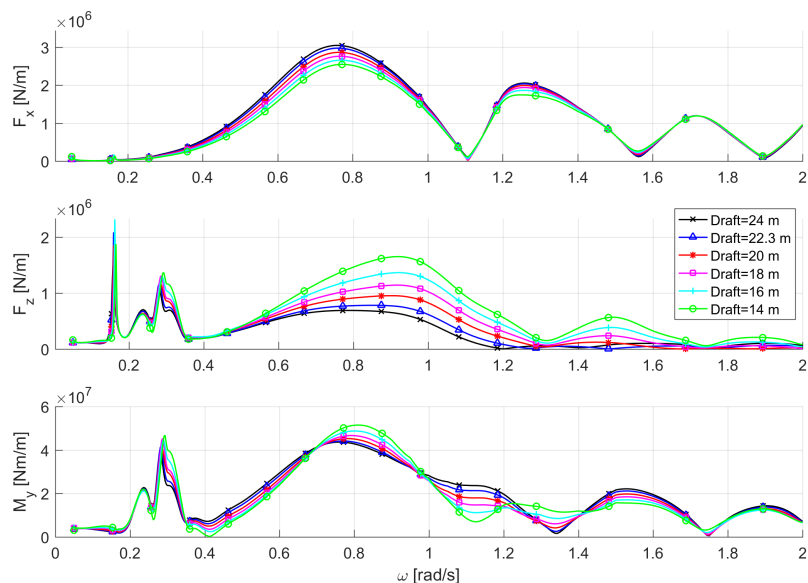
Figure 5.15: Sectional force and moment amplitudes for different drafts.

As for the column diameter, the force in x-direction decreases with lower draft, due to lower surge excitation force. The cancellation frequencies are the same since the distance between the columns is equal.

In the wave energy range, the force in z-direction and the bending moment maxima increase with lower draft due to higher excitation loads. The inertia moment amplitude increases with lower draft since the heave and pitch accelerations increase. This counteracts some of the increased pressure bending moment, as can be seen in Figure B.11, where the different load components calculated are plotted for draft 14 and 24 meters. Further, it is seen that the bending moment is not larger for all frequencies when the draft is reduced because of the large increase in inertia moment. At frequencies around 0.5 rad/s the bending moment is also reduced by a higher restoring moment from the increased motions. When the draft is 14 meters, the viscous loads on the heave plate are increased since the motions are larger, however, they are still low compared to the other components.

5.2.3   Distance between Columns

The distance between the center of the columns (DCC) is adjusted from the baseline design of 60.3 meters to 57, 63, 66, and 73 meters. The effects of changing DCC on the hydrostatic parameters are shown in Figure 5.16.
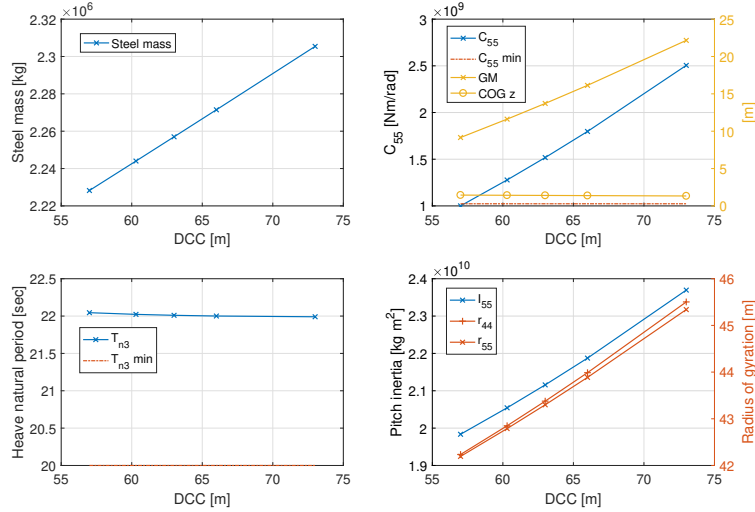
Figure 5.16: Effect of changing DCC on steel mass, pitch restoring coefficient, heave natural period, and pitch inertia. The metacentric height and global z-coordinate of the center of gravity are given at the right axis of the upper right plot. The roll and pitch radii of gyration are given at the right axis of the lower right plot.

Increasing DCC results in longer beams, bracing, and pontoons, which are only a small fraction of the total displacement. As discussed in Section 4.6.1, the diameters of the truss members are not changed. Therefore, the displacement and the steel mass are almost unaffected by changing DCC. DCC greatly influences C_{55}, since the second moment of the waterplane area depends on the distance to the columns squared. This increases the metacentric height of the structure and C_{55} by almost a factor of k^4 when DCC increases by k. The waterplane inertia increases by approximately k^2. However, since the displacement, center of buoyancy, and center of gravity are almost constant, C_{55} increases by a larger factor since the term $\rho g \nabla (z_B - z_G)$ is almost constant and always lower than zero, see equation (3.24).

For DCC equal to 57 meters, the requirement to the pitch restoring coefficient is not met. When DCC is too large, the structure gets a problem with the freeboard and the critical pitch angles. At DCC equal to 73 meters, the angle between the MSL, origin, and the bottom of the beams at column 1 was 9.06 degrees, which could lead to unwanted slamming loads when the platform is subjected to a wind overturning moment. For a DCC of this size, the freeboard should be increased, which would cause the steel mass to increase at the same rate as for increasing draft.

The heave natural period is unaffected, since the waterplane area, structural mass, and heave added mass are almost unchanged. The pitch inertia increases since the radius of gyration increases with a longer distance between the columns.

The added mass and potential damping diagonal coefficients obtained from *Wadam* for the different DCC are shown in Figure 5.17.
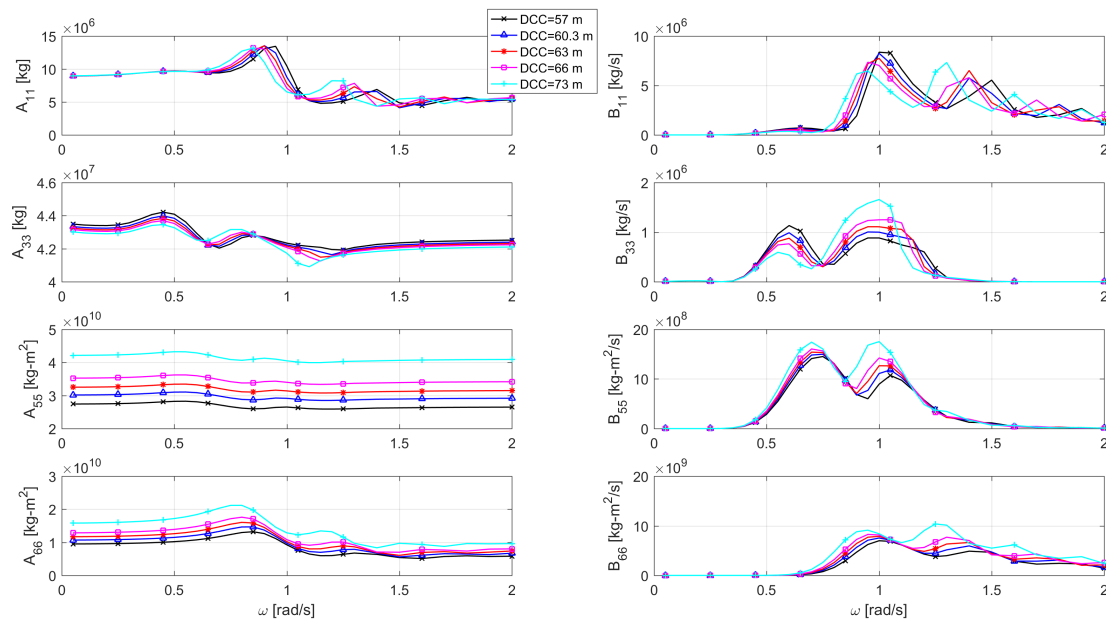
Figure 5.17: Added mass and potential damping coefficients in surge, heave, pitch, and yaw for different DCC.

A_{11} and A_{33} do not change much when changing DCC, since the dimensions of the columns and heave plates modeled are unchanged. However, there is less interaction between the columns when DCC increases. This affects A_{11} at higher frequencies and decreases A_{33} when DCC increases.

The added inertia A_{55} and A_{66} increase by $\approx k^2$ when DCC increases by k since the moment arms increase and the diagonal added mass terms depend on the arm squared (Faltinsen, 1990). A_{55} and A_{66} are plotted when divided by DCC squared in Figure B.12. A_{66} increases more than A_{55} with increasing DCC, since A_{33} decreases while A_{11} and A_{22} are less affected.

The damping terms show similar trends as the added mass terms, but it is difficult to see consistent trends as they are more frequency-dependent.

The wave excitation load RAOs from *Wadam* for surge, heave and pitch for different DCC are given in Figure 5.18.
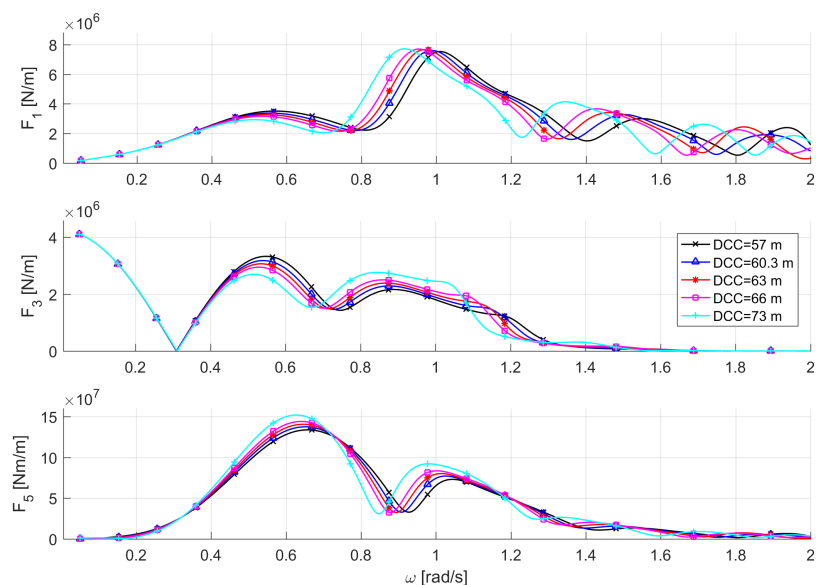
Figure 5.18: First-order wave excitation load amplitudes per unit wave amplitude in surge, heave, and pitch for different DCC.

For long waves, the changes to DCC is relatively small compared to the wavelengths. Therefore, the excitation loads are equal. The heave cancellation frequency is also constant for changing DCC since the draft, heave plates, and columns are equal. At higher wave frequencies, the frequencies giving load maxima and minima in surge, heave, and pitch due to the phase difference between the columns shift to lower wave frequencies as DCC increases, to maintain the same wavelength/DCC ratios. This results in a lower heave excitation force with increasing DCC between the cancellation frequency and the second drop where the wavelength is twice the distance between the columns in x-direction. For frequencies above 0.7 rad/s, the heave force increases with DCC until around 1.1 rad/s. The maximum pitch moment amplitude increases with DCC by a factor of approximately $k^{0.5}$. If increasing DCC increase or decrease the excitation loads depends on the wave frequency.

The wave loads from Morison's equation are given in Figure B.13 and the Morison added mass and linearized viscous damping are given in Figure B.14. The inertia loads and added mass terms increase with increasing DCC at lower frequencies since the element lengths increase. At higher frequencies, if the inertia loads increase or decrease alternates due to different cancellation frequencies. The coefficients in pitch and yaw connected to the drag term increase with DCC since the moment arms increase. There are almost no changes in the surge and heave drag related terms, as the motion RAOs are similar and the heave natural period is constant.

The resulting RAOs in surge, heave, and pitch for different DCC are shown in Figure 5.19.
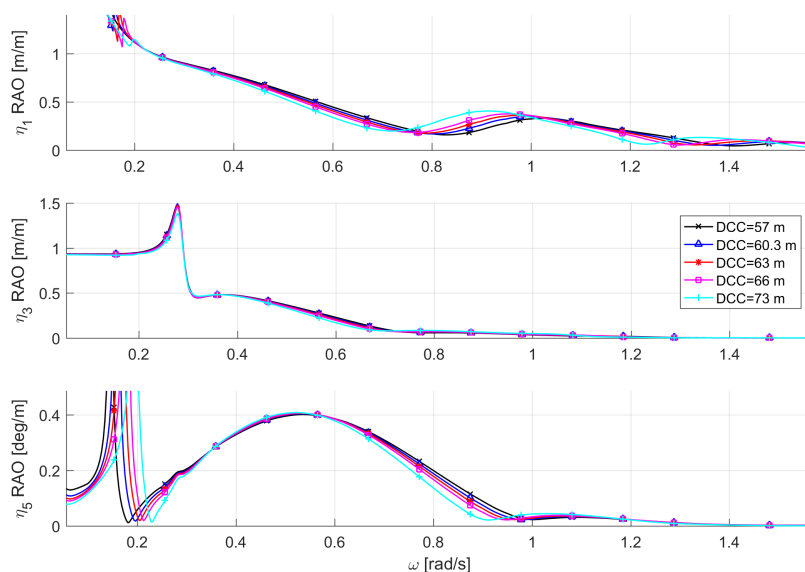
Figure 5.19: Surge, heave, and pitch RAOs for different DCC.

The surge RAO follows the same trends as the surge excitation force since the other surge coefficients do not change much.

The heave RAO is almost unaffected by changing DCC, but show a small decrease with increasing DCC for ω around 0.6 rad/s, where the heave excitation force is lower. As the heave excitation force and the Morison terms are similar at the heave natural frequency, there are almost no differences in the heave RAO maxima.

The pitch motions decrease for wave frequencies lower than the pitch natural frequency since C_{55} increases. Larger C_{55} yields higher natural frequency in pitch. The low pitch motion at frequencies around 0.2 rad/s comes from coupling effects with surge and shifts to higher frequencies when the pitch natural frequency increases. Further, increasing DCC results in higher I_{55} and A_{55} which decreases the pitch RAO at higher frequencies. The pitch RAO maximum around $\omega = 0.55$ rad/s is almost constant, even though the pitch excitation moment maximum increase with DCC, because I_{55} and A_{55} have increased.

A comparison of the internal forces in the cross-section for different DCC is given in Figure 5.20.
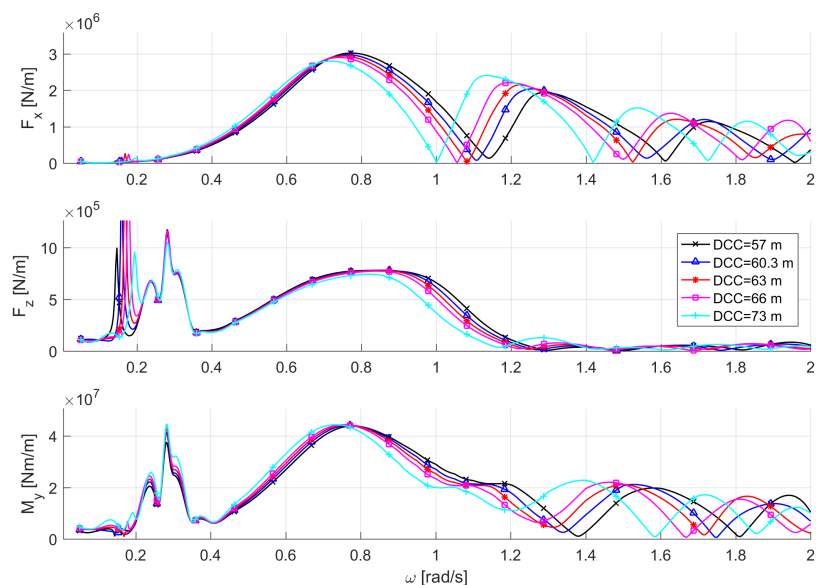
Figure 5.20: Sectional force and moment amplitudes for different DCC.

The amplitude maxima of the internal forces and bending moment do not change much with changing DCC. The cancellation frequencies of the force in x-direction and the bending moment change due to a changing distance between the columns.

A larger cross-sectional bending moment was expected for increasing DCC since the moment arm increases. However, the bending moment amplitudes show only a small increase of about 0.5 MNm from DCC equal 57 meters to 73 meters, corresponding to a 1 % increase in the maximum value, and the maximum moves towards lower frequencies.

The calculated loads acting on the cross-section for DCC 57 and 73 meters are shown in Figure B.15. The figure shows that the forces in z-direction change little, as expected since column 1 is equal and there are only small changes in the heave RAO. The pressure force maximum in x-direction moves towards lower frequencies since the distance between the columns increases, which leads to a lower maximum value with higher DCC. In the wave energy range, the cross-section force maxima in x-direction are about three times larger than the force maxima in z-direction. There is an 8 % decrease in the x-directional cross-sectional force maximum and a 28 % increase in the moment arm related to the forces in z-direction when DCC goes from 57 to 73 meters. The moment arm for the x-directional force does not change. These counteracting effects give less change in the pressure bending moment, which also gives fewer changes in the cross-sectional bending moment. Figure B.15 shows that the pressure bending moment is almost equal for the different DCC. The inertia moment about the y-axis increases with DCC since the arm is larger. This effect lowers the cross-sectional bending moment at frequencies higher than the maximum amplitude.

It should be specified that even though the results show that the bending moment does not increase noticeably with larger DCC, longer truss elements yield that larger diameters and thicknesses are required to maintain the structural integrity of the hull. With larger DCC, the assumption of rigid-body motions is less valid, that is, elasticity in the hull may become important.

5.2.4   Length of Heave Plates

The length of the hexagonal heave plate edge (LHP) is changed to understand the influence of the heave plates. The hexagonal shape and the modeled thickness of 0.4 meters are kept for all analyses. Heave plate edge lengths of 18, 19.7 (baseline design), 22, and 24 meters are used. The effects of changing the heave plate size on the hydrostatic properties are shown in Figure 5.21.
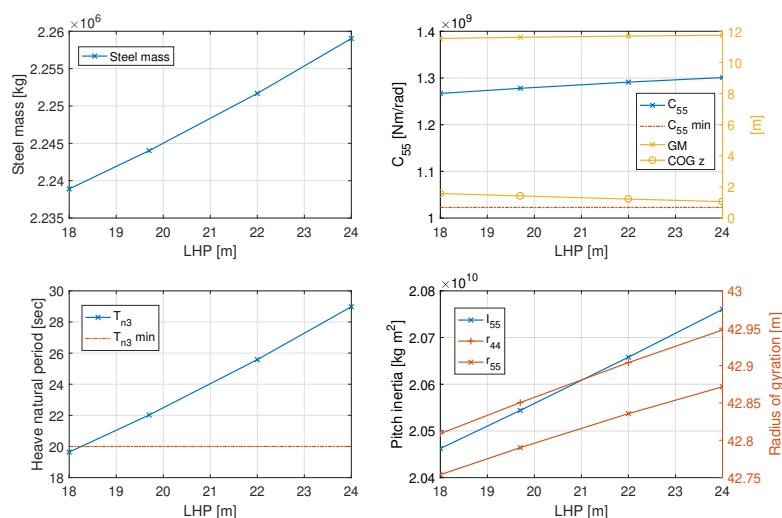
Figure 5.21: Effect of changing LHP on steel mass, pitch restoring coefficient, heave natural period, and pitch inertia. The metacentric height and global z-coordinate of the center of gravity are given at the right axis of the upper right plot. The roll and pitch radii of gyration are given at the right axis of the lower right plot.

The heave plates are in general used to increase the natural period in heave by augmenting the heave added mass. As seen in the figure, the heave natural period is greatly increased with larger heave plates. For the smallest heave plate, the requirement for the minimum heave natural period is not met. If the size of the heave plates is too large, the flow around the heave plates could influence each other.

Changing the size of the heave plate has almost no effect on the steel mass because the steel mass is taken as 20 % of the displaced mass and the heave plates are only a small fraction of the total displacement. In reality, increasing the heave plate size would more significantly influence the steel mass since more reinforcements would be required. Less ballast would then be necessary and the center of gravity would be lowered. As a result, larger heave plates would have a larger positive correlation with C_{55}. The effects on the pitch inertia and radii of gyration are small since the change in mass is small.

The added mass and potential damping diagonal coefficients obtained from *Wadam* for different heave plate sizes are given in Figure 5.22.
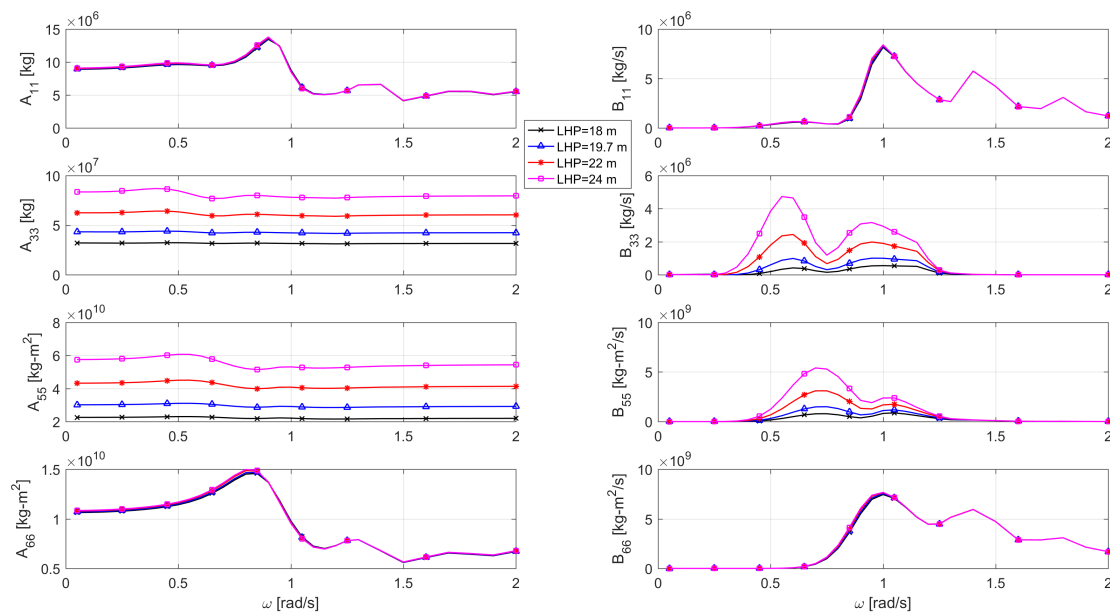
Figure 5.22: Added mass and potential damping coefficients in surge, heave, pitch, and yaw for different LHP calculated by *Wadam*.

As expected, changing the heave plate size does not affect the horizontal motion coefficients, while the heave and pitch added mass and damping increase with increasing heave plate size. From the simplified formula for heave added mass in Section 2.5, the heave added mass should increase by a factor k^3 when the heave plate equivalent diameter increases by k. From the calculations in *Wadam*, both A_{33} and A_{55} increase by a factor slightly higher than k^3, as can be seen in Figure B.16 where the coefficients are normalized by the heave plate length. This is a result of an increasing ratio between the column and heave plate diameters. Further, A_{33} and A_{55} are more frequency-dependent as the size of the heave plate increases, since the submergence-radius ratio decreases. As observed when changing the draft, A_{33} is almost frequency-independent for ratios above one. For high submergence-radius ratios, the potential damping in heave and pitch is low.

The wave excitation loads from *Wadam* in surge, heave, and pitch for different heave plates are shown in Figure 5.23.
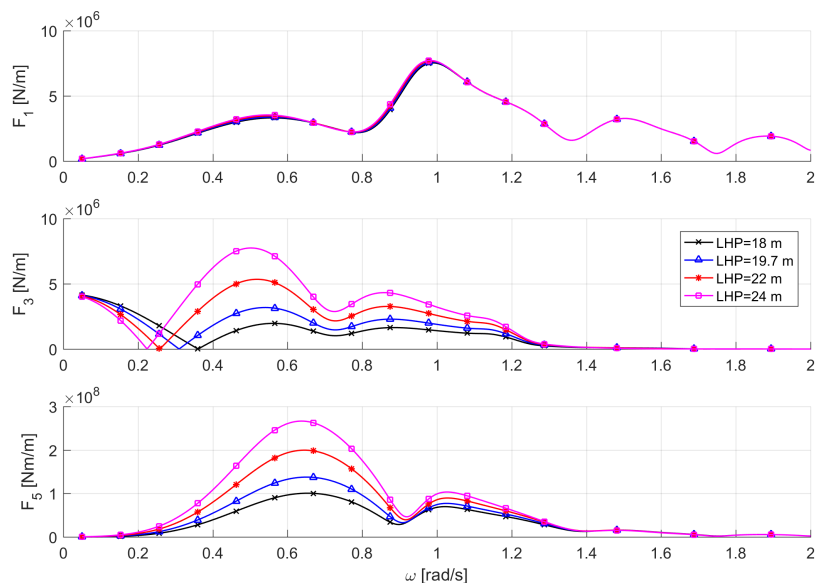
Figure 5.23: First-order wave excitation load amplitudes per unit wave amplitude in surge, heave, and pitch for different LHP.

There are no changes to the surge excitation force as the columns and heave plate thickness are unchanged.

The heave cancellation frequency lowers with a larger heave plate since the ratio between the column and heave plate decreases and the heave added mass increases. At frequencies higher than the cancellation frequency, the heave excitation force amplitudes increase with larger LHP since the added mass term increases while the columns are equal, see equation (C.11). The waterline area is the same, so at very low frequencies the heave force is equal. The phase difference between the columns is the same, resulting in the same second drop for the heave force.

The heave excitation force increases by a factor k^3 in the range $0.7 < \omega < 1.2$ rad/s, the same as the added mass, and by an even higher factor for lower frequencies as can be seen in Figure B.17, where the heave and pitch excitation loads are normalized by dividing by the cube of LHP. From Figure B.17, it could also be seen that the pitch moment increase by a slightly higher factor than k^3 in the range $0.2 < \omega < 0.9$ rad/s.

The wave loads from Morison's equation are given in Figure B.18 and the Morison added mass and linearized viscous damping are given in Figure B.19. The inertia loads and added mass terms are unchanged with changing LHP since the elements are equal. The coefficients in heave and pitch connected to the drag term increase with increasing LHP in the wave energy range since the area of the heave plates increase. There are no changes in the surge and yaw drag related coefficients. At the heave natural frequency, the drag related terms are influenced by the changing heave natural period.

The resulting RAOs in surge, heave, and pitch for different heave plate sizes are given Figure 5.24.
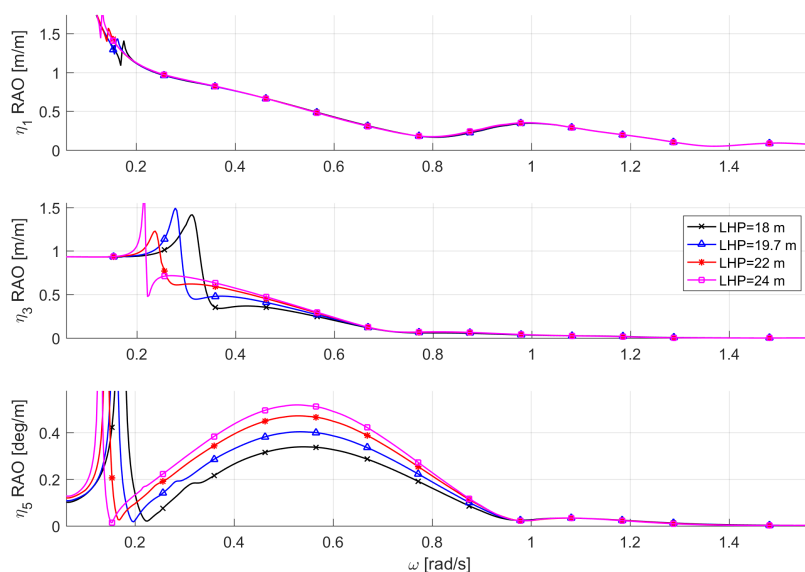
Figure 5.24: Surge, heave, and pitch RAOs for different LHP.

The surge RAOs are equal, except at the pitch natural frequency that changes due to the increased pitch added inertia.

The heave RAOs show how the natural frequency decreases for larger heave plates. This results in larger motions at frequencies higher than the heave cancellation frequency, where the heave excitation force increases with increasing LHP by a higher factor than the added mass. At frequencies above 0.7 rad/s, the heave RAOs are almost equal since both the excitation force and heave added mass increase by $\approx k^3$. The heave added mass is between three to eight times larger than the structural mass. The heave RAO maximum varies because of the varying amplitudes of the drag force and viscous damping.

The pitch motions increase in the wave energy range with larger heave plates. The excitation moment and pitch added inertia increase by $\approx k^3$ in this range, while the pitch inertia is almost constant. The pitch added inertia is between one to three times larger than the pitch inertia. Therefore, the increase in pitch excitation force is larger than the increase in the total inertia, resulting in larger pitch motions. Larger heave plates lower the pitch natural frequency.

A comparison of how the internal forces and bending moment change with different heave plate sizes is given in Figure 5.25.
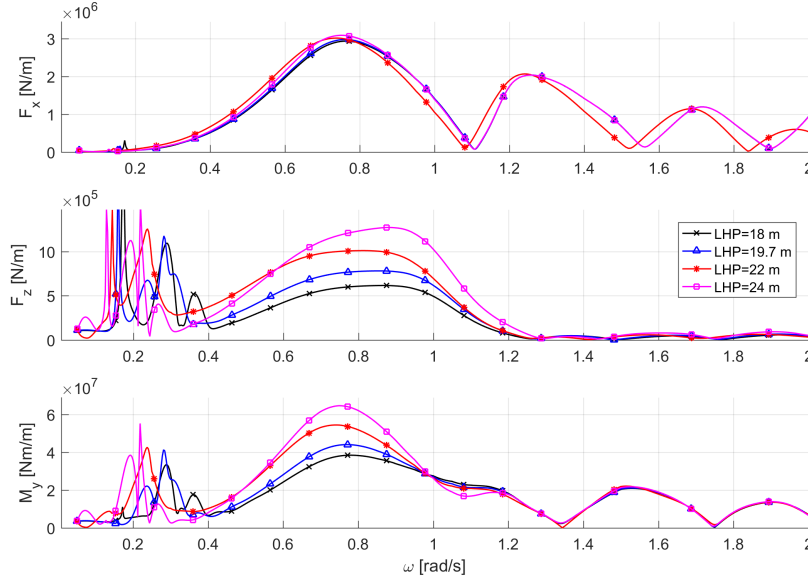
Figure 5.25: Sectional force and moment amplitudes for different LHP.

The internal loads in the cross-section reflect the same trends as the motion RAOs. Increased excitation force in z-direction due to larger heave plates gives a larger cross-sectional force in z-direction and bending moment. In the wave energy range, the maximum values in the z-directional force and bending moment increase by $\approx k^2$, being proportional to the area of the heave plates.

In Figure B.20, the different load components calculated are given for LHP equal to 18 and 24 meters for comparison. It is seen that the pressure force in z-direction and bending moment increase with larger LHP in the wave energy range. There is also an increase in the inertia and restoring force and moment since the motions increase. This counteracts some of the increased pressure moment around 0.5 rad/s, not giving the same increase in the cross-section moment here as for higher frequencies. Higher inertia moment results in lower bending moment around 1.1 rad/s for larger heave plates.

F_x for LHP equal to 22 meters differs from the other heave plate sizes, which is not expected. The analysis was conducted twice, to check for errors in the initial parameters, but the same results were obtained. A reason could be because the pressure force is only calculated at discrete frequencies, and then interpolated between them. A small difference in the output from *Wadam* could result in the creation of a different spline for the pressure force in x-direction for LHP 22 meters, which will affect the cross-sectional force and the cancellation frequencies.

5.2.5   Summary

How the four parameters: 1) the column diameters (column dia), 2) the draft, 3) the distance between the columns (DCC), and 4) the heave plate size (LHP) influence on the design criteria are shown in Figure 5.26. In the following figures, the relative changes are calculated by dividing the values by the related value for the baseline design, being the upscaled 10 MW design presented in Section 5.1.

$$\text{Relative change}[-] = \frac{x_i - x_{baseline}}{x_{baseline}}, \tag{5.3}$$

where x_i is the value and $x_{baseline}$ is the value for the baseline design.
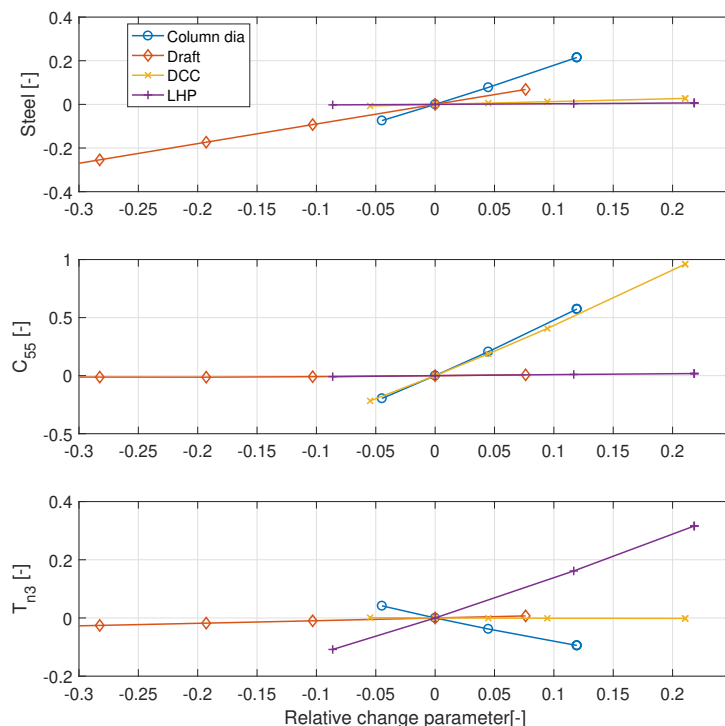
Figure 5.26: Sensitivity analysis of how the parameters affect the design criteria. The results are given as relative changes based on the upscaled design.

The column diameter is the parameter that affects the displacement, and hence, the steel mass the most. The displaced volume of the structure mainly comes from the wet volume of the columns. Therefore, changing the draft is the second most influencing parameter on the steel mass. Changing the distance between the columns or the length of the heave plate sides have almost no effect on the steel mass. This is because of the way the steel mass is estimated, as a fraction of the displaced mass. In real life, longer truss elements would require larger diameters and thicknesses to maintain the structural integrity of the platform and the heave plates would need more reinforcements, increasing the total amount of steel used.

It is seen that changing the distance between columns and increasing the column diameter have almost the same effect on the pitch restoring coefficient, with the column diameter being slightly more effective. However, the increase in the amount of steel is higher when increasing the diameter of the columns, making it in total a less efficient parameter to adjust. Increasing the distance between the columns has a larger effect on the metacentric height, but the displacement increases more with larger column diameter, giving them overall almost the same effect on C_{55}.

Only increasing the heave plate size has a positive effect on the heave natural period. Increasing the column diameter has a negative relation to the heave natural period since the effective area on the top side of the heave plates is reduced and the stiffness is increased. Changing the draft or the distance between the columns have almost no effect on the heave natural period. Increasing the draft has a small positive relation to the heave natural period since the displacement increases.

In Figure 5.27, the relative difference in the standard deviations for surge, heave, and pitch

motions are shown when the parameters are adjusted and for the three selected sea states.

(a) EC1.   **(b)** EC2.   **(c)** EC3.
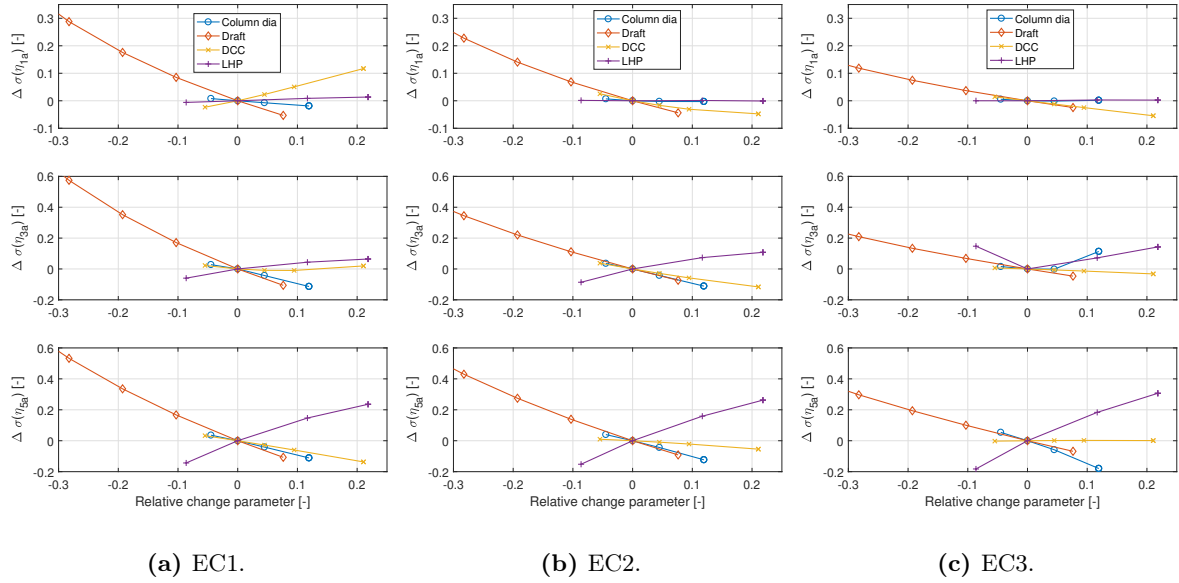
Figure 5.27: Relative change in the standard deviations of the surge, heave, and pitch motions when the parameters are varied and given for the three environmental conditions.

For the surge motions, changing the draft and DCC are the parameters that influence the surge standard deviation the most. Augmenting the draft reduces the surge standard deviations for all EC. Increasing DCC could have a positive or negative effect on the surge standard deviation depending on the EC since the excitation force increase and decrease for different wave frequencies. The column diameter and heave plate do not affect the surge standard deviations.

Larger column diameter gives lower heave motion amplitudes for EC1 and EC2, while for EC3 the heave natural frequency for the largest column is within the wave energy range resulting in a larger standard deviation. The same effect is seen for the smallest heave plate in EC3. In general, larger heave plates give higher heave motion amplitudes. Larger draft decreases the heave motion and adjusting DCC shows no clear trend for all ECs.

It was expected that the heave motions would decrease with decreasing column diameter due to the increase in heave added mass, as found by Leimeister (2016) for the optimized DeepCwind optimized platform. However, it is found that the heave added mass increases by a lower factor than the platform mass decreases for lower column diameters. Also, the heave potential excitation force increases with a lower column diameter, which results in larger heave amplitudes. This difference in results is because the displacement of the columns is a larger fraction of the total displacement on the WindFloat concept than for the DeepCwind hull and since Leimeister (2016) compared the results for an extreme sea state, where the heave natural frequency influences the standard deviation.

In pitch, increasing the column diameter or the draft reduce the motion amplitudes, while larger heave plates have a negative effect on the pitch motion for all ECs. Increasing DCC has a positive effect on the standard deviation for EC1 and EC2, while the differences are almost zero in EC3.

The relative changes in the standard deviations of the horizontal nacelle accelerations are given Figure 5.28. The figure shows similar trends as found for the surge and pitch motions, except for

changing DCC that now gives larger nacelle acceleration with increasing DCC for all ECs. This is because of the increased surge motion at higher frequencies and the phase difference between the surge and pitch motions.

(a) EC1.   **(b)** EC2.   **(c)** EC3.
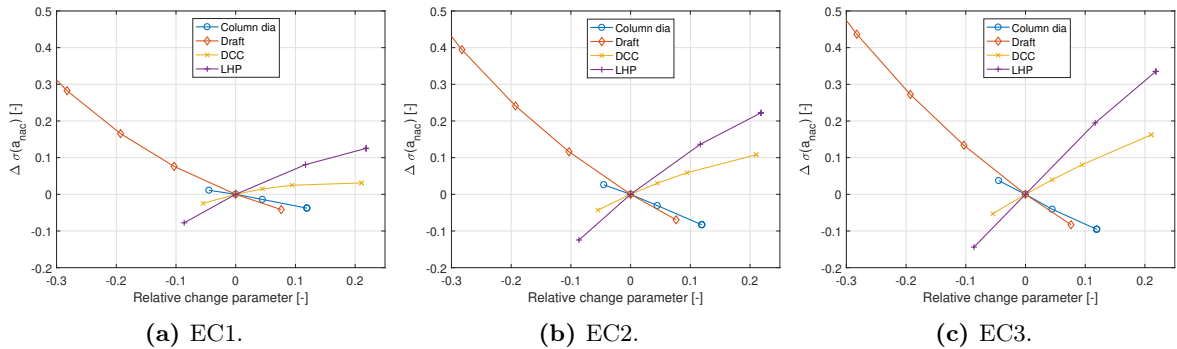
Figure 5.28: Relative change in the standard deviation of the nacelle acceleration when the parameters are varied and given for the three environmental conditions.

As found by Karimi et al. (2017) and summarized in Section 2.3, it is seen that increasing the draft is efficient for reducing the nacelle accelerations, at the price of more steel. However, the optimal design points by Karimi et al. (2017) also showed the trend of reducing the column diameters and increasing the heave plate size will decrease nacelle accelerations and increase cost, while Figure 5.28 show that both of these actions will increase the nacelle acceleration. In this study, a lower column diameter will also decrease the amount of steel required. These differences in conclusions could come from Karimi et al. (2017) including a mooring system, where the optimal semi-submersible designs used angled taut mooring and no ballast. It could also be based on the different environmental conditions evaluated. As seen in Figure 5.28, the changes in nacelle accelerations are lower in EC1 than in EC3 when adjusting the parameters.

The relative changes in the standard deviations of the cross-sectional loads are given in Figure 5.29.

(a) EC1.   **(b)** EC2.   **(c)** EC3.
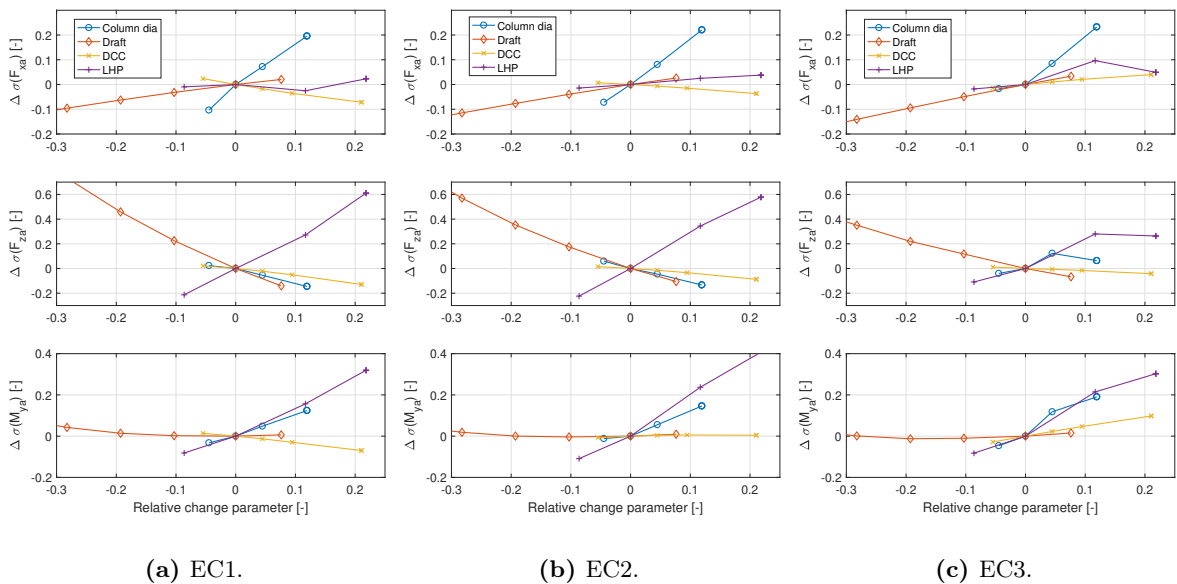
Figure 5.29: Relative change in the standard deviations of the cross section x- and z-force, and bending moment when the parameters are varied and given for the three environmental conditions.

The column diameter has the largest influence on the split force. Also, a larger draft gives higher split force amplitudes. The effect of changing DCC on the split force depends on the EC. The lines for adjusting LHP are affected by the numerical problems with the interpolation of the pressure force but show a small positive relation between larger heave plates and the split force.

For the cross-sectional force in z-direction, a larger draft will reduce the force amplitudes, while larger heave plates increase the force. Increasing the column diameter has a positive effect on the force for EC1 and EC2. For EC3, the force amplitudes close to the heave natural frequency affect the results. Larger DCC gives a small reduction in the standard deviation.

Larger column diameters or heave plates increase the bending moment. Adjusting the draft seems to not influence the bending moment, however, the bending moment maximum increase with a lower draft. Adjusting DCC shows a low positive or negative trend depending on the EC.

A summary of how the different parameters influence the evaluated criteria is given in Table 5.4. When the environmental conditions show different trends, the EC2 is weighted as the most important since EC2 is at rated wind, while the others are for calm or extreme conditions.

Table 5.4: A comparison of how the different parameters influence the design criteria, the responses, and the internal forces and bending moment. $+$ indicates an increased value when the parameter is increased, while $-$ indicates a decreased value when the parameter is increased. The amount of symbols indicates how strong the relation is. 0 indicates no clear trend, and (?) means that the trend depends on the wave frequency and environmental condition.

Value \ Parameter	Column diameter	Draft	DCC	LHP
Steel mass	++	+	0	0
Pitch restoring, C_{55}	++	0	++	0
Heave natural period, T_{n3}	−	0	0	+
Surge, $\sigma(\eta_{1a})$	0	−	− (?)	0
Heave, $\sigma(\eta_{3a})$	− (?)	−−	− (?)	++
Pitch, $\sigma(\eta_{5a})$	−−	−−	−	++
Nacelle accelerations, $\sigma(a_{nac})$	−	−−	+	++
Split force, $\sigma(F_{xa})$	++	+	− (?)	0
Shear force, $\sigma(F_{za})$	−− (?)	−−	−	++
Bending moment, $\sigma(M_{ya})$	+	− (?)	0 (?)	++

5.3 Improved Design

Based on the knowledge gained in the last section, a more efficient design could be suggested. The main goal of a FWT structure is to be as cheap to produce as possible while fulfilling the limiting criteria to motions and internal loads. Therefore, the steel mass should be minimized without a critical increase in the motion amplitudes and/or the cross-sectional loads.

Reducing the column diameter and increasing DCC, will give the best results on the steel mass while maintaining the required stiffness in pitch. However, too large outer dimensions will limit the number of possible places to construct the platform and cause problems with maintaining the structural integrity of the platform.

Reducing the column diameter gives higher heave and pitch motions, and nacelle accelerations. However, it will reduce the split force and bending moment in the cross-section. Further, a reduced column diameter implies that the heave plates could be reduced in size, as long as the structure has a sufficiently large heave natural period. Smaller heave plates give lower motions,

nacelle accelerations, bending moment, and in reality lower steel mass. Smaller heave plates will counteract the increased motions by reducing the column diameter. Increasing DCC gives higher nacelle accelerations and could either increase or decrease the responses depending on the EC. Further, it was found that its influence on the bending moment is low.

The draft should be minimized to decrease the steel mass, however, increasing the draft is the most efficient parameter for reducing the motions and accelerations of the nacelle. It also decreases the maximum cross-sectional bending moment, while the split force is increased. Also, the draft is important for maintaining enough space for the ballast at a low position.

The base diameter of the wind turbine tower is approximately 10.5 meters, giving a lower bound for the column diameter. A too low column diameter requires the DCC to be large and problems with the critical pitch angles will occur. The dimensions of a suggested improved design are given in Table 5.5. The column diameter is reduced, but not to the minimum value, while DCC is increased. This led to the freeboard being increased by one meter, to keep the beams above the sea level at 10 degrees pitch. The heave plates are reduced by almost the same factor as the columns, so the heave natural period still is just above 20 seconds. A DCC of 68.5 meters is slightly larger than for the OO-Star platform that has an equivalent DCC of 64 meters and is lower than the 70 meters presented by Son et al. (2018) for their 10 MW WindFloat hull. They also present a 10-meter column diameter, which is not feasible with the tower used in this thesis. However, their design reflects the findings of this thesis, that the column diameter should be minimized and compensated by a larger DCC. The selected outer dimensions should be feasible, but larger truss member diameters and thicknesses could be necessary. The draft is decreased to 20 meters to further reduce steel weight, even though, this implies larger motions, accelerations, and internal loads as could be seen in Figure 5.30.

Table 5.5: Main dimensions of the improved 10 MW WindFloat structure, and compared to the first upscaled dimensions.

Parameter	Improved [m]	Upscaled [m]
Column diameter	11.5	13.4
Length of heave plate edge	17.5	19.7
Column center to center	68.5	60.3
Main beam and pontoon diameter	2.8	2.8
Bracing diameter	2.0	2.0
Operating draft	20	22.3
Freeboard	11.0	10.0

The improved design scale the column diameter by a lower factor than the rest, as suggested by the scale factors given by Leimeister (2016) and summarized in Section 2.4. However, for the WindFloat concept, an important conclusion from Section 5.2.5 is that the heave plates should be scaled by the same factor as the columns. To maintain a sufficiently large heave natural period, and minimize the responses.

The main platform properties of the improved design are compared against the initial upscaled design in Table 5.6.

Table 5.6: Main design criteria and platform properties of the improved 10 MW design, and compared to the initial upscaled design.

Design criterion	Improved	Upscaled
Steel mass [kg]	1.62E+06	2.24E+06
Volume displacement, ∇ [m^3]	7.89E+03	1.09E+04
Total mass [kg]	8.09E+06	1.12E+07
Static pitch angle [deg]	9.7	8.00
Heave natural period [sec]	21.4	22.0
Roll natural period [sec]	41.5	39.8
Pitch natural period [sec]	41.4	39.8
COG, (x_G, y_G, z_G) [m]	(-0.1243, 0.00, 8.809)	(-0.112, 0.00, 1.422)
Radius of gyration, (r_{xx}, r_{yy}, r_{zz}) [m]	(48.79, 48.72, 38.76)	(42.85, 42.79, 34.40)
Product of inertia, (r_{xy}, r_{xz}, r_{yz}) [m]	(0.00, -26.92, 0.00)	(0.00, -21.41, 0.00)
Ballast fraction column with WT [-]	0.12	0.19
Mass of wind turbine [kg]	1.557E+06	1.568E+06

The steel mass is reduced by 27.7 %, while the criteria to static pitch angle and natural periods are still met. The static pitch angle has increased since DCC was adjusted to give just enough stiffness to meet the criterion. The heave natural period is still above 20 seconds and the natural periods in roll and pitch have increased since the stiffness has decreased more than the inertia and added mass. The center of gravity is higher for the improved design since the ballast is placed higher up and the draft is lower. Less ballast is placed in column one since DCC has increased. For the improved design, the total WT mass has decreased due to the one-meter shorter tower when the freeboard is increased.

It should be emphasized that the suggested improved design is not an optimized design. The relation between lower column diameter and increased DCC needs to be evaluated by a more complete structural analysis. Further, the draft should be set based on weighing the importance of lower steel mass versus higher motion and load RAOs. The draft is also influenced by limiting depths during construction and towing to operation site. In Figure 5.30, the relative changes in the standard deviations of the motions, internal loads, and nacelle accelerations are given for the 5 MW WindFloat platform and the improved design with draft 20 and 22.3 meters, using the initial upscaled platform as the reference structure.
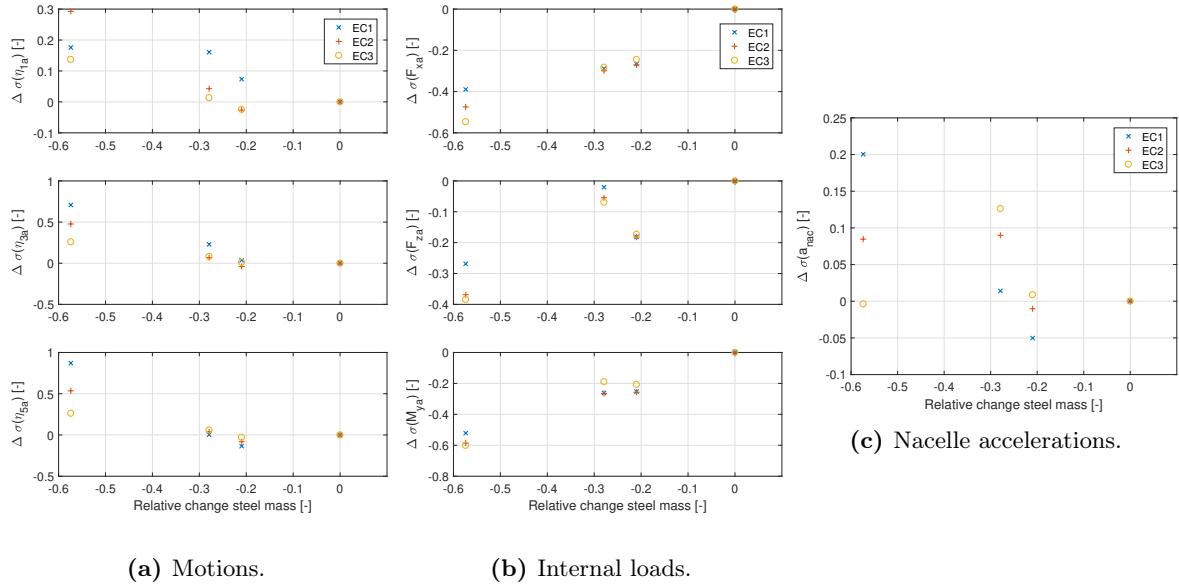
Figure 5.30: Relative changes in the standard deviations of the motions, internal loads, and nacelle accelerations for different designs given as a function of relative change in steel mass. The initial upscaled design is used as the reference design. The 5 MW WindFloat has the lowest steel mass, followed by the improved design, and the improved design with draft 22.3 meters.

From Figure 5.30, it is seen that the improved design with draft 20 meters gives larger motion and nacelle acceleration amplitudes compared to the initial upscaled design. However, the reduction in steel mass is much larger than the increase in responses. Maintaining the draft of the upscaled design and adjusting the other dimensions to the improved values would give responses close to the upscaled design and still a large decrease in steel mass. All of the upscaled designs have lower motion standard deviations than the 5 MW WindFloat platform because the mass and inertia have increased more than the excitation loads. The standard deviations of the nacelle acceleration are also lower for the two heaviest platforms compared to the 5 MW WindFloat. The improved design with low draft has similar nacelle acceleration standard deviation in EC2, lower in EC1, and higher in EC3 compared to the 5 MW platform. The accelerations have increased in EC3, by other means at lower frequencies, since the height of the nacelle is increased. The internal loads are increased compared to the 5 MW design, however, they are lower for the improved designs compared to the initial upscaled one. Therefore, based on a lower standard deviation of the motions and nacelle accelerations compared to the 5 MW WindFloat the draft was reduced to 20 meters. This gives a further reduction of steel mass, and makes, for instance, towing in shallow waters more feasible.

5.4 Effects of Mean Tilt Angle

The effects of modeling and executing the analyses with a tilted platform on the results are studied and discussed in this section. Analyses with a mean tilt angle of ± 5 and ± 10 degrees are carried out. The rotation is about the y-axis (pitch motion). For the negative pitch angles, the waves are propagating in negative x-direction, $\beta = 180$ degrees. For the positive pitch angles and zero pitch, the waves propagate in the positive x-direction. The improved 10 MW design, with the dimensions as given in Table 5.5, is used for the analyses.

When the platform pitch, the heave plates will experience the same rotation and at the same time a vertical displacement, as could be seen in Figure 5.31. For a ± 5 degrees tilt angle, the center of the heave plate at column one will move about -3.4 or 3.5 meters vertically, and the

heave plates at columns two and three will move 1.8 or -1.6 meters vertically, depending on being a positive or negative tilt angle. For a ± 10 degrees tilt angle, heave plate one will move -6.5 or 7.2 meters vertically and the heave plates at columns two and three will move 3.7 or -3.1 meters vertically. As seen in Section 5.2.2, changing the submergence of the heave plates has large effects on the wave loads and responses.
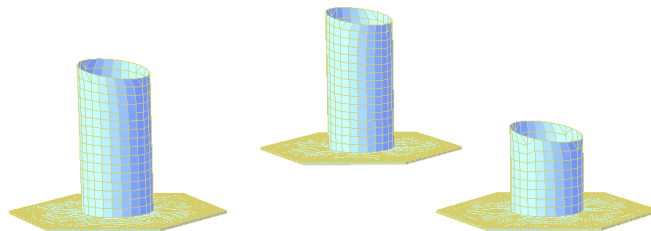
Figure 5.31: Screenshot of the model from *HydroD* with a negative 10 degrees tilt angle. Only half the structure is modeled and meshed in *GeniE*. In *HydroD*, the model is mirrored about the xz-plane.

The effects of the mean tilt angle on the diagonal added mass and damping coefficients are shown in Figure 5.32.
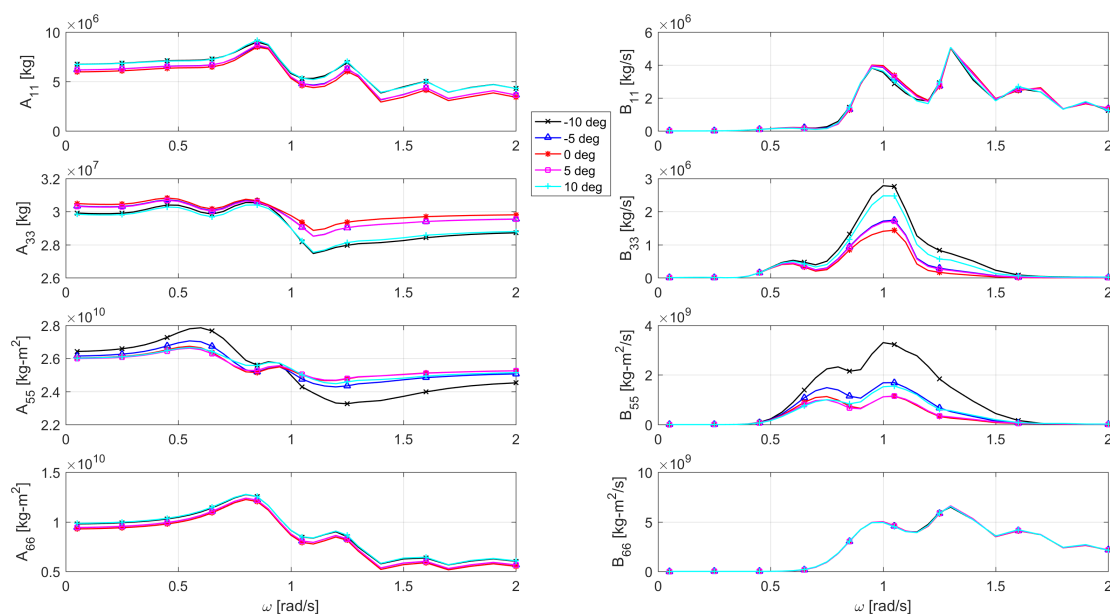
Figure 5.32: Added mass and potential damping coefficients in surge, heave, pitch, and yaw for different tilt angles calculated by *Wadam*.

The added mass in surge and added inertia in yaw are slightly increased when the platform is tilted in both positive and negative directions. A possible explanation for this might be that the projected area of the heave plates in the horizontal motion directions has increased. A_{11} and A_{66} are independent of the platform having a positive or negative tilt angle. At 0.05 rad/s, there is a 12.6 % increase in surge added mass when tilted 10 degrees and a 3.3 % increase for the 5 degrees cases. The related damping terms show minimal changes since they are dependent on the surface generated waves, that mostly comes from the columns.

In heave and pitch, the coefficients are more frequency-dependent with a larger tilt angle. The

effect of a larger tilt angle shows similar development on the heave and pitch coefficients as lowering the draft in Section 5.2.2. In pitch, the trend is especially clear for the -10 degrees tilt angle, which gives the largest vertical displacement of the heave plate at column one. In addition, the heave added mass decreases with a larger tilt angle, probably because of the same effect as for surge and yaw, the projected area of the heave plates in the z-direction is decreased.

The heave plates greatly influence the potential damping, which increases when the heave plates are less submerged, as seen in Section 5.2.2. The damping coefficients increase more with lower submergence of the one heave plate at column one than if the other two heave plates are less submerged because heave plate one experiences a larger vertical displacement.

Further, the structure loses its rotational symmetry when a mean tilt angle is introduced, resulting in coupling effects between surge and heave, and heave and pitch, as could be seen in Figure 5.33. Similar results were also found by Antonutti et al. (2014).
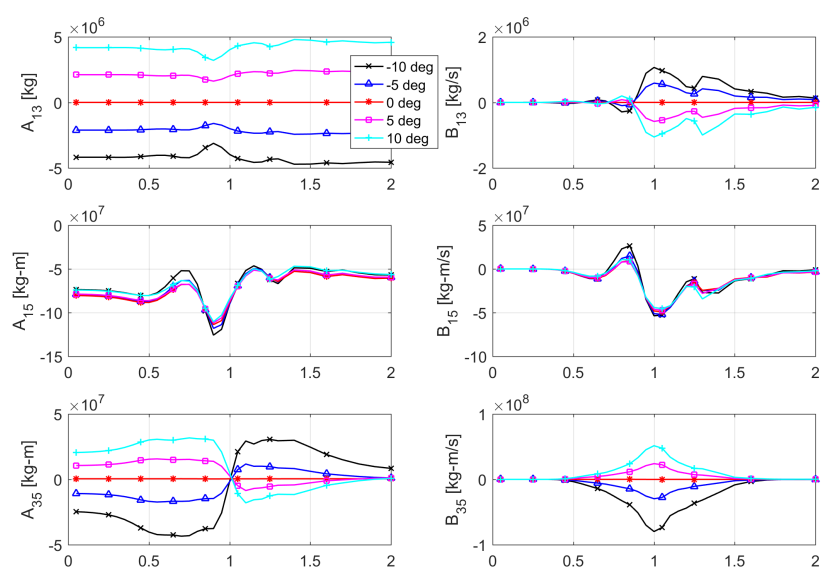
Figure 5.33: Coupled added mass and potential damping coefficients between surge, heave, and pitch for different mean tilt angles.

The potential excitation loads and Morison loads are given in Figure 5.34.
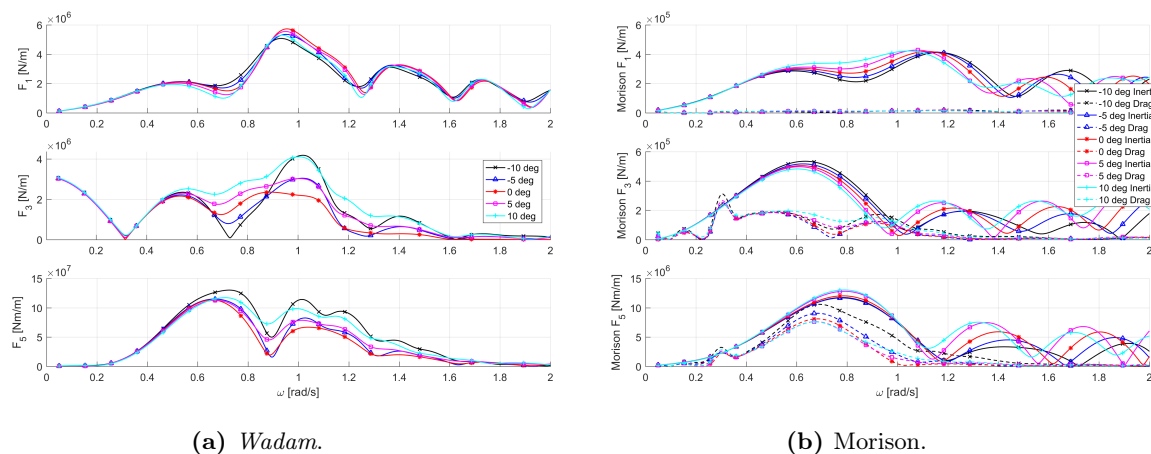
Figure 5.34: Wave excitation load amplitudes in surge, heave, and pitch for different tilt angles. In (a), first-order wave excitation loads from *Wadam* and in (b) from Morison on the slender elements and viscous loads on the heave plates.

The surge excitation force from *Wadam* is affected by the mean tilt angle in the wave energy range. It is seen that for positive tilt angles, the excitation force decreased compared to for the upright structure in the range 0.5-1.3 rad/s. For the negative tilt angles, the surge force increase in the range 0.6-0.9 rad/s. It was expected that the surge excitation forces would increase with larger tilt angles because of a larger projected area of the heave plates, as for the surge and yaw added mass. As seen in Figure 5.13, the surge force decrease when the draft is reduced. For a positive tilt angle, the two columns at negative x-coordinates are reduced in wet length and this is compensated by a larger draft at column one. The surge force is mostly affected by the wave dynamics close to the surface. Therefore, two shorter columns compensated by one at a larger draft will result in lower surge force, because there is a lower increase in wave forces acting on the lower part of column one than the decrease in wave forces by lower draft on the two other columns. For the case of a negative tilt angle, two of the columns have slightly increased wet lengths while only column one has less, resulting in a larger surge force. From Section 5.2.1, it was seen that using the inertia term of Morison's equation on the columns gave a good approximation of the surge excitation force up to 0.9 rad/s. The inertia force on the columns with different tilt angles are calculated and compared against the surge force from Wadam with 10 degrees tilt in Figure 5.35. It is seen that estimating the surge force with Morison's equation on the columns gives similar results as seen in Figure 5.34 for wave frequencies up to 0.9 rad/s. Therefore, it could be assumed the rotation of the heave plates has minimal influence on the surge potential excitation force. At higher wave frequencies, the ellipse shape of the cylinders and that they are not parallel to the z-axis affect the surge force.
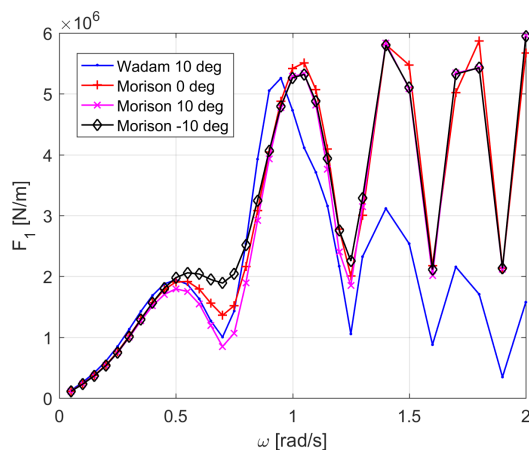
Figure 5.35: The surge wave excitation force amplitudes calculated by *Wadam* with 10 degrees tilt is compared with the inertia force on the columns with different tilt angles using Morison's equation. $C_a = 1.0$ is used for the columns in Morison's equation.

The heave excitation force is equal for low wave frequencies, as for changing the draft, since the wavelengths are much longer than the changing vertical displacements of the heave plates and the columns and heave plates are unchanged. Around 0.7 rad/s, when the wavelength is twice the distance in the x-direction between the columns, there are large differences in the heave force. For the -10 degrees tilt angle, the heave force is canceled since the force on the heave plate at column one increase and equals the force on the two other heave plates, which has decreased, and the forces are 180 degrees out of phase. For the positive tilt angles, two of the heave plates have lower submergence, which results in higher heave forces for all frequencies above the heave cancellation frequency compared to for the upright model. Around 1 rad/s, the heave force is almost doubled for the cases of ± 10 degrees tilt angles compared to the upright case. The results are similar as found by Antonutti et al. (2014) for the Dutch Tri-floater.

The pitch excitation moment is in general increased compared to the upright case. In the wave energy range, the pitch moment increases the most for negative pitch angles since the surge excitation force increases.

The wave loads from Morison's equation are given in Figure 5.34b and the Morison added mass and linearized viscous damping coefficients are given in Figure B.21. The Morison loads are low compared to the potential wave excitation loads and the inertia terms are still dominating. In surge, the inertia loads increase with a larger positive tilt angle in the wave energy range since the pontoon and bracing connecting column two and three are closer to the surface. The drag loads in surge increase at low frequencies for the positive tilt angles and decrease for the negative angles compared to the upright, A reason for this could be the proximity of one or two heave plates to the surface. The inertia force in heave on the slender elements shows the opposite trend of the surge inertia force, as the heave force is more dependent on the elements connecting column one to column two and three. The heave drag force shows a small increase for the tilted platforms as one or two of the heave plates are closer to the surface. There are only minor changes in the Morison added mass terms due to the bracing being more or less submerged, and the damping coefficients show no clear trends.

The resulting motion RAOs in surge, heave, and pitch for different tilt angles are compared against the upright improved design in Figure 5.36.
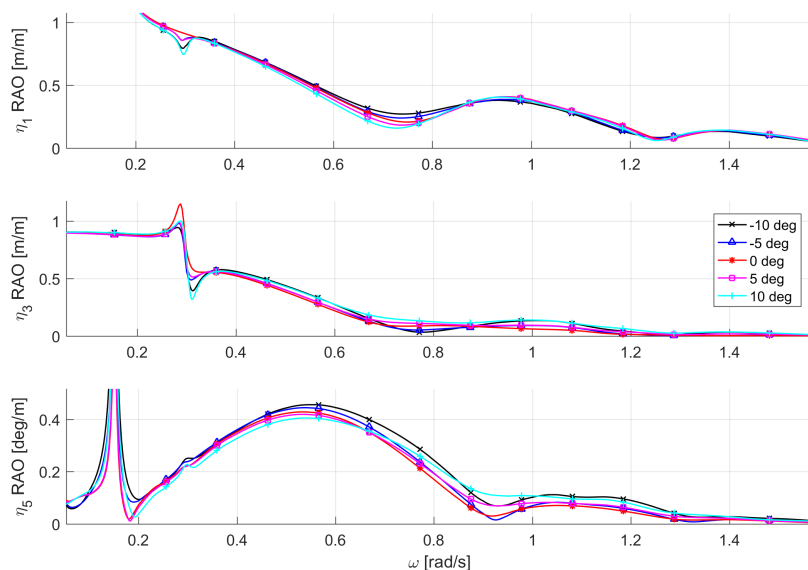
Figure 5.36: Surge, heave, and pitch RAOs for different tilt angles.

The surge RAO reflects the changes in the surge excitation force since the mass and restoring matrices are equal, and there is only a small increase in the surge added mass. The surge excitation force increases by 24 % for the -10 degrees tilt angle and decreases by 34 % for the 10 degrees tilt angle at 0.7 rad/s, while the added mass increased by about 13 %. The effect of the new coupled terms between surge and heave are visible at the heave natural frequency.

Also, the heave and pitch RAOs reflect the changes in the excitation loads as the mass and restoring matrices are unchanged. The coupling between heave and pitch are seen at the natural frequencies. The relative changes in the standard deviations of the motions and nacelle accelerations are given in Figure 5.38 for the three different environmental conditions. The reason for the heave motion being more canceled at the heave cancellation frequency when the platform is tilted could again be because of the iterative method used for solving Morison's equation.

The internal loads calculated in the cross-section are given in Figure 5.37 for different tilt angles.
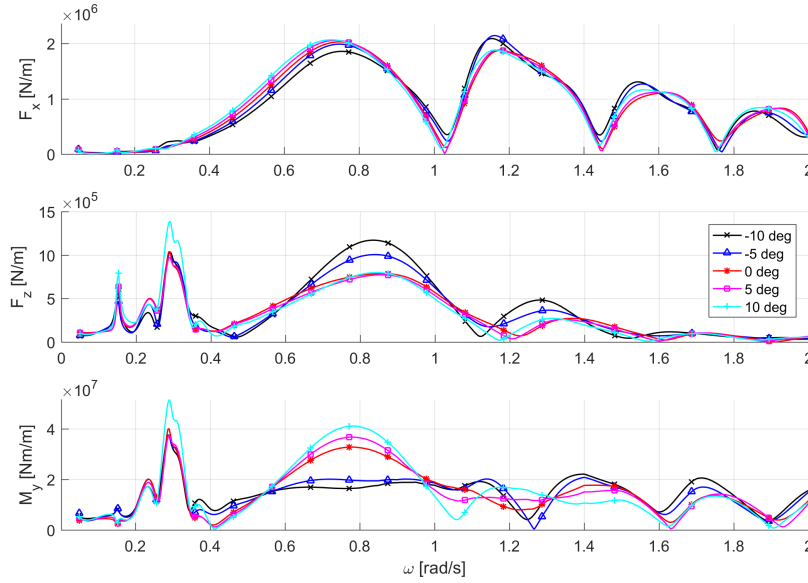
Figure 5.37: Sectional force and moment amplitudes for different tilt angles.

The sectional force in the x-direction shows the opposite trend of the surge excitation force at lower frequencies. This is because the cross-sectional loads are in equilibrium with the forces acting on column one. With lower (or more negative) tilt angle, less of column one is submerged resulting in lower split forces. The cancellation frequencies are the same since the distance between the columns is constant.

The cross-section force in the z-direction is increased with negative tilt angles since the heave plate at column one is then closer to the surface. The differences between the positive tilt angles and the upright case are small, as the vertical displacement of the heave plate is then lower, and the excitation loads are less sensitive to changes to larger draft since the wave dynamics decrease exponentially with the depth, e^{kz_m}, see Appendix C.

In the wave energy range, the bending moment is greatly reduced with the negative tilt angles and is slightly increased for the positive tilt angles. In Figure B.22, the different internal load components are plotted and compared for the zero and ± 10 degrees tilt angles. The pressure bending moment is greatly increased for the -10 degrees tilt angle. However, the inertia moment is also increased due to larger pitch motions. This results in the cross-section bending moment to decrease compared to the upright case since the increased pressure and inertia moments cancel each other. For the positive tilt angles, the pressure moment is lower than for the upright case, but the pitch motion has increased in the range with the maximum bending moment, which gives a larger increase in the inertia moment and the cross-section bending moment.

The relative changes of the standard deviations of the motions, internal loads, and nacelle accelerations are given in Figure 5.38 for the three selected environmental conditions. It is seen that the heave standard deviation for EC1 increases with 59 % when the structure is tilted 10 degrees. In pitch, the largest change is again for EC1 when the platform is tilted -10 degrees. The differences in the surge standard deviations are lower. For EC3, the differences in surge, heave, and pitch are lower since the excitation loads are similar for lower wave frequencies. The standard deviation of the bending moment decreases by 32 % when the platform has a -10 degrees tilt and increases by 22 % for a positive 10 degrees tilt angle. Also, for the cross-section loads, the differences in the x-direction are lower. The standard deviation of the nacelle accelerations

increases by 31 % for the platform with -10 degrees tilt angle in EC1 and EC2. The nacelle accelerations increase for both positive and negative tilt angles since the pitch motion increases, and especially due to the differences in the pitch RAOs at higher frequencies (EC1).

The results show that the effect of the mean tilt angle should be accounted for when modeling and designing a FWT structure, especially for FWT structures equipped with heave plates since the submergence of these greatly influences the responses of the structure. However, the goal of an active ballast system is always to keep to platform as upright as possible, and minimizing these effects. It is seen from the figure that the relative changes are lower for the ± 5 degrees tilt angles, which are more likely to occur during operation than a ± 10 degrees tilt angle.

(a) Motions.

(b) Internal loads.

(c) Nacelle accelerations.
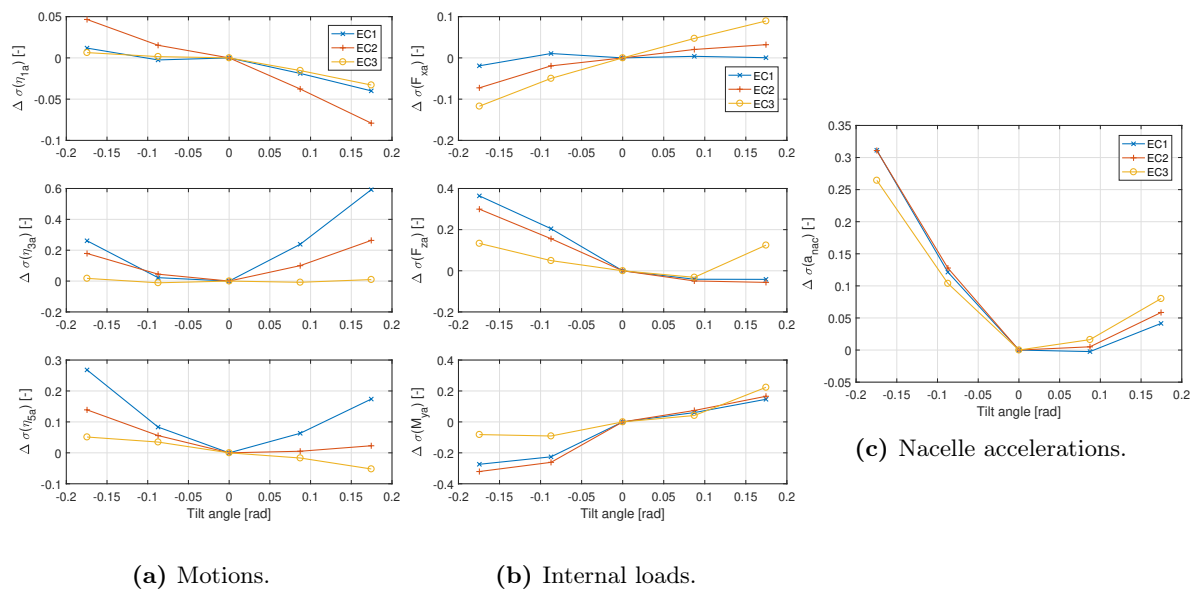
Figure 5.38: Relative changes in the standard deviations of the motions, internal loads, and nacelle accelerations for different tilt angles and given for the three environmental conditions. The upright model is used as reference.

6   Conclusion and Recommendations

6.1   Conclusion

This thesis set out to investigate the effects different design parameters have on the behavior of a semi-submersible FWT platform. The goal is a cost-effective design, while satisfying strength and safety requirements. This study was carried out by calculating hydrostatic properties in *MATLAB*, and hydrodynamic coefficients for the designs using the first-order potential theory program *Wadam*. The WindFloat concept was chosen and upscaled to support the 10 MW DTU RWT. The hull was parameterized by defining four dimensions that describe the main properties of the structure: 1) the column diameter, 2) the draft, 3) the distance between the columns, and 4) the heave plate size.

This study has shown that increasing the draft is the most important parameter for reducing the platform motions and nacelle accelerations. However, the drawbacks are increased steel mass and higher split forces between the columns. The heave plates are important appendices on the WindFloat concept, giving the upscaled structure a heave added mass four times larger than the structural mass. This effect shifts the heave natural period of the platform outside the wave energy range. However, the study has shown that larger heave plates increase the heave and pitch motions, nacelle accelerations, and shear force and bending moment in the cross-section. A conclusion from this is that the heave plates should be minimized in size, while the heave natural period is maintained outside the wave energy range.

The wind turbine thrust overturning moment is an important design driver and is counteracted by the pitch restoring coefficient. For achieving a higher pitch restoring coefficient, it is found that increasing the column diameter is slightly more effective than increasing the distance between the columns. However, the steel mass increases more with the column diameter. From the calculations of internal loads, a larger distance between columns did not introduce a larger bending moment in the cross-section, however, this could be a result of the simplifications used and needs further evaluation. Increasing the distance between the columns gives a small increase in the nacelle accelerations. It is found that increasing the column diameter decreases motions and nacelle acceleration standard deviations, due to a larger structural mass and a lower difference between the columns and the heave plates. However, a larger column diameter increases the internal split force and bending moment. The relative effect of changing the heave plate size on the motions standard deviations is larger than changing the column diameter.

To conclude, based on the findings from the parametric study an improved cost-effective design is suggested where: 1) the column diameter and heave plates are scaled down to minimize steel mass and responses, 2) the distance between the columns is increased to maintain the stiffness in pitch, and 3) the draft is to be set based on evaluating using less steel versus higher responses and internal loads.

The conclusion from including a mean tilt angle on the platform in the analyses is that the effect should be accounted for when modeling and designing a FWT structure in some cases. A 31 % increase in the standard deviation of the nacelle accelerations was found when a -10 degrees tilt angle was introduced. Especially for FWT structures equipped with heave plates, the effects from a mean tilt angle could be important since the submergence of these greatly influences the responses of the structure. The study identified that the effects of a mean tilt angle on the motion RAOs are larger in the high frequency end of the wave energy range. For low frequency waves or low tilt angles, the effects of the mean tilt angle on the responses are low.

6.2   Recommendations for Further Work

In the thesis, some assumptions are made, and some effects are not included in the analyses due to time limitations. The following list presents recommendations for further work of effects that should be included in the parametric study of a semi-submersible FWT design.

- How different hull shapes influence the second-order effects from waves should be evaluated. Especially, second-order effects on the surge and pitch motions could be important since their natural periods are outside the wave energy range.

- Viscous effects on the heave plates should be further analyzed. The viscous effects on the added mass coefficients are not included in this thesis, nor corrections to the drag coefficients. Also, the effects of the heave plate thickness and reinforcements should be evaluated in a future parametric study.

- Assess the effects of different hull shapes when wind loads are introduced. Coupled wave-wind analyses where wind loads on the structure and WT are included. Aerodynamic damping should be included, and the effects of wave-wind misalignment could be studied.

- A mooring system is not evaluated in this thesis. The weight and stiffness provided by the mooring system should be included in further analyses. Also, evaluating different mooring systems in combination with different hull shapes could be of interest.

- A more detailed structural analysis where structural flexibility is included and loads in the truss members are estimated should be carried out, to further understand the effects of increasing the distance between the columns.

- A structural analysis evaluating the strength of the structure could be of interest. Requirements to the diameters and wall thickness of the structural components could be estimated, including the WT tower and reinforcements on the heave plates. The steel mass could be calculated based on found thicknesses and could be used in the evaluation of the different designs.

- A detailed cost analysis should be included in the evaluation of the different parameters, where the cost of material, mooring, and fabrication are evaluated.

7 References

Antonutti, R., Peyrard, C., Johanning, L., Incecik, A., and Ingram, D. (2014) An investigation of the effects of wind-induced inclination on floating wind turbine dynamics: heave plate excursion. *Ocean Engineering,* 91, pp. 208–217. DOI: 10.1016/j.oceaneng.2014.09.008.

— (2016) The effects of wind-induced inclination on the dynamics of semi-submersible floating wind turbines in the time domain. *Renewable Energy,* 88, pp. 83–94. DOI: 10.1016/j.renene.2015.11.020.

Aubault, A., Cermelli, C., and Roddier, D. (2009) WindFloat: A Floating Foundation for Offshore Wind Turbines—Part III: Structural Analysis. *ASME 2009 28th International Conference on Ocean, Offshore and Arctic Engineering.* Honolulu, Hawaii, USA, May 31–June 5, 2009. Vol. 1: Offshore Technology. Honolulu: ASME, pp. 213–220. DOI: 10.1115/omae2009-79232.

Bachynski, E. E. and Moan, T. (2012) Design considerations for tension leg platform wind turbines. *Marine Structures,* 29(1), pp. 89–114. DOI: 10.1016/j.marstruc.2012.09.001.

Bachynski, E. E. (2014) *Design and Dynamic Analysis of Tension Leg Platform Wind Turbines.* Doctoral thesis. Department of Marine Technology, NTNU. Available at: https://ntnuopen.ntnu.no/ntnu-xmlui/handle/11250/238768 (accessed: 03/08/2020).

Bak, C., Zahle, F., Bitsche, R., Kim, T., Yde, A., Henriksen, L. C., Andersen, P. B., Natarajan, A., and Hansen, M. H. (2013) Design and performance of a 10 MW wind turbine. *Wind Energy,* 124.

Borgman, L. E. (1958) Computation of the ocean-wave forces on inclined cylinders. *Eos, Transactions American Geophysical Union,* 39(5), pp. 885–888. DOI: 10.1029/TR039i005p00885.

Cermelli, C., Roddier, D., and Aubault, A. (2009) WindFloat: A Floating Foundation for Offshore Wind Turbines—Part II: Hydrodynamics Analysis. *ASME 2009 28th International Conference on Ocean, Offshore and Arctic Engineering.* Honolulu, Hawaii, USA, May 31–June 5, 2009. Vol. 4: Ocean Engineering; Ocean Renewable Energy; Ocean Space Utilization, Parts A and B. Honolulu: ASME, pp. 135–143. DOI: 10.1115/omae2009-79231.

Cruz, J. and Atcheson, M. (2016) *Floating Offshore Wind Energy: The Next Generation of Wind Energy.* The Next Generation of Wind Energy. Cham: Springer International Publishing, Cham. DOI: 10.1007/978-3-319-29398-1.

DNV GL AS (2017a) HydroD V4.10-01.

— (Oct. 2017b) *Sesam User Manual HydroD.* DNV GL AS.

— (July 2018) *DNV GL standards: Floating wind turbine structures (DNVGL-ST-0119).* Available at: https://rules.dnvgl.com/docs/pdf/DNVGL/ST/2018-07/DNVGL-ST-0119.pdf (accessed: 03/30/2020).

— (Sept. 2019a) *DNV GL recommended practice: Environmental conditions and environmental loads (DNVGL-RP-C205).* Available at: https://oilgas.standards.dnvgl.com/download/dnvgl-rp-c205-environmental-conditions-and-environmental-loads (accessed: 04/06/2020).

— (2019b) GeniE V7.13-11.

— (Nov. 2019c) *Sesam User Manual GeniE.* DNV GL AS.

— (June 2019d) *Sesam User Manual Wadam.* DNV GL AS.

— (2019e) Wadam V9.6-19.

Dr.techn.Olav Olsen (2020) *Renewable energy.* Available at: https://www.olavolsen.no/en/business-areas/renewable-energy (accessed: 02/04/2020).

Equinor (Oct. 11, 2019) *Investing in Hywind Tampen development.* Available at: https://www.equinor.com/en/news/2019-10-11-hywind-tampen.html (accessed: 01/31/2020).

— (2020) *Equinor — the world's leading floating offshore wind developer.* Available at: https://www.equinor.com/en/what-we-do/hywind-where-the-wind-takes-us.html (accessed: 01/31/2020).

Faltinsen, O. M. (1990) *Sea Loads on Ships and Offshore Structures*. Cambridge: Cambridge University Press.

Fukushima Offshore Wind Consortium (2020). Available at: http://www.fukushima-forward.jp/english/index.html (accessed: 02/04/2020).

Galván, J., Sánchez-Lara, M. J., Mendikoa, I., Pérez-Morán, G., Nava, V., and Rodríguez-Arias, R. (2018) NAUTILUS-DTU10 MW Floating Offshore Wind Turbine at Gulf of Maine: Public numerical models of an actively ballasted semisubmersible. *Journal of Physics: Conference Series,* 1102, p. 012015. DOI: 10.1088/1742-6596/1102/1/012015.

Greco, M. (2012) *Lecture Notes TMR4215: Sea Loads*. Trondheim: Department of Marine Technology, NTNU.

Hall, M., Buckham, B., and Crawford, C. (2013) Evolving offshore wind: A genetic algorithm-based support structure optimization framework for floating wind turbines. *2013 MTS/IEEE OCEANS - Bergen*. Bergen, Norway, June 10–14, 2013. Bergen: IEEE, pp. 1–10. DOI: 10.1109/OCEANS-Bergen.2013.6608173.

Hall, M., Buckham, B., and Crawford, C. (2014) Hydrodynamics-based floating wind turbine support platform optimization: A basis function approach. *Renewable Energy,* 66, pp. 559–569. DOI: 10.1016/j.renene.2013.12.035.

Housseine, C. O., Monroy, C., and Hauteclocque, G. de (2015) Stochastic Linearization of the Morison Equation Applied to an Offshore Wind Turbine. *ASME 2015 34th International Conference on Ocean, Offshore and Arctic Engineering*. St.John's, NL, Canada, May 31–June 5, 2015. Vol. 9: Ocean Renewable Energy. St.John's, NL, Canada: ASME. DOI: 10.1115/omae2015-41301.

Ideol (2018) *Our projects*. Available at: https://www.ideol-offshore.com/en/our-projects (accessed: 02/03/2020).

IEA (2019) *Offshore Wind Outlook 2019*. Paris: IEA. Available at: https://www.iea.org/reports/offshore-wind-outlook-2019 (accessed: 01/30/2020).

IRENA (2019) *Renewable Power Generation Costs in 2018*. Abu Dhabi: International Renewable Energy Agency. Available at: https://www.irena.org/publications/2019/May/Renewable-power-generation-costs-in-2018 (accessed: 01/31/2020).

Jonkman, J., Butterfield, S., Musial, W., and Scott, G. (2009) *Definition of a 5-MW Reference Wind Turbine for Offshore System Development*. Golden, Colorado, USA: National Renewable Energy Laboratory. Available at: https://www.nrel.gov/docs/fy09osti/38060.pdf (accessed: 02/20/2020).

Karimi, M., Hall, M., Buckham, B., and Crawford, C. (2017) A multi-objective design optimization approach for floating offshore wind turbine support structures. *Journal of Ocean Engineering and Marine Energy,* 3(1), pp. 69–87. DOI: 10.1007/s40722-016-0072-4.

Karimirad, M. and Michailides, C. (2015) V-shaped semisubmersible offshore wind turbine: An alternative concept for offshore wind technology. *Renewable Energy,* 83, pp. 126–143. DOI: 10.1016/j.renene.2015.04.033.

Kvittem, M. I. and Moan, T. (2015) Time domain analysis procedures for fatigue assessment of a semi-submersible wind turbine. *Marine Structures,* 40, pp. 38–59. DOI: 10.1016/j.marstruc.2014.10.009.

Kvittem, M. I. (2014) *Modelling and response analysis for fatigue design of a semi-submersible wind turbine*. Doctoral thesis. Department of Marine Technology, NTNU. Available at: https://ntnuopen.ntnu.no/ntnu-xmlui/bitstream/handle/11250/239262/Marit_Irene_Kvittem_PhD.pdf?sequence=3&isAllowed=y (accessed: 03/08/2020).

Leimeister, M. (2016) *Rational Upscaling and Modelling of a Semi-Submersible Floating Offshore Wind Turbine*. Master thesis. Department of Marine Technology, NTNU. Available at: https://ntnuopen.ntnu.no/ntnu-xmlui/handle/11250/2397151?locale-attribute=no (accessed: 03/25/2020).

LIFES50+ (2020) *Innovative Floating Offshore Wind Energy*. Available at: https://lifes50plus.eu (accessed: 02/04/2020).

Lopez-Pavon, C. and Souto-Iglesias, A. (2015) Hydrodynamic coefficients and pressure loads on heave plates for semi-submersible floating offshore wind turbines: A comparative analysis using large scale models. *Renewable Energy,* 81, pp. 864–881. DOI: 10.1016/j.renene.2015.04.003.

Luan, C., Chabaud, V., Bachynski, E. E., Gao, Z., and Moan, T. (2017) Experimental validation of a time-domain approach for determining sectional loads in a floating wind turbine hull subjected to moderate waves. *Energy Procedia,* 137, pp. 366–381. DOI: 10.1016/j.egypro.2017.10.361.

Luan, C., Gao, Z., and Moan, T. (2016) Design and Analysis of a Braceless Steel 5-MW Semi-Submersible Wind Turbine. *ASME 2016 35th International Conference on Ocean, Offshore and Arctic Engineering*. Busan, South Korea, June 19–24, 2016. Vol. 6: Ocean Space Utilization; Ocean Renewable Energy. V006T09A052: ASME. DOI: 10.1115/omae2016-54848.

— (2017) Development and verification of a time-domain approach for determining forces and moments in structural components of floaters with an application to floating wind turbines. *Marine Structures,* 51, pp. 87–109. DOI: 10.1016/j.marstruc.2016.10.002.

Moreno, J., Thiagarajan, K. P., and Cameron, M. (2016) Hydrodynamic Coefficients of Hexagonal Heave Plates for Floating Offshore Wind Turbine Platforms. *ASME 2016 35th International Conference on Ocean, Offshore and Arctic Engineering*. Busan, South Korea, June 19–24, 2016. Vol. 6: Ocean Space Utilization; Ocean Renewable Energy. V006T09A032: ASME. DOI: 10.1115/omae2016-54139.

Ohta, M., Komatsu, M., Ito, H., and Kumamoto, H. (2013) Development of a V-shaped Semi-submersible Floating Structure for 7MW Offshore Wind Turbine. *International Symposium on Marine and Offshore Renewable Energy*. Tokyo, Japan, Oct. 28–30, 2013. Tokyo.

Pettersen, B. (2007) *Compendium TMR4247: Marine Technology Hydrodynamics (In Norwegian)*. Trondheim: Department of Marine Technology, NTNU.

Principle Power (2019) *WindFloat*. Available at: http://www.principlepowerinc.com/en/windfloat (accessed: 02/03/2020).

— (Jan. 2, 2020) *WindFloat Atlantic project starts supplying clean energy in Portugal*. Available at: http://www.principlepowerinc.com/en/news-press/press-archive/2020/01/02/windfloat-atlantic-project-starts-supplying-clean-energy-in-portugal (accessed: 02/03/2020).

Robertson, A., Jonkman, J., Masciola, M., Song, H., Goupee, A., Coulling, A., and Luan, C. (Sept. 2014) *Definition of the Semisubmersible Floating System for Phase II of OC4*. Golden, Colorado, USA: National Renewable Energy Laboratory. DOI: 10.2172/1155123. Available at: https://www.nrel.gov/docs/fy14osti/60601.pdf (accessed: 02/13/2020).

Roddier, D., Cermelli, C., and Weinstein, A. (2009) WindFloat: A Floating Foundation for Offshore Wind Turbines—Part I: Design Basis and Qualification Process. *ASME 2009 28th International Conference on Ocean, Offshore and Arctic Engineering*. Honolulu, Hawaii, USA, May 31–June 5, 2009. Vol. 4: Ocean Engineering; Ocean Renewable Energy; Ocean Space Utilization, Parts A and B. Honolulu: ASME, pp. 845–853. DOI: 10.1115/omae2009-79229.

Roddier, D., Peiffer, A., Aubault, A., and Weinstein, J. (2011) A generic 5 MW WindFloat for numerical tool validation & comparison against a generic spar. *OMAE2011-50278*. Rotterdam, The Netherlands, June 19–24, 2011. Rotterdam: ASME.

Sarpkaya, T. (1986) Force on a circular cylinder in viscous oscillatory flow at low Keulegan—Carpenter numbers. *Journal of Fluid Mechanics,* 165, pp. 61–71. DOI: 10.1017/S0022112086002999.

Son, D., Pinguet, R., and Roddier, D. (2018) Global Sizing of the WindFloat for a 10 MW Generic Wind Turbine. *ASME 2018 1st International Offshore Wind Technical Conference*. San Francisco, CA, Nov. 4–7, 2018. V001T01A035: ASME. DOI: 10.1115/iowtc2018-1104.

Tao, L., Molin, B., Scolan, Y. M., and Thiagarajan, K. (2007) Spacing effects on hydrodynamics of heave plates on offshore structures. *Journal of Fluids and Structures,* 23(8), pp. 1119–1136. DOI: 10.1016/j.jfluidstructs.2007.03.004.

Tao, L. and Cai, S. (2004) Heave motion suppression of a Spar with a heave plate. *Ocean Engineering,* 31(5), pp. 669–692. DOI: 10.1016/j.oceaneng.2003.05.005.

Tao, L. and Dray, D. (2008) Hydrodynamic performance of solid and porous heave plates. *Ocean Engineering,* 35(10), pp. 1006–1014. DOI: 10.1016/j.oceaneng.2008.03.003.

Tao, L. and Thiagarajan, K. (2003) Low KC flow regimes of oscillating sharp edges. II. Hydrodynamic forces. *Applied Ocean Research,* 25(2), pp. 53–62. DOI: [10.1016/S0141-1187(03)00046-4](10.1016/S0141-1187(03)00046-4).

The MathWorks Inc. (2016) MATLAB R2016b (version 9.1.0.441655).

Tracy, C. H. (2007) *Parametric design of floating wind turbines.* Master thesis. Massachusetts Institute of Technology. Available at: https://dspace.mit.edu/handle/1721.1/40877 (accessed: 01/29/2020).

Vangdal, C. (2019) *Hydrodynamic Study of Floating Wind Turbines in Extreme Conditions.* Master thesis. Department of Marine Technology, NTNU. Available at: https://ntnuopen.ntnu.no/ntnu-xmlui/handle/11250/2622977 (accessed: 03/25/2020).

Veselina Petrova (Nov. 18, 2019) *French floating offshore wind farm to use 10-MW MHI Vestas hardware.* Available at: https://renewablesnow.com/news/french-floating-offshore-wind-farm-to-use-10-mw-mhi-vestas-hardware-676738/ (accessed: 06/07/2020).

Wadhwa, H. and Thiagarajan, K. P. (2009) Experimental Assessment of Hydrodynamic Coefficients of Disks Oscillating Near a Free Surface. *ASME 2009 28th International Conference on Ocean, Offshore and Arctic Engineering.* Honolulu, Hawaii, USA, May 31–June 5, 2009. Vol. 4: Ocean Engineering; Ocean Renewable Energy; Ocean Space Utilization, Parts A and B. ASME, pp. 435–441. DOI: 10.1115/omae2009-79671.

Wang, Q. (2014) *Design and Dynamic Analysis of a Steel Pontoon-type Semi-submersible Floater Supporting the DTU 10MW Reference Turbine.* Master thesis. Department of Marine Technology, NTNU. Available at: https://ntnuopen.ntnu.no/ntnu-xmlui/handle/11250/2400733 (accessed: 05/20/2020).

Yu, W., Müller, K., and Lemmer, F. (2018) *D4.2 Public Definition of the Two LIFES50+ 10MW Floater Concepts.* Available at: https://lifes50plus.eu/wp-content/uploads/2018/04/GA_640741_LIFES50_D4.2.pdf (accessed: 02/04/2020).

A   Upscaled Design
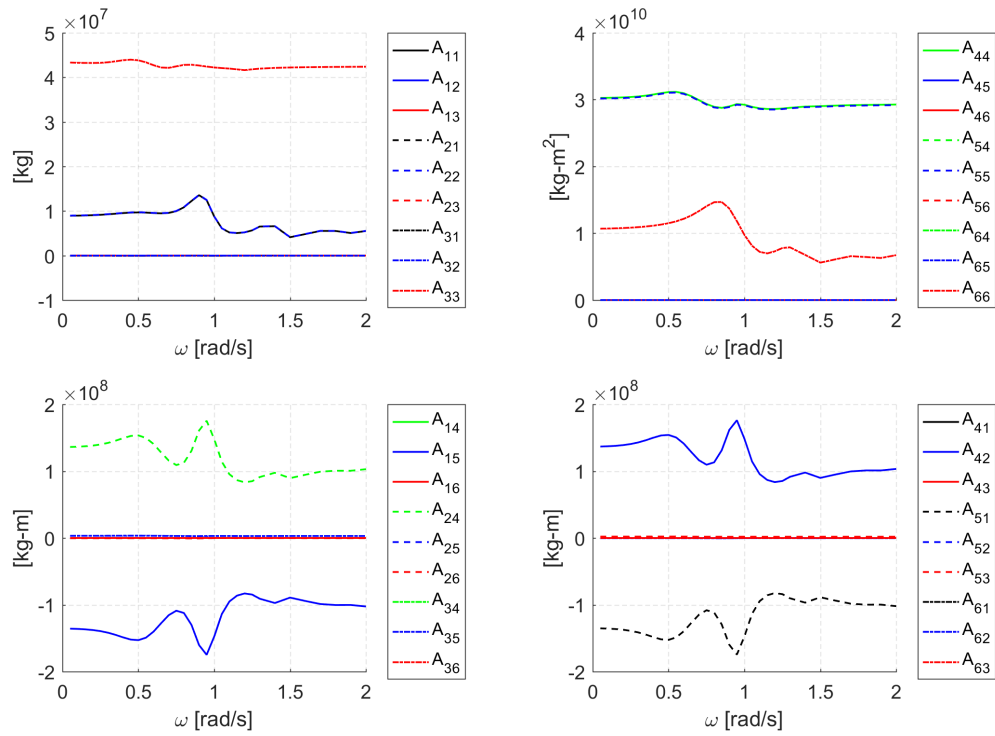
Figure A.1: Added mass coefficients from *Wadam* for the upscaled 10 MW platform.
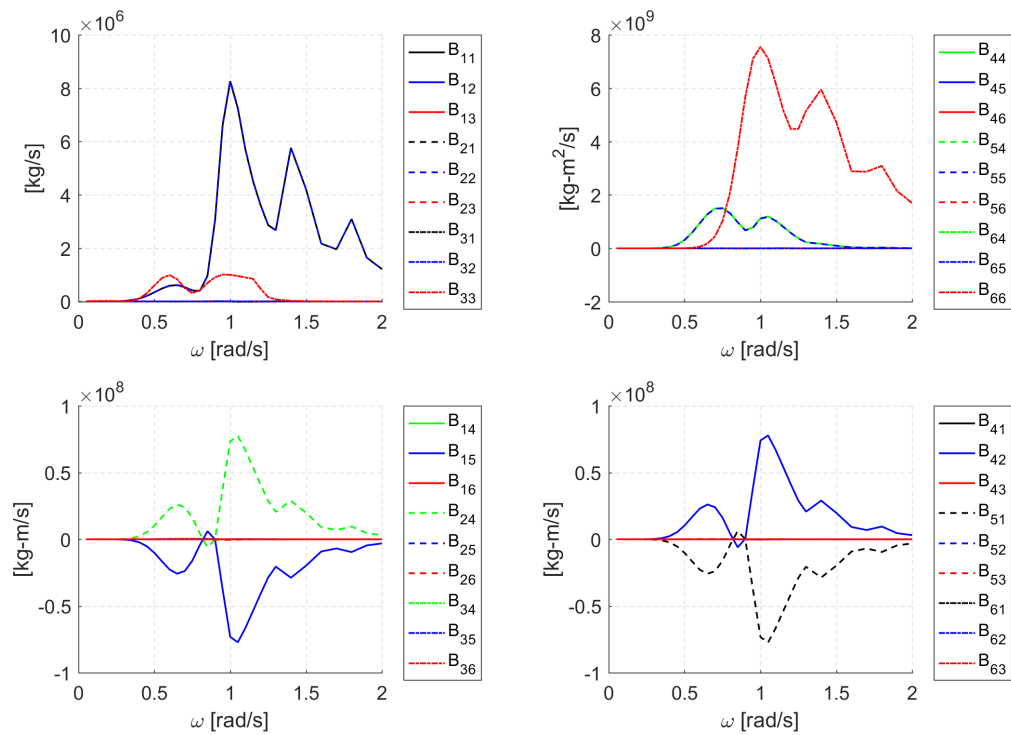
Figure A.2: Potential damping coefficients from *Wadam* for the upscaled 10 MW platform.
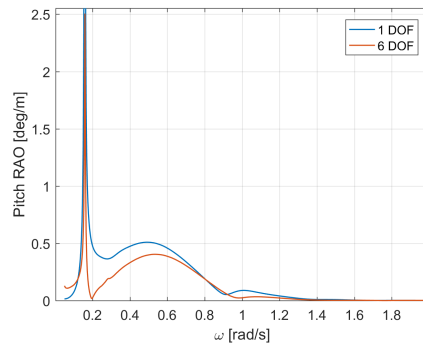
Figure A.3: The pitch RAO when solved with the one DOF and six DOF equations of motions.

B Parameter Variation

This appendix complements Section 5.2 and Section 5.4 with additional figures from the parameter variations to further explain the results. The appendix is divided into five sections, one for each of the parameters adjusted. These are: 1) column diameter, 2) draft, 3) distance between columns, 4) length of heave plates, and 5) mean tilt angle.

B.1 Column Diameter
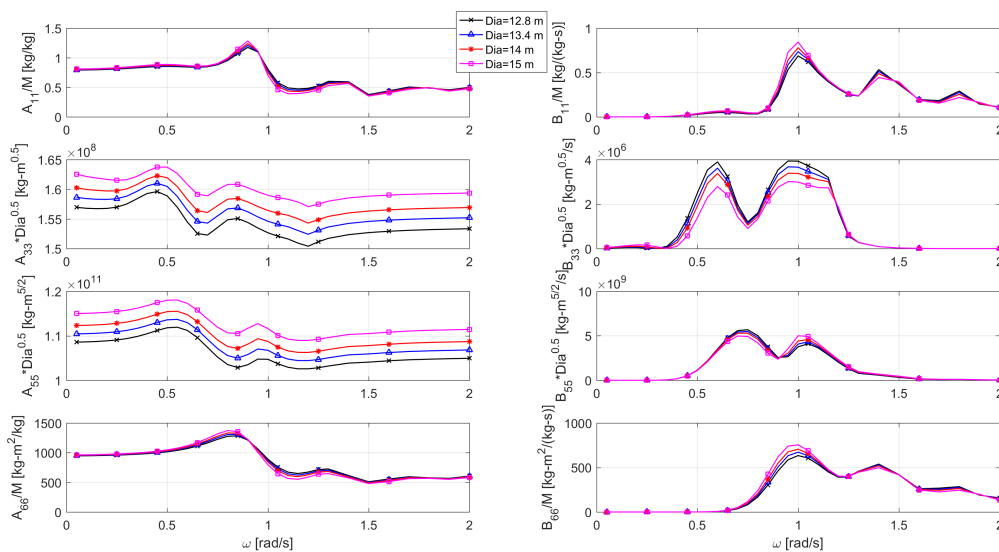
Figure B.1: Normalized added mass and damping in surge, heave, pitch, and yaw for different column diameters. The surge and yaw coefficients are divided by the displaced mass of the structure, while the heave and pitch coefficients are multiplied by the square root of the column diameter.
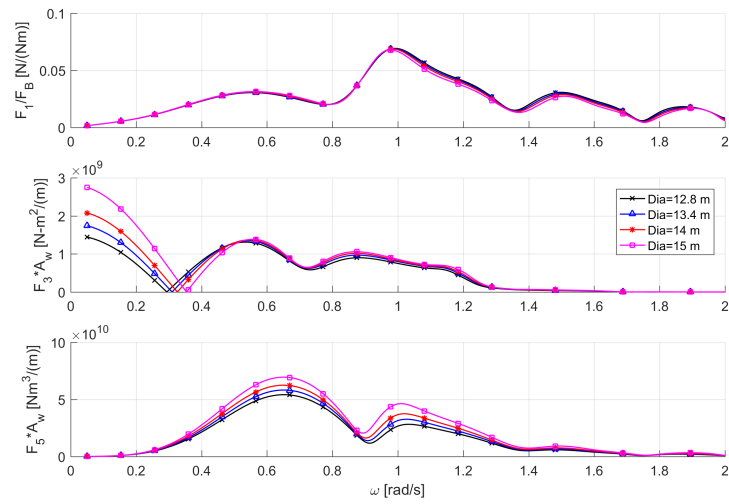
Figure B.2: Normalized wave excitation loads in surge, heave, and pitch for different column diameters. The surge force is divided by the buoyancy force and the heave and pitch loads are multiplied by the waterplane area.
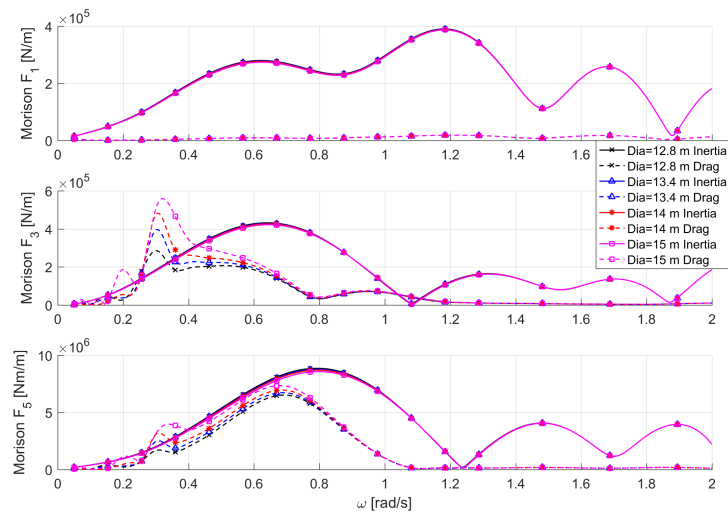
Figure B.3: Morison wave loads plotted for different column diameters.
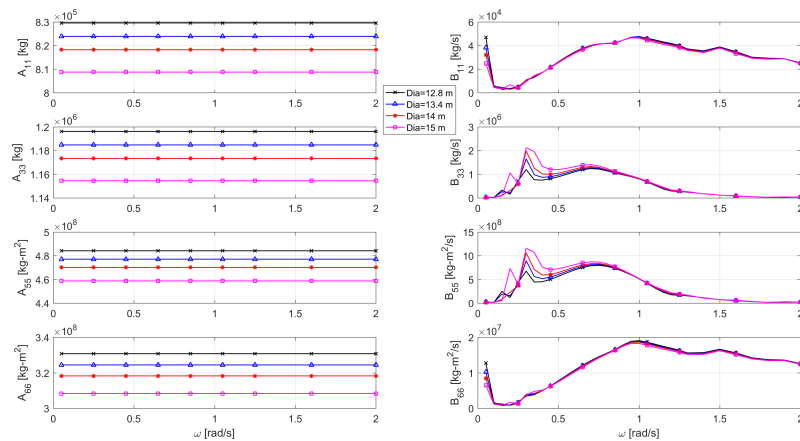
Figure B.4: Morison added mass and linearized viscous damping plotted for different column diameters.
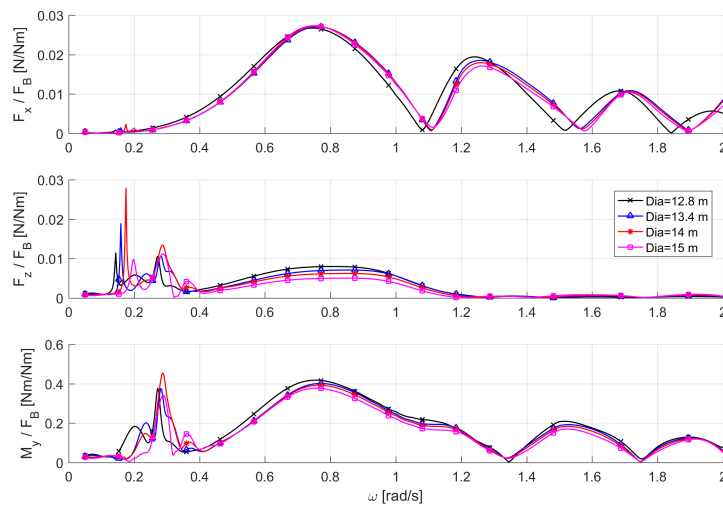
Figure B.5: Normalized internal forces in x and z, and bending moment in cross section for different column diameters. The forces and moment are divided by the buoyancy force of the entire structure.

            (a) Dia=12.8 m.   **(b)** Dia=15 m.
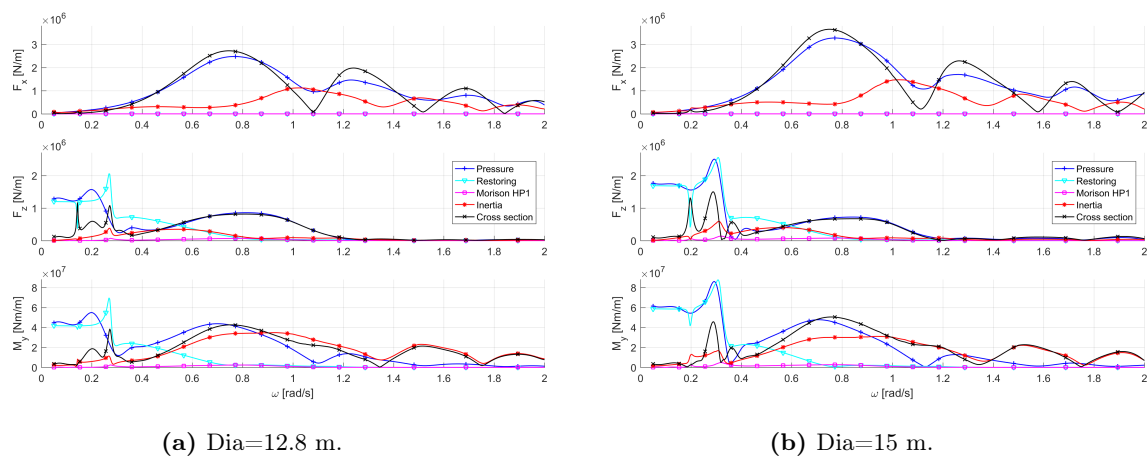
Figure B.6: Internal forces and bending moments in cross section for column diameter equal to 12.8 and 15 meters.

B.2   Draft
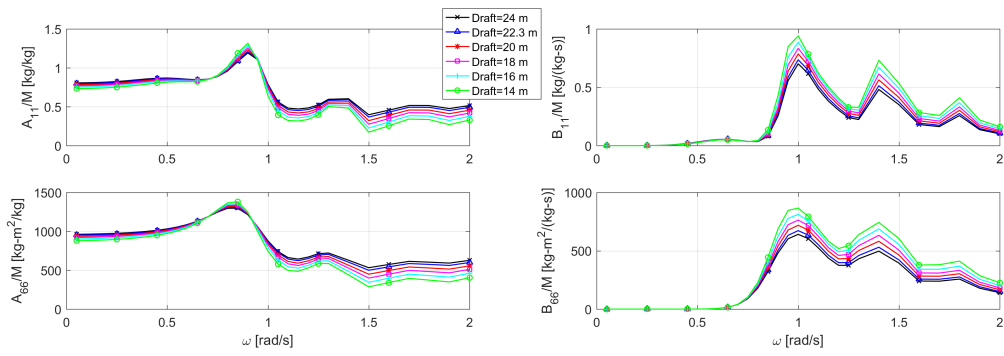
Figure B.7: Normalized added mass and damping in surge and yaw for different drafts. The coefficients are divided by the displaced mass of the structure.
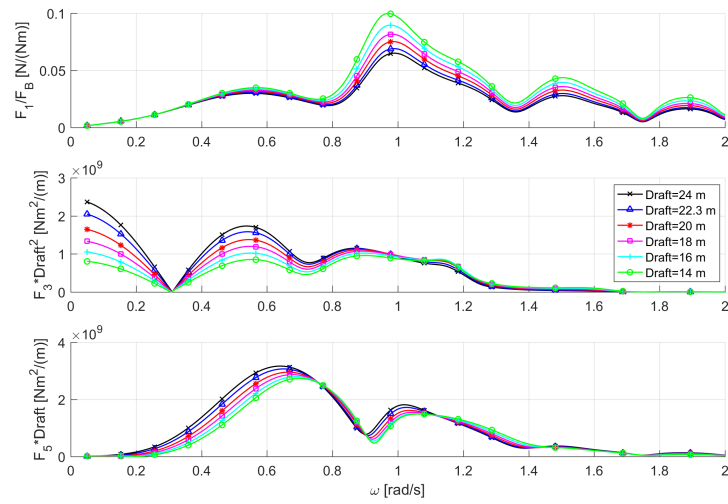
Figure B.8: Normalized wave excitation loads in surge, heave, and pitch for different drafts. The surge force is divided by the buoyancy force, the heave force is multiplied by the draft squared, and the pitch moment is multiplied by the draft.
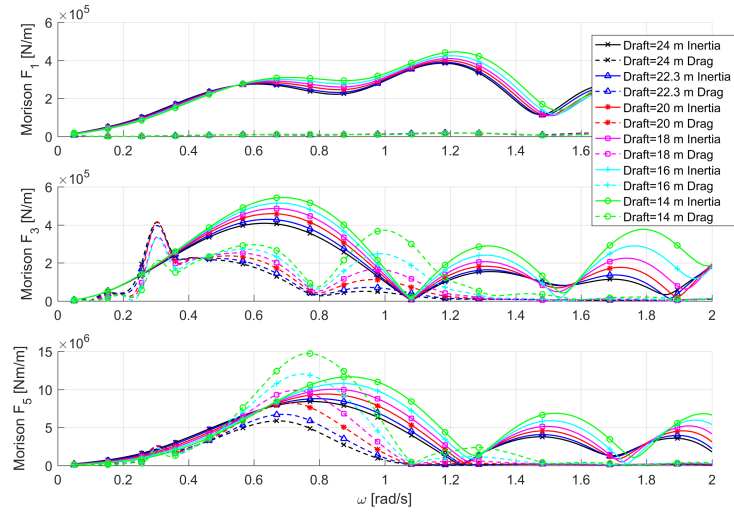
Figure B.9: Morison wave loads plotted for different drafts.
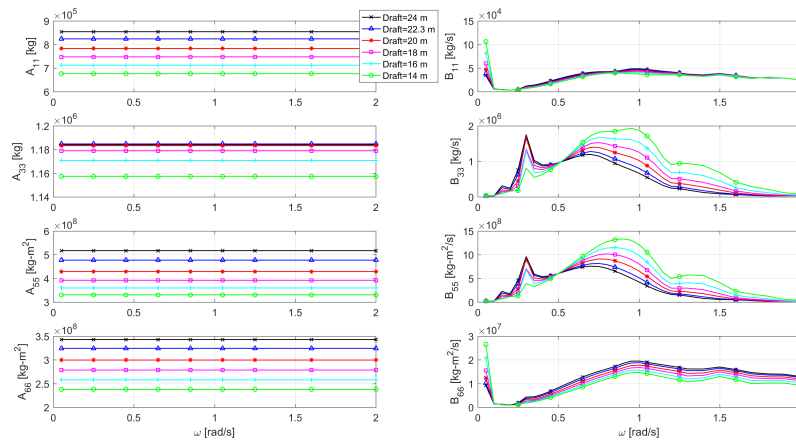
Figure B.10: Morison added mass and linearized viscous damping plotted for different drafts.

(a) Draft=14 m.

(b) Draft=24 m.
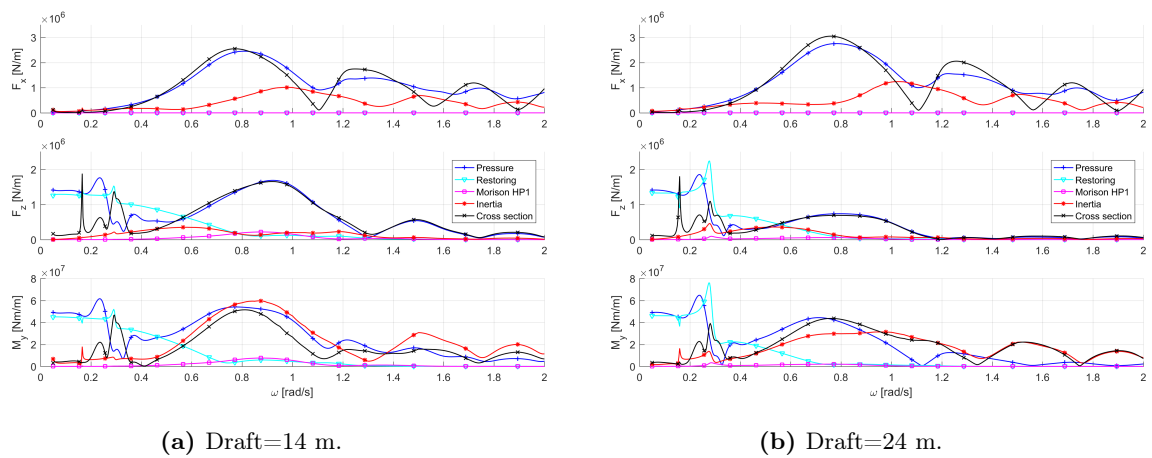
Figure B.11: Internal forces and bending moments in cross section for drafts equal to 14 and 24 meters.

B.3   Distance between Columns
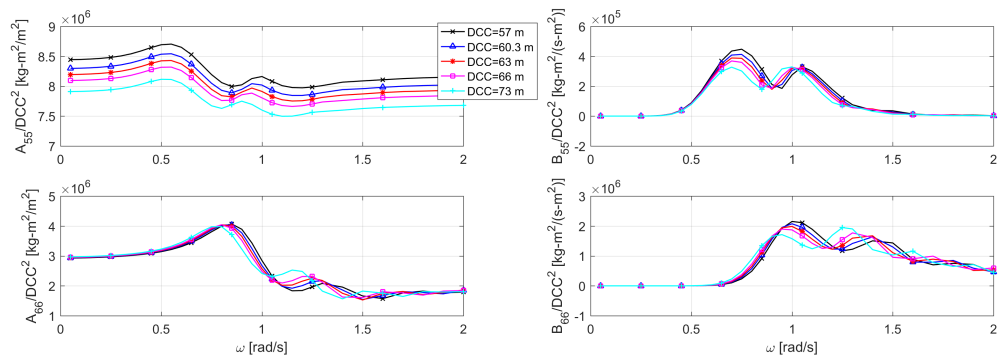
Figure B.12: Added mass and damping in pitch and yaw for different DCC. The coefficients are divided by DCC squared.
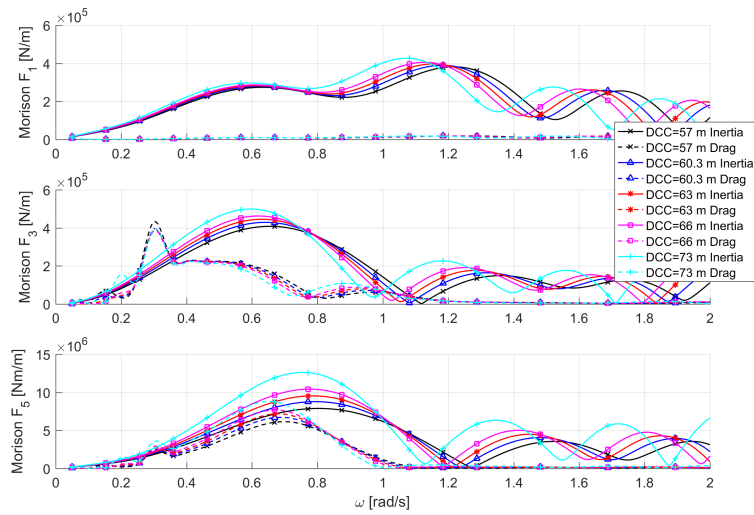
Figure B.13: Morison wave loads plotted for different DCC.
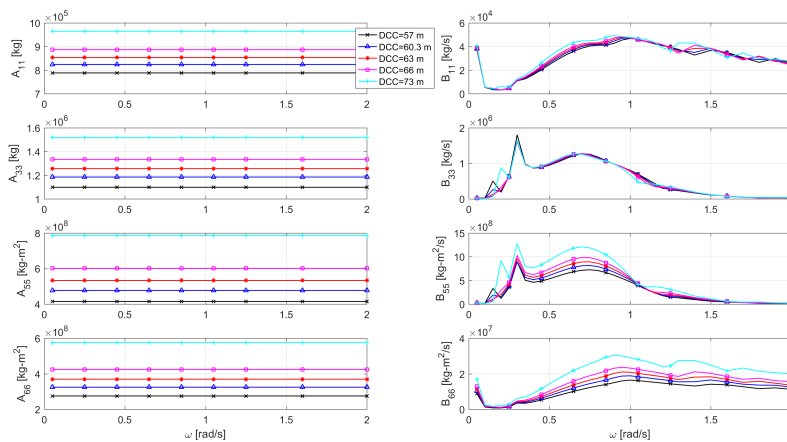
Figure B.14: Morison added mass and linearized viscous damping plotted for different DCC.

(a) DCC=57 m.

(b) DCC=73 m.
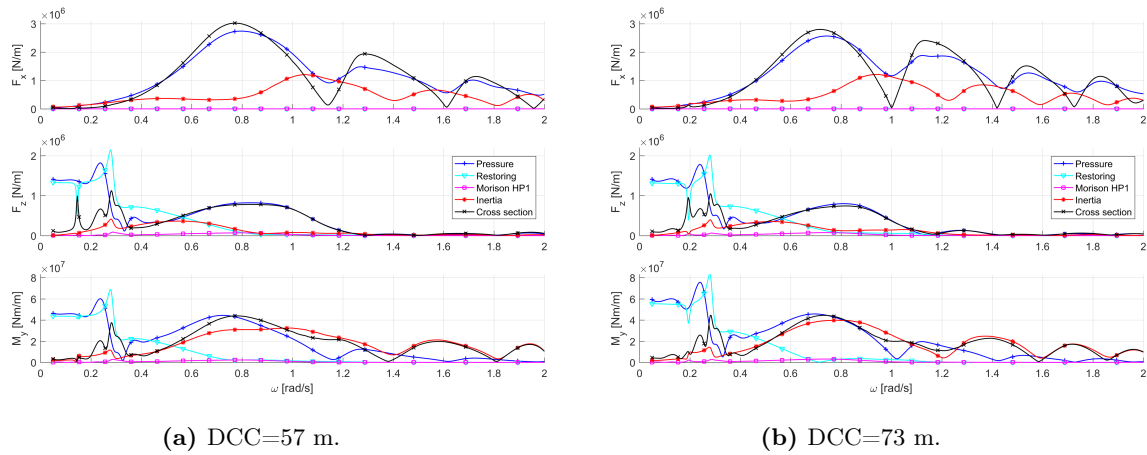
Figure B.15: Internal forces and bending moment in cross section for DCC equal to 57 and 73 meters.

B.4   Length of Heave Plates
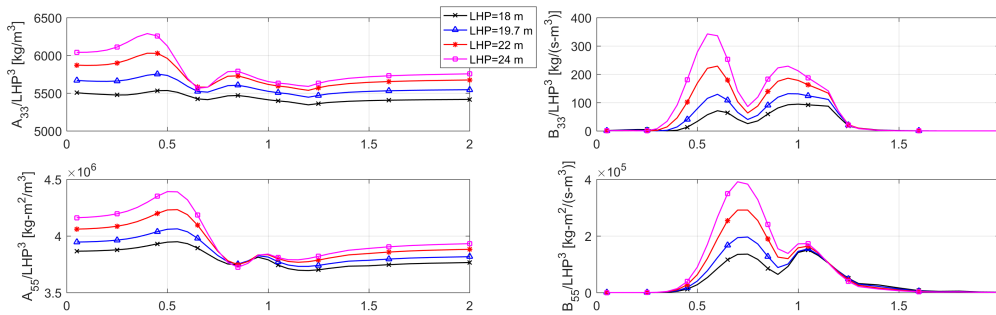
Figure B.16: Normalized added mass and damping in heave and pitch for different LHP. The coefficients are divided by the cube of LHP.
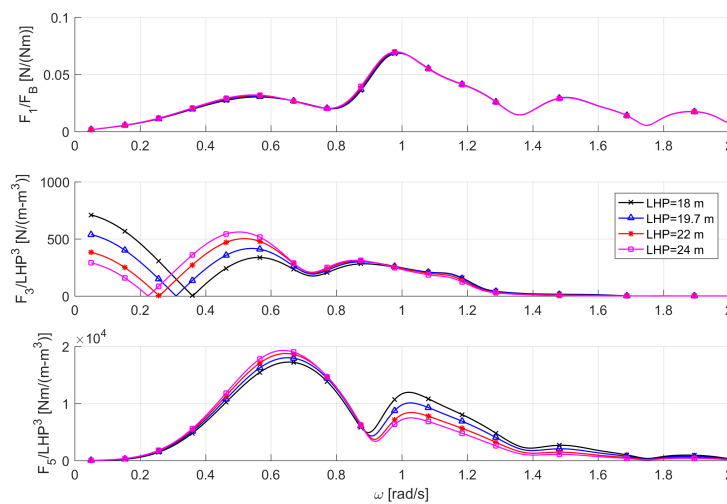
Figure B.17: Normalized wave excitation forces in surge, heave, and pitch for different LHP. The surge force is divided by the buoyancy force, the heave and pitch loads are divided by the cube of the heave plate edge length (LHP).
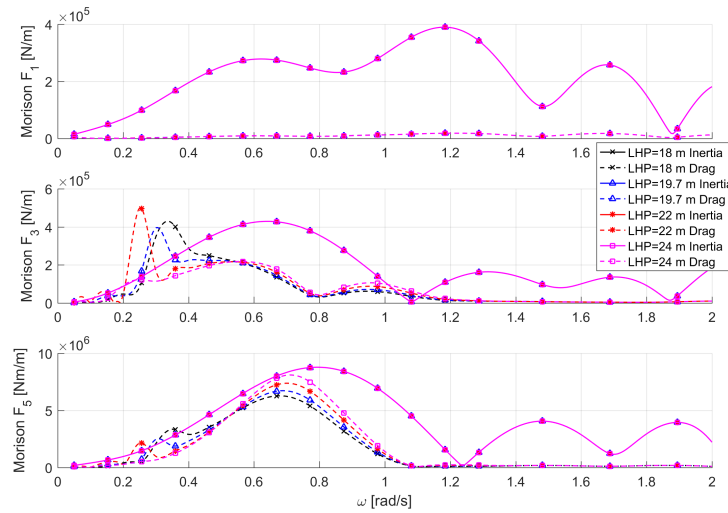
Figure B.18: Morison wave loads plotted for different LHP.
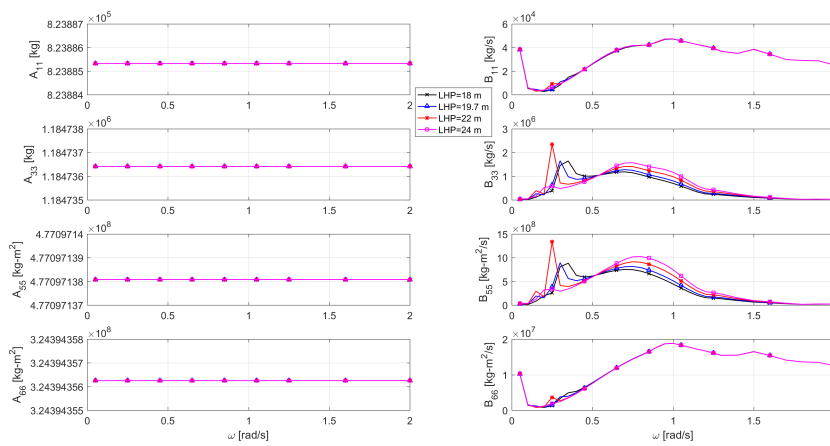
Figure B.19: Morison added mass and linearized viscous damping plotted for different LHP.
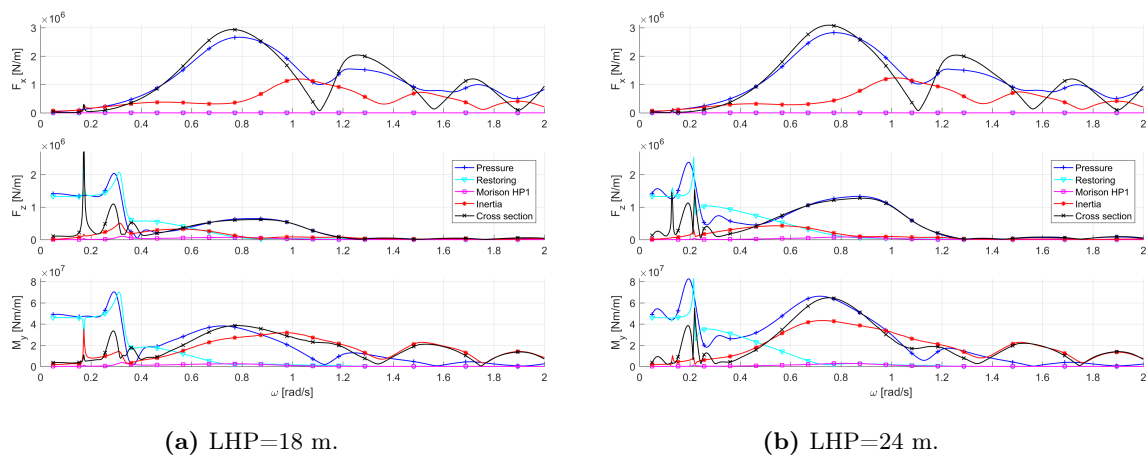
(a) LHP=18 m.   **(b)** LHP=24 m.

Figure B.20: Internal forces and bending moment in cross section for LHP equal to 18 and 24 meters.

B.5   Mean Tilt Angle
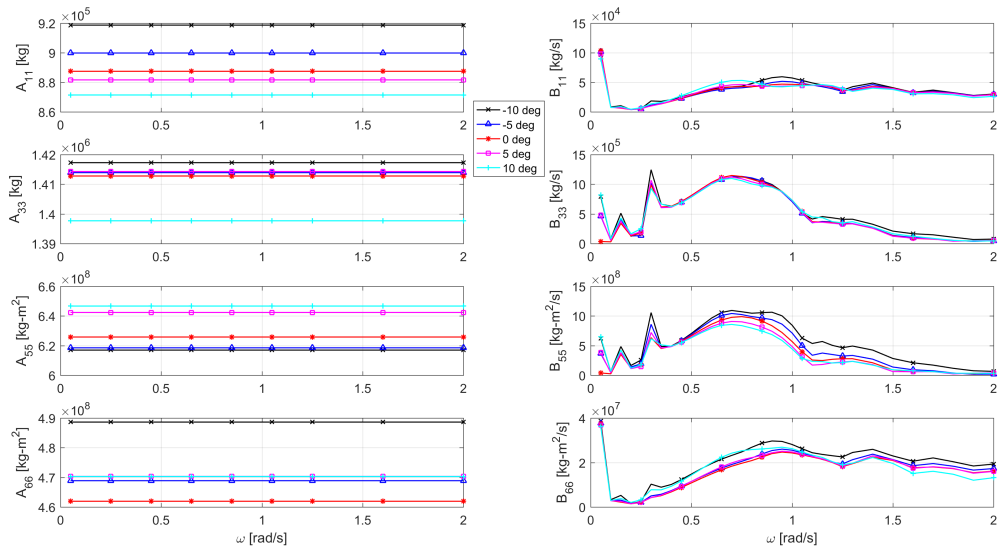
Figure B.21: Morison added mass and linearized viscous damping plotted for different tilt angles.
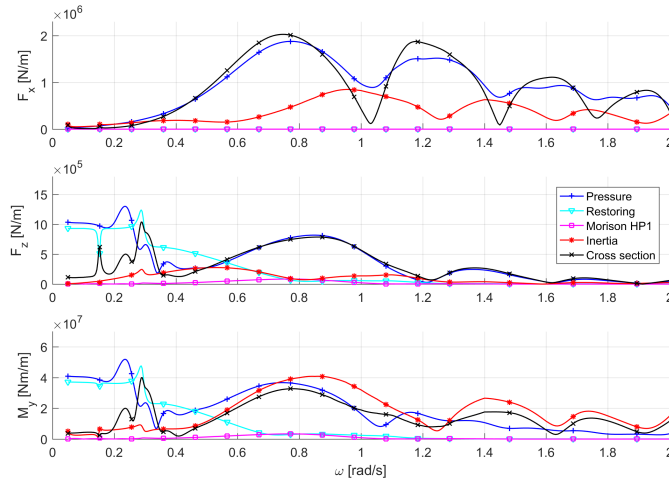
(a) 0 degrees.
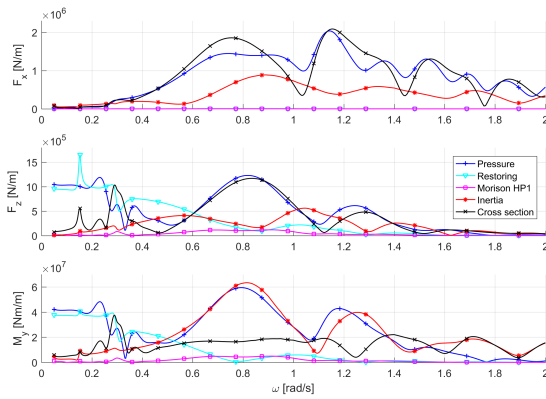
(b) -10 degrees.
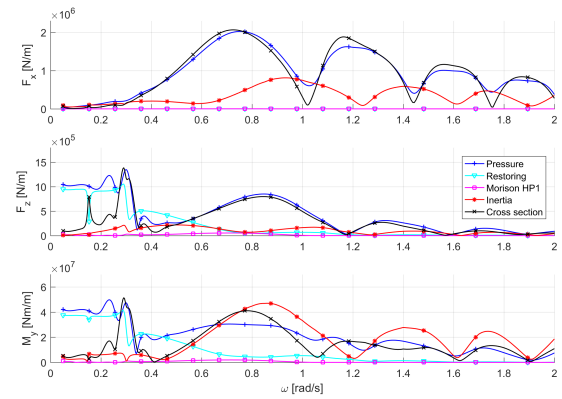
(c) 10 degrees.

Figure B.22: Internal forces and bending moment in cross section for a zero and ±10 degrees tilt angle. All the calculations are for the improved design.

C   Estimation of Heave Excitation Force

The heave excitation force on the WindFloat hull is estimated based on the procedure explained by Greco (2012) for a standard drilling semi-submersible in beam sea. For the estimation, the truss members are neglected and the waves propagate in the positive x-direction.

Assumptions:

- Linear potential-flow theory. Regular waves propagating in positive x-direction, $\beta = 0$.

- Deep water, $\omega^2 = kg$.

- Long wave approximation, $\lambda > 5D$.

- Steady-state conditions.

- Coupling effects are neglected.

Based on the two first assumptions, the incident wave velocity potential, ϕ_0, dynamic pressure, p_0, and vertical acceleration of the wave particles, $a_{0,3}$ are given as,

$$\phi_0 = i\frac{g\zeta_a}{\omega}e^{kz}e^{-ik(x\cos\beta + y\sin\beta)}e^{i\omega t}, \tag{C.1}$$

$$p_0 = -\rho\frac{\partial\phi}{\partial t} = \rho g\zeta_a e^{kz}e^{i(\omega t - kx)}, \tag{C.2}$$

$$a_{0,3} = \frac{\partial^2\phi}{\partial t\partial z} = -\omega^2\zeta_a e^{kz}e^{i(\omega t - kx)}. \tag{C.3}$$

The heave excitation force consists of the Froude-Kriloff force and the diffraction force, and the forces in heave direction are connected to the heave plates. In the following equations, the subscript $_B$ means bottom of the heave plates, the subscript $_T$ means top of the heave plates, the subscript $_m$ means middle of the heave plates, the subscript $_{HP}$ means the heave plates, and the subscript $_{col}$ means the columns. The areas, A, are the cross-section areas in the xy-plane.

The Froude-Kriloff force on a heave plate is calculated by assuming a constant pressure on the heave plates since long waves are assumed. The pressure and the force on the bottom of the heave plate i is

$$p_{0,B} = \rho g\zeta_a e^{kz_B}e^{i(\omega t - kx_i)} \Rightarrow F_{FK,B} = p_{0,B}A_{HP}. \tag{C.4}$$

The pressure and the force on the top of the heave plate i is

$$p_{0,T} = \rho g\zeta_a e^{kz_T}e^{i(\omega t - kx_i)} \Rightarrow F_{FK,T} = -p_{0,B}(A_{HP} - A_{col}). \tag{C.5}$$

The total vertical Froude-Kriloff force acting on the heave plate is then,

$$F_{FK,3} = F_{FK,B} + F_{FK,T} = \rho g\zeta_a(e^{kz_B} - e^{kz_T})e^{i(\omega t - kx_i)}A_{HP} + \rho g\zeta_a e^{kz_T}e^{i(\omega t - kx_i)}A_{col}. \tag{C.6}$$

Further, $z_B = z_m - h/2$, where h is the thickness of the heave plate. Using Taylor expansion on $e^{kh/2}$ and that $kh << 1$ gives,

$$e^{kz_B} = e^{kz_m - kh/2} \approx e^{kz_m} - \frac{kh}{2}e^{kz_m} \tag{C.7}$$

Similar can be done for e^{kz_T} resulting in the Froude-Kriloff force on one heave plate could be written as,

$$F_{FK,3} \approx -\rho g \zeta_a k e^{kz_m} e^{i(\omega t - kx_i)} \overbrace{A_{HP} h}^{V_{HP}} + \rho g \zeta_a e^{kz_T} e^{i(\omega t - kx_i)} A_{col} \tag{C.8}$$
$$= \rho g \zeta_a e^{kz_m} e^{i(\omega t - kx_i)} (e^{k(z_T - z_m)} A_{col} - k V_{HP}).$$

Using Taylor expansion on $e^{k(z_t - z_m)}$ and knowing that $k(z_t - z_m) << 1$. The total Froude-Kriloff force on the three heave plates could be written as,

$$F_{FK,3} = \zeta_a e^{kz_m} (\rho g A_{col} + \rho g k(z_T - z_m) A_{col} - \rho g k V_{HP})(2e^{i(\omega t - kx_{col2})} + e^{i(\omega t - kx_{col1})})$$
$$= \zeta_a e^{kz_m} (\rho g A_{col} - \rho \omega^2 z_m A_{col} + \underbrace{\rho \omega^2 z_T A_{col} - \rho \omega^2 V_{HP}}_{-\omega^2 \rho V_{col+HP} = -\omega^2 \frac{1}{3} M})(2e^{i(\omega t - kx_{col2})} + e^{i(\omega t - kx_{col1})}). \tag{C.9}$$

The diffraction force could be calculated using the added mass and damping terms since long waves are assumed. Further, the damping could be neglected in long waves and in heave the added mass comes from the three heave plates. So the diffraction force on the structure could be calculated as,

$$F_{D,3} = \frac{2}{3} A_{33} a_{0,3}(x = x_{col2}) + \frac{1}{3} A_{33} a_{0,3}(x = x_{col1})$$
$$= -\omega^2 \zeta_a e^{kz_m} \frac{1}{3} A_{33}(2e^{i(\omega t - kx_{col2})} + e^{i(\omega t - kx_{col1})}). \tag{C.10}$$

The total heave excitation force could then be estimated as,

$$F_{exc,3} = F_{FK,3} + F_{D,3}$$
$$= \zeta_a e^{kz_m}[\rho g A_{col} - \rho \omega^2 z_m A_{col} - \omega^2 \frac{1}{3}(M + A_{33})](2e^{i(\omega t - kx_{col2})} + e^{i(\omega t - kx_{col1})}). \tag{C.11}$$

From the equation, the heave excitation force will be zero when the expression in the brackets is zero. Solving this equation and using that,

$$\omega_{n,3}^2 = \frac{C_{33}}{M + A_{33}} = \frac{\rho g 3 A_{col}}{M + A_{33}}, \tag{C.12}$$

gives that the heave excitation force will be zero for,

$$\omega_c = \frac{\omega_{n,3}}{\sqrt{1 - \frac{|z_m|}{g} \omega_{n,3}^2}}, \tag{C.13}$$

where ω_c is called the cancellation frequency and is connected to the force on the top and bottom of each heave plate cancel each other. It is observed that $\omega_c > \omega_{n,3}$ always. Compared to the semi-submersible in the example by Greco (2012), there will not be cancellation effects due to

the phase difference between the columns since the WindFloat hull is not symmetric about the y-axis. However, the absolute value of expression in the last parenthesis will alternate between one and three. For low wave frequencies it will be close to three. When the wave length is twice the distance between the columns, $\lambda = 2(x_{col1} - x_{col2})$, the expression in the last parenthesis will be one.

D MATLAB Codes

The most important *MATLAB* codes used for the calculations are given in this section.

D.1 Main script

```matlab
% Upscaled WindFloat 10 MW structure
% Written by Vetle Kallaak
clear variables; close all;

% Environment
env.rho = 1025; % Sea water density
env.g = 9.80665; % Gravity
env.d = 320; % Depth [m]
env.amp = 1; % Wave amplitude [m]
env.beta = 0; % Wave heading angle [rad]
% Parameters
p.FB1 = 10; % Column freeboard
% Wind turbine
[p.WT] = WTdata(p.FB1);

p.numCol = 3; % Number of columns
p.draft = 20; % Floater draft
p.diaCol = 11.5; % Column diameter
p.dcc = 68.5; % Center-center distance for columns
p.lhp = 17.5; % Heave plate length of plate edge (hexagon)
p.diaBeam = 2.8; % Truss main beam diameter
p.diaBracing = 2.0; % Truss bracing diameter

% Unknown variables, guessed
p.COGz_pon = -p.draft+p.diaBeam; % Mean position of pontoons
p.COGz_beam = p.FB1 - p.diaBeam; % Mean position of bracing
p.hhp = 0.05; % Height of heave plate (Kvittem)
p.hhpM = 0.4; % Height of heave plates modeled in GeniE
p.FBM = 1; % Modeled freeboard in GeniE
p.massFracSteel = 0.20; % Steel mass, fraction of total mass (From Erin)
p.t = 0.03; % Steel plates thickness
p.thp = 0.05; % Heave plate thickness

% Adjustable ballast for right output
p.massFracBallast1 = 0.18;
p.rhoB = env.rho; % Density of ballast
p.COGz_ballastBot = -p.draft + p.hhp + p.t; % Ballast floor

p.tilt = 0 * pi/180; % Pitch tilt angle

% GeniE mesh, depend a bit on wave freq and dimensions
mesh.gensize = 1.4; % General mesh element size
mesh.maxsize = 2.2; % Max mesh size, for under hp

% Calculate RAO and Morison forces
sesam.workspace = '10Mw_opti1';
newrun = false;

% Criteria
crit.eta5max = (10*pi/180); % Max allowable pitch angle
crit.T33min = 20; % Min natural period in heave
crit.DhpDcmin = 1.6; % Min diameter ratio, hp/column

% Wave frequencies
w1 = 0.05:0.05:1.3;
w2 = 1.4:0.1:2;

% HydroD workspaces
sesam.wadam1 = [sesam.workspace '\WadamRun1'];
sesam.wadam2 = [sesam.workspace '\WadamRun2']; % Extra damping
WaveHeadInd = 1; % Index of the wave heading for which to calc everything
figPosition = [100 100 1000 650];

interpolPoints = 16;

%% Hydrostatic calculations and structure proporties
[M, C, elem, alpha, mdata] = hydrostatic(env, p);
```

```matlab
68  mdata
69  C(1,1) = p.WT.Ft/(0.15*env.d); % Mooring stiffness
70
71  %% Wave environment
72  % Waves
73  clear waves
74  waves(:,1) = [w1 w2];
75  waves(:,2) = 2*pi./waves(:,1);
76  waves(:,3) = 2*pi*env.g./waves(:,1).^2;
77  maxElemSize = min(waves(:,3))/6 % Max element diagonal
78
79  %% Control of input parameters
80  [T33, A33, check] = control(env,p,elem,alpha,C,mdata,crit);
81  choice = menu('Continue?','Yes','No');
82  if choice == 2 || choice == 0
83      return;
84  end
85
86  %% Sesam
87  mesh.numElWL2 = ceil(pi*p.diaCol/mesh.gensize); % Elemenents on WL column 2
88  if newrun
89      Bex = zeros(6,6);
90      check = writeSesamFiles(sesam, p, mesh, env, waves, C, mdata, Bex, 1);
91      if check
92          cont = runSesam(p, sesam, 1); % WadamRun 1
93          if ~cont % Continue
94              return;
95          end
96      end
97  end
98
99  %% Read Wadam.LIS file, results from Wadam
100 % Read results from Wadam
101 [MASS, RESTORING, DAMPING, ADDMASS, WAVEEX, MOTIONS, WaveDat, WaveDir] = ...
102     WadamLIS(sesam.wadam1);
103 % Rewrite potential excitation force and RAO from Wadam file
104 for i=1:length(WaveDat(:,1))
105     F_pot(1:6,i) = complex(WAVEEX(:,1,WaveHeadInd,i),WAVEEX(:,2,WaveHeadInd,i));
106     etaW(1:6,i) = complex(MOTIONS(:,1,WaveHeadInd,i),MOTIONS(:,2,WaveHeadInd,i));
107 end
108 waveW(1,:) = WaveDat(:,5); % Wave frequencies
109
110 %% Loads on Morison elements
111 [etaM1, etaM0, FtotwI, FtotwD, Atot_mor, Btot_mor, F_hp1, B_hp1] = ...
112 includeMorisonElem(p, elem, alpha, env, M, C,...
113 waveW, ADDMASS, DAMPING, F_pot);
114
115 %% Calculate RAOs
116 % Calculate RAO, solving the 6DOF equation of motion with Wadam results
117 [etaWown] = calcRAO(WaveDat(:,5), MASS, ADDMASS, DAMPING, RESTORING, F_pot);
118 % Interpolate values for better solution
119 % Linear interpolation of A and B matrices
120 [A_pothr] = linInterpolation(ADDMASS, 3, interpolPoints);
121 [B_pothr] = linInterpolation(DAMPING, 3, interpolPoints);
122 [Btot_morhr] = linInterpolation(Btot_mor, 3, interpolPoints);
123 [B_hp1hr] = linInterpolation(B_hp1, 3, interpolPoints);
124
125 waveWhr = linInterpolation(waveW, 2, interpolPoints);
126 % Spline interpolation of forces for better fit
127 for r = 1:6 % Splining
128     F_pothr(r,:) = interp1(waveW,F_pot(r,:),waveWhr,'spline');
129     F_totwIhr(r,:) = interp1(waveW,FtotwI(r,:),waveWhr,'spline');
130     F_totwDhr(r,:) = interp1(waveW,FtotwD(r,:),waveWhr,'spline');
131     F_hp1hr(r,:) = interp1(waveW,F_hp1(r,:),waveWhr,'spline');
132 end
133 Atot = A_pothr + Atot_mor; % Total added mass matrix for structure
134 Btot = B_pothr + Btot_morhr; % Total damping for structure
135 Ftot = F_pothr + F_totwIhr + F_totwDhr; % Total excitation loads
136 % RAO from wadam with interpolated values
137 [etaWhr] = calcRAO(waveWhr, MASS, A_pothr, B_pothr, RESTORING, F_pothr);
138 % Final RAO
139 [eta1] = calcRAO(waveWhr, M, Atot, Btot, C, Ftot);
140
```

```matlab
141  %% Natural frequencies
142  for dof=1:6 %dof
143      Tn_all(:,1) = 2*pi*sqrt((M(dof,dof)+Atot(dof,dof,:))/(C(dof,dof)));
144      Tn_all(:,2) = 2*pi./waveWhr(:);
145      [~, waven_index(dof)] = min(abs(Tn_all(:,1) - Tn_all(:,2)));
146      Tn(dof,1) = Tn_all(waven_index(dof),1); % Natural period
147      Tn(dof,2) = 2*pi/Tn(dof,1); % Natural frequency
148  end
149  Tn
150  waven_index
151
152  %% Additional damping to HydroD
153  % For calculating more correct motions, read pressure panels, get more
154  % correct radiation pressure
155  if newrun
156      Bex = Btot_morhr(:,:,waven_index(3))
157      check = writeSesamFiles(sesam, p, mesh, env, waves, C, mdata, Bex, 2);
158      if check
159          cont = runSesam(p, sesam, 2); % WadamRun 2
160      end
161  end
162  % Read results from Wadam
163  [MASS1, RESTORING1, DAMPING1, ADDMASS1, WAVEEX1, MOTIONS1, WaveDat1, WaveDir1] = ...
164      WadamLIS(sesam.wadam2);
165  % Rewrite potential excitation force and RAO from Wadam file
166  for i=1:length(WaveDat1(:,1))
167      etaW_Bex(1:6,i) = complex(MOTIONS1(:,1,WaveHeadInd,i),MOTIONS1(:,2,WaveHeadInd,i));
168  end
169  [etaW_Bexown] = calcRAO(WaveDat1(:,5), MASS1, ADDMASS1, DAMPING1, RESTORING1, F_pot);
170
171  %% Calculate internal loads at cross section
172  [numElem, Fp, Fc, F_Mhp1, FI, Fcs] = internalLoads(sesam, p, elem, env, waveW, ...
173      waveWhr, F_hp1hr, B_hp1hr, eta1, ADDMASS, DAMPING, etaM1, etaW, etaW_Bex, F_pot);
174
175  %% Save results
176  if newrun
177      %% Save entire workspace
178      clear aa ac bb bc c choice cont dof ee ff i f plotFig r Tn_all
179      save(['C:\Users\Vetle\OneDrive - NTNU\Emner\MASTER\MATLAB\Results\' sesam.workspace])
180  end
181  fprintf('\nFinished!\n\n');
```

D.2   Mass and Hydrostatic Calculations

```matlab
1   % Dimensions, mass and hydrostatic data for WindFloat concept
2   % Written by Vetle Kallaak
3
4   function [M, C, elem, alpha, mdata] = hydrostatic(env,p)
5   rho = env.rho;
6   g = env.g;
7   %% Elements of the structure
8   elem = struct('name',[],'L',[],'A',[],'Vwet',[],'mass',[],'COG',[]);
9   % Columns
10  elem(1).name = 'column';
11  elem(1).L = p.FB1+p.draft-p.hhp;
12  elem(1).A = pi*(p.diaCol/2)^2;
13  elem(1).Vwet = elem(1).A * (p.draft-p.hhp);
14  elem(2:3) = elem(1);
15  Vcol_wetM = elem(1).A * (p.draft-p.hhpM) * p.numCol; % Sesam volume
16  % Heave plates
17  elem(4).name = 'hp';
18  elem(4).L = p.hhp;
19  elem(4).A = (3*sqrt(3)/2 * p.lhp^2);
20  elem(4).Vwet = elem(4).A * elem(4).L;
21  elem(5:6) = elem(4);
22  VhpM = elem(4).A * p.hhpM * p.numCol; % Sesam volume
23  % Beams and pontoons
24  elem(7).name = 'beam';
25  elem(7).L = p.dcc - p.diaCol;
26  elem(7).A = pi*(p.diaBeam/2)^2;
27  elem(7).Vwet = 0;
28  elem(8:12) = elem(7);
29  [elem(10:12).name] = deal('pontoon');
```

```matlab
30  [elem(10:12).Vwet] = deal(elem(10).A * elem(10).L);
31  %% Bracing
32  elem(13).name = 'bracing';
33  alpha = atan((-p.COGz_pon+p.COGz_beam)/(p.dcc/2)) % Angle between pontoon and bracing
34  diaBracHor = p.diaBracing/sin(alpha); % Horizontal cross section, max dia
35  % Corrected alpha
36  alpha = atan((-p.COGz_pon-p.diaBeam/2+p.COGz_beam)/(p.dcc/2-diaBracHor/2))
37  notBracing = p.diaCol/2 / cos(alpha);
38  elem(13).L = sqrt((-p.COGz_pon-p.diaBeam/2+p.COGz_beam)^2 + ...
39      (p.dcc/2-diaBracHor/2)^2)-notBracing;
40  lBracW = (-p.COGz_pon - p.diaBeam/2)/sin(alpha); % Wet length of bracing
41  elem(13).A = pi*(p.diaBracing/2)^2;
42  elem(13).Vwet = elem(13).A * lBracW;
43  elem(14:18) = elem(13); % 6 bracings in total
44
45  %% Volume and mass displacement
46  % GeniE structure
47  mdata.VdispM = Vcol_wetM + VhpM;
48  mdata.massM = mdata.VdispM*rho;
49  % Entire structure
50  VdispTot = sum([elem.Vwet]);
51  massTot = VdispTot*rho;
52  mdata.VdispTot = VdispTot;
53  mdata.massTot = massTot;
54
55  %% Steel mass
56  massSteel = p.massFracSteel * massTot; % Steel mass of hull
57  mdata.massSteel = massSteel;
58  % Volume of steel, for equally distribution of weight
59  VSCol_p = pi*(p.diaCol*p.t-p.t^2)*(p.FB1+p.draft-p.hhp-p.t);
60  VSCol_top = pi*(p.diaCol/2)^2*p.t;
61  VSCol = (VSCol_p + VSCol_top) * p.numCol;
62  VSBeam = pi*(p.diaBeam*p.t-p.t^2)*(p.dcc-p.diaCol)*p.numCol;
63  VSPon = VSBeam;
64  VSBracing = pi*(p.diaBracing*p.t-p.t^2)*elem(13).L*p.numCol*2;
65  VShp = elem(4).A*p.thp*p.numCol;
66  [elem(1:3).mass] = deal(massSteel * VSCol/(VSCol+VSPon+VSBeam+VSBracing+VShp)/p.numCol);
67  [elem(4:6).mass] = deal(massSteel * VShp/(VSCol+VSPon+VSBeam+VSBracing+VShp)/p.numCol);
68  [elem(7:9).mass] = deal(massSteel * VSBeam/(VSCol+VSPon+VSBeam+VSBracing+VShp)/p.numCol);
69  [elem(10:12).mass] = deal(massSteel * ...
70      VSPon/(VSCol+VSPon+VSBeam+VSBracing+VShp) / p.numCol);
71  [elem(13:18).mass] = deal(massSteel * ...
72      VSBracing/(VSCol+VSPon+VSBeam+VSBracing+VShp) / (2*p.numCol));
73
74  %% Ballast and WT mass
75  elem(19).name = 'ballast1';
76  elem(20).name = 'ballast2';
77  massBallast = massTot-massSteel-p.WT.masstot; % Total req. ballast
78  massFracBallast2 = (1-p.massFracBallast1)/2;
79  mdata.massBallast = massBallast;
80  elem(19).Vwet = 0;
81  elem(19).mass = massBallast*p.massFracBallast1;
82  elem(20).Vwet = 0;
83  elem(20).mass = massBallast*massFracBallast2;
84  % Height of ballast
85  elem(19).L = ((elem(19).mass / p.rhoB) / (pi*(p.diaCol/2-p.t)^2));
86  elem(20).L = ((elem(20).mass / p.rhoB) / (pi*(p.diaCol/2-p.t)^2));
87  elem(21) = elem(20);
88  % Wind turbine
89  elem(22).name = 'WT';
90  elem(22).Vwet = 0;
91  elem(22).mass = p.WT.masstot;
92
93  %% Center of gravity
94  % elem(22).mass=0; % To get data w/o WT (wrong draft etc.)
95  % Columns
96  COGz_col = (VSCol_p*(p.FB1-p.t-(p.FB1+p.draft-p.hhp-p.t)/2)+ ...
97      VSCol_top*(p.FB1-p.t/2))/(VSCol_p+VSCol_top);
98  elem(1).COG = [p.dcc/2/cos(pi/6), 0, COGz_col];
99  elem(2).COG = [-p.dcc/2*tan(pi/6), p.dcc/2, COGz_col];
100 elem(3).COG = [-p.dcc/2*tan(pi/6), -p.dcc/2, COGz_col];
101 % Heave plates
102 elem(4).COG = [p.dcc/2/cos(pi/6), 0, -1*(p.draft-p.hhp/2)];
```

```matlab
103  elem(5).COG = [-p.dcc/2*tan(pi/6), p.dcc/2, -1*(p.draft-p.hhp/2)];
104  elem(6).COG = [-p.dcc/2*tan(pi/6), -p.dcc/2, -1*(p.draft-p.hhp/2)];
105  % Beams
106  elem(7).COG = [(elem(1).COG(1)+elem(2).COG(1))/2, ...
107  (elem(1).COG(2)+elem(2).COG(2))/2, p.COGz_beam];
108  elem(8).COG = [(elem(1).COG(1)+elem(2).COG(1))/2, ...
109      -(elem(1).COG(2)+elem(2).COG(2))/2, p.COGz_beam];
110  elem(9).COG = [elem(2).COG(1), 0, p.COGz_beam];
111  % Pontoons
112  elem(10).COG = [(elem(1).COG(1)+elem(2).COG(1))/2, ...
113      (elem(1).COG(2)+elem(2).COG(2))/2, p.COGz_pon];
114  elem(11).COG = [(elem(1).COG(1)+elem(2).COG(1))/2, ...
115      -(elem(1).COG(2)+elem(2).COG(2))/2, p.COGz_pon];
116  elem(12).COG = [elem(2).COG(1), 0, p.COGz_pon];
117  % Bracing
118  COGz_brac = p.COGz_pon + p.diaBeam/2 + elem(13).L/2*sin(alpha);
119  elem(13).COG = [elem(10).COG(1), elem(10).COG(2), COGz_brac];
120  elem(14).COG = [elem(10).COG(1), elem(10).COG(2), COGz_brac];
121  elem(15).COG = [elem(11).COG(1), elem(11).COG(2), COGz_brac];
122  elem(16).COG = [elem(11).COG(1), elem(11).COG(2), COGz_brac];
123  elem(17).COG = [elem(12).COG(1), elem(12).COG(2), COGz_brac];
124  elem(18).COG = [elem(12).COG(1), elem(12).COG(2), COGz_brac];
125  % Ballast
126  elem(19).COG = [p.dcc/2/cos(pi/6), 0, ...
127      p.COGz_ballastBot + elem(19).L/2];
128  elem(20).COG = [-p.dcc/2*tan(pi/6), p.dcc/2, p.COGz_ballastBot + elem(20).L/2];
129  elem(21).COG = [-p.dcc/2*tan(pi/6), -p.dcc/2, p.COGz_ballastBot + elem(21).L/2];
130  % WT
131  elem(22).COG = [elem(1).COG(1)+p.WT.COGx, elem(1).COG(2)+p.WT.COGy, p.FB1+p.WT.COGz];
132
133  %% Mass matrix data
134  COGmom = zeros(1,3); % Global center of gravity, mass moment
135  L_ij = zeros(1,3); % For specific product of inertia
136  % Local inertia of main contributors
137  I(1) = p.numCol*(elem(1).mass*(0.5*(p.diaCol/2)^2+1/12*elem(1).L^2)...
138      +1/4*elem(4).mass*(elem(4).A/pi));
139  I(2) = I(1);
140  I(3) = p.numCol*(elem(1).mass*(p.diaCol/2)^2+0.5*elem(4).mass*(elem(4).A/pi) ...
141      + 2*elem(7).mass*(0.5*(p.diaBeam/2)^2+elem(7).L^2/12)...
142      + 2*elem(13).mass*elem(13).L^2/12*(sin(pi/2-alpha))^2 );
143  for i = 1:length(elem) % All elements
144     for d=1:3
145        COGmom(d) =  COGmom(d) + elem(i).mass * elem(i).COG(d);
146     end
147     % Parellel axis theorem
148     I(1) = I(1) + elem(i).mass * (elem(i).COG(2)^2+elem(i).COG(3)^2);
149     I(2) = I(2) + elem(i).mass * (elem(i).COG(1)^2+elem(i).COG(3)^2);
150     I(3) = I(3) + elem(i).mass * (elem(i).COG(1)^2+elem(i).COG(2)^2);
151     L_ij(1) = L_ij(1) + elem(i).mass * elem(i).COG(1)*elem(i).COG(2);
152     L_ij(2) = L_ij(2) + elem(i).mass * elem(i).COG(1)*elem(i).COG(3);
153     L_ij(3) = L_ij(3) + elem(i).mass * elem(i).COG(2)*elem(i).COG(3);
154  end
155  mdata.COG = COGmom/massTot;
156  % Radii of gyration, r=(r_xx, r_yy, r_zz)
157  mdata.r = sqrt((1/massTot)*I);
158  % Specific product of inertia, r_ij=(r_xy, r_xz, r_yz)
159  mdata.r_ij = - sqrt((1/massTot)*L_ij) .* sign(L_ij);
160  % Calculate mass matrix
161  [M] = massMat(massTot, mdata.COG, mdata.r, mdata.r_ij);
162
163  %% Hydrostatic restoring data
164  % Center of buoyancy
165  COB=zeros(1,3);
166  for i=1:length(elem)
167      COB(1) = COB(1) + elem(i).Vwet*elem(i).COG(1);
168      COB(2) = COB(2) + elem(i).Vwet*elem(i).COG(2);
169      if i<=3 % Columns
170          COB(3) = COB(3) + elem(i).Vwet*(-p.draft+p.hhp)/2;
171      elseif i >= 13 % Bracing
172          COB(3) = COB(3) + elem(i).Vwet*((p.COGz_pon+p.diaBeam/2)/2);
173      else
174          COB(3) = COB(3) + elem(i).Vwet*elem(i).COG(3);
175      end
```

```
176 | end
177 | COB = COB/VdispTot;
178 | mdata.COB = COB;
179 |
180 | % Waterplane inertia
181 | Icol = pi*p.diaCol^4/64;
182 | Iwp(1) = p.numCol*Icol + 2*elem(2).COG(2)^2*elem(2).A + ...
183 |     elem(1).COG(2)^2*elem(1).A + pi*p.diaBracing^2/(4*sin(alpha))*2* ...
184 |     ((elem(12).COG(2)+diaBracHor/2+lBracW*cos(alpha))^2 +...
185 |     (elem(10).COG(2)+diaBracHor/2*sin(pi/6)+lBracW*cos(alpha)*sin(pi/6))^2 +...
186 |     (elem(10).COG(2)-diaBracHor/2*sin(pi/6)-lBracW*cos(alpha)*sin(pi/6))^2 ); % Ixx
187 | Iwp(2) = p.numCol*Icol + 2*elem(2).COG(1)^2*elem(2).A + ...
188 |     elem(1).COG(1)^2*elem(1).A + ...
189 |     pi*p.diaBracing^2/(4*sin(alpha))*2*(elem(12).COG(1)^2 +...
190 |     (elem(10).COG(1)+diaBracHor/2*cos(pi/6)+lBracW*cos(alpha)*cos(pi/6))^2+...
191 |     (elem(10).COG(1)-diaBracHor/2*cos(pi/6)-lBracW*cos(alpha)*cos(pi/6))^2); % Iyy
192 |
193 | BM = Iwp./ VdispTot;
194 | GM = BM - (mdata.COG(3)-COB(3)); % 1: transverse , 2: longitudinal
195 | mdata.GM = GM;
196 | % Calculate hydrostatic restoring matrix
197 | C = zeros(6,6);
198 | C(3,3) = rho*g*(elem(1).A + pi*p.diaBracing^2/(4*sin(alpha))*2) * p.numCol;
199 | C(3,4) = rho*g* elem(1).A*(elem(1).COG(2)+elem(2).COG(2)+elem(3).COG(2));
200 | C(4,3) = C(3,4);
201 | C(3,5) = -rho*g* elem(1).A*(elem(1).COG(1)+elem(2).COG(1)+elem(3).COG(1));
202 | C(5,3) = C(3,5);
203 | C(5,4) = -rho*g* (elem(1).A*(elem(1).COG(1)*elem(1).COG(2)+ ...
204 |     elem(2).COG(1)*elem(2).COG(2)+elem(3).COG(1)*elem(3).COG(2)));
205 | C(4,5) = C(5,4);
206 | C(4,6) = -rho*g*VdispTot*COB(1) + massTot*g*mdata.COG(1);
207 | C(5,6) = -rho*g*VdispTot*COB(2) + massTot*g*mdata.COG(2);
208 | C(4,4) = rho*g* VdispTot * GM(1);
209 | C(5,5) = rho*g* VdispTot * GM(2);
210 | end
```

D.3   Morison's Equation

```
1  | % Calculation of forces on slender elements by using Morison's equation
2  | % And viscous forces on heave plates
3  | % Written by Vetle Kallaak
4  |
5  | function [FtotwaveI,FtotwaveD, Atot_mor, Btot_mor, F_hp1, B_hp1] = ...
6  |     morison(first, waveW, eta, env, p, h_approx, COC, coord)
7  | movingStructure = true;
8  | % coord - Description of Morison elements
9  | % Rows: Morison element
10 | % Columns: (x,y,z) start and then end of Morison element (keep normal
11 | % vector positiv). Column 7: Diameter , 8: C_a, 9:C_D
12 |
13 | % Environment
14 | g = env.g; % Gravitational acceleration
15 | rho = env.rho; % Sea water density [kg/m^3]
16 | d = env.d; % Depth
17 | A = env.amp; % Wave amplitude
18 | beta = env.beta; % Wave angle
19 |
20 | % Calculate wave numbers and wave lengths
21 | Nfreq = length(waveW);
22 | k_all = zeros(Nfreq,1);
23 | for cc=1:Nfreq
24 |     w=waveW(cc);
25 |     k1 = w^2/g; %Wave number , assumed deep water
26 |     k_n=10;
27 |     k_n1 = k1;
28 |     while abs(k_n1 - k_n) > 0.00001
29 |         % Newton's method
30 |         k_n = k_n1;
31 |         k_n1=k_n - (w^2-k_n*g*tanh(k_n*d))/(-g*tanh(k_n*d)-k_n*g*d*(1/(cosh(k_n*d))^2));
32 |     end
33 |     k_all(cc,1)=k_n1;
34 | end
35 |
```

```matlab
36   FwaveI = zeros(6,Nfreq,length(coord(:,1))); % Wave inertia loads
37   FwaveD = zeros(6,Nfreq,length(coord(:,1))); % Wave drag loads
38   B_mor = zeros(6,6,Nfreq,length(coord(:,1))); % Damping matrix
39   A_mor = zeros(6,6,length(coord(:,1))); % Added mass matrix
40
41   for el=1:length(coord(:,1)) % Morison elements
42       D = coord(el,7); % Diameter of element
43       C_a = coord(el,8); % Added mass coefficient
44       C_D = coord(el,9); % Drag coefficient
45       % Calculate length of element
46       L = sqrt((coord(el,4)-coord(el,1))^2 + (coord(el,5)-coord(el,2))^2 + ...
47           (coord(el,6)-coord(el,3))^2);
48       if L == 0 % Heave plate
49           steps = 1; % Calculate only for center of heave plate
50           h = 0; % Element step length
51           if p.tilt ~= 0
52               n = [cos(p.tilt) 0 -sin(p.tilt)];
53               % Projection matrix
54               P = [n(2)^2+n(3)^2, -n(1)*n(2), -n(1)*n(3);
55                   -n(1)*n(2), n(1)^2+n(3)^2, -n(2)*n(3);
56                   -n(1)*n(3), -n(2)*n(3), n(1)^2+n(2)^2];
57           else
58               n = [0 0 0]; % Normal vector of element
59               P = zeros(3,3);
60               P(3,3) = 1; % Only want force in z-direction
61           end
62       else
63           steps = round(L/h_approx);
64           h = L/steps; % Element step length
65           % Calculate unit vector of element along x direction
66           n(1) = (coord(el,4)-coord(el,1))/L;
67           % Calculate unit vector of element along y direction
68           n(2) = (coord(el,5)-coord(el,2))/L;
69           % Calculate unit vector of element along z direction
70           n(3) = (coord(el,6)-coord(el,3))/L;
71           % Projection matrix
72           P = [n(2)^2+n(3)^2, -n(1)*n(2), -n(1)*n(3);
73               -n(1)*n(2), n(1)^2+n(3)^2, -n(2)*n(3);
74               -n(1)*n(3), -n(2)*n(3), n(1)^2+n(2)^2];
75       end
76       dFwaveInertia = zeros(6,Nfreq);
77       dFwaveDrag = zeros(6,Nfreq);
78       dB_mor = zeros(6,6,Nfreq);
79       dA_mor = zeros(6,6);
80       for j=1:steps % steps along element
81           % Coordinates to center of part
82           x = coord(el,1) + h*n(1)*(j-0.5);
83           y = coord(el,2) + h*n(2)*(j-0.5);
84           z = coord(el,3) + h*n(3)*(j-0.5);
85           % For rotation to translation and force to moment
86           S = [0, z-COC(3), -(y-COC(2));
87               -(z-COC(3)), 0, x-COC(1);
88               y-COC(2), -(x-COC(1)), 0];
89           for cc=1:Nfreq % All wave frequencies
90               w = waveW(cc); % Wave frequency
91               k = k_all(cc,1); % Wave number
92
93               % Wave velocity field, U=[u;v;w]
94               U = [w*A*(cosh(k*(z+d))/sinh(k*d))*exp(-1i*k*(x*cos(beta)+...
95                   y*sin(beta)))*cos(beta);
96                   w*A*(cosh(k*(z+d))/sinh(k*d))*exp(-1i*k*(x*cos(beta)+...
97                   y*sin(beta)))*sin(beta);
98                   1i*w*A*(sinh(k*(z+d))/sinh(k*d))*exp(-1i*k*(x*cos(beta)+...
99                   y*sin(beta)))];
100              % Linearization of drag term
101              if movingStructure
102                  K = 8/(3*pi) * abs(P*(U-1i*w*[eye(3) S]*eta(:,cc)));
103              else
104                  K = abs(P*U);
105              end
106              if L == 0 % Heave plate
107                  % Wave drag force
108                  dFwD = 0.5*C_D*rho*pi*D^2/4* K.*(P*U);
```

```matlab
109                  % Morison damping matrix, related to drag force
110                  dB = 0.5*C_D*rho*pi*D^2/4* K.* (P*[eye(3) S]);
111              else
112                  % Wave drag force
113                  dFwD = 0.5*C_D*rho*h*D* K.*(P*U);
114                  % Morison damping matrix, related to drag force
115                  dB = 0.5*C_D*rho*h*D* K.* (P*[eye(3) S]);
116                  % Wave inertia force and moment
117                  if first
118                      dFwI = 1i*w*rho*h*pi*D^2/4*(1+C_a)*(P*U);
119                      dFwaveInertia(1:3,cc) = dFwaveInertia(1:3,cc) + dFwI;
120                      dFwaveInertia(4:6,cc) = dFwaveInertia(4:6,cc) + (-S*dFwI);
121                  end
122              end % Type of element
123              % Wave drag force and moment on part
124              dFwaveDrag(1:3,cc) = dFwaveDrag(1:3,cc) + dFwD;
125              dFwaveDrag(4:6,cc) = dFwaveDrag(4:6,cc) + (-S*dFwD);
126              % Morison damping matrix for part
127              dB_mor(1:3,:,cc) = dB_mor(1:3,:,cc) + dB;
128              dB_mor(4:6,:,cc) = dB_mor(4:6,:,cc) + (-S*dB);
129          end % All wave frequencies
130          if L~=0 && first % Not heave plate and first iteration
131              % Morison added mass matrix, related to inertia force
132              dM = C_a*rho*h*pi*D^2/4 * (P*[eye(3) S]);
133              dA_mor(1:3,:) = dA_mor(1:3,:) + dM;
134              dA_mor(4:6,:) = dA_mor(4:6,:) + (-S*dM);
135          end
136      end % Parts
137      % Numerical integration along element
138      FwaveI(:,:,el) = dFwaveInertia;
139      FwaveD(:,:,el) = dFwaveDrag;
140      B_mor(:,:,:,el) = dB_mor;
141      A_mor(:,:,el) = dA_mor;
142  end % Morison elements
143
144  % Total wave inertia and drag force
145  FtotwaveI(:,:) = sum(FwaveI,3);
146  FtotwaveD(:,:) = sum(FwaveD,3);
147  % Total added mass and damping matrices
148  Btot_mor(:,:,:) = sum(B_mor,4);
149  Atot_mor(:,:) = sum(A_mor,3);
150  % Heave plate 1 force and damping for internal load calculations
151  F_hp1 = FwaveD(:,:,4);
152  B_hp1 = B_mor(:,:,:,4);
153  end % Function
```

D.4   Calculation of Internal Hull Loads

```matlab
1   % Calculate internal loads
2   % Written by Vetle Kallaak
3   function [numEl, Fp, Fc, F_Mhp1, FI, Fcs] = internalLoads(sesam, p, elem, env, waveW, ...
4       waveWhr, F_hp1, B_hp1, eta1, ADDMASS, DAMPING, etaM1, etaW, etaW_Bex, F_pot)
5   fprintf('Calculating internal loads...\n');
6   %% Read pressure from WADAM1.LIS
7   tic
8   [WaveDat, panels, Ppanels, PpanelsR, sections] = PanelsWadamLIS(sesam.wadam2); % ws
9   toc
10  % panels(panel,1:10) Geometry of panels
11  % 1:10 - PI, PANO, NX, NY, NZ, XC, YC, ZC, A, DIAG
12  % Ppanels(panel,1:6,wave) Pressure on panels
13  % 1:6 - PI, PANO, REAL, IMAG, ABS, PHASE
14  %% Geometry of reflected part of structure in Sesam,symmetry about xz-plane
15  panelsR = panels;
16  panelsR(:,4)=panelsR(:,4)*-1;
17  panelsR(:,7)=panelsR(:,7)*-1;
18  numEl = length(panels(:,1));
19
20  %% Loads
21  FpW = zeros(6,length(WaveDat(:,1))); % Pressure loads
22  FradW = zeros(6,length(WaveDat(:,1))); % Radiation loads Wadam
23  Frad = zeros(6,length(WaveDat(:,1))); % Radiation loads
24  FradWBex = zeros(6,length(WaveDat(:,1))); % Radiation loads Wadam with extra damping
25  FI = zeros(6,length(waveWhr)); % Inertia loads
```

```matlab
26  Fc = zeros(6,length(waveWhr)); % Restoring loads
27  F_Mhp1 = zeros(6,length(waveWhr)); % Morison drag on heave plate
28
29  % Cross section, moment point, now yz-plane
30  CS = [0 0 0];
31
32  for ii=1:length(WaveDat(:,1)) % All wave freq calculated in Wadam
33      % Pressure loads on panels
34      for nn=1:length(panels(:,1)) %All panels
35          % Only panels from colum 1
36      if panels(nn,6) >= ((elem(1).COG(1) - p.lhp - 0.5)*cos(p.tilt) + ...
37              -p.draft*sin(p.tilt))
38          % Forces
39          % F = n * area * P
40          F_p = panels(nn,9) * complex(Ppanels(nn,3,ii),Ppanels(nn,4,ii));
41          F_pR = panelsR(nn,9) * complex(PpanelsR(nn,3,ii),PpanelsR(nn,4,ii));
42          FpW(1,ii) = FpW(1,ii) + panels(nn,3) * F_p + panelsR(nn,3) * F_pR;
43          FpW(2,ii) = FpW(2,ii) + panels(nn,4) * F_p + panelsR(nn,4) * F_pR;
44          FpW(3,ii) = FpW(3,ii) + panels(nn,5) * F_p  + panelsR(nn,5) * F_pR;
45          % Moments
46          FpW(4,ii) = FpW(4,ii) - panels(nn,4)*F_p*(panels(nn,8)-CS(3))  - ...
47            panelsR(nn,4)*F_pR*(panelsR(nn,8)-CS(3)) + panels(nn,5)*F_p* ...
48            (panels(nn,7)-CS(2)) + panelsR(nn,5)*F_pR*(panelsR(nn,7)-CS(2));
49          FpW(5,ii) = FpW(5,ii) + panels(nn,3)*F_p*(panels(nn,8)-CS(3)) + ...
50              panelsR(nn,3)*F_pR*(panelsR(nn,8)-CS(3)) - panels(nn,5)*F_p* ...
51              (panels(nn,6)-CS(1)) - panelsR(nn,5)*F_pR*(panelsR(nn,6)-CS(1));
52          FpW(6,ii) = FpW(6,ii) - panels(nn,3)*F_p*(panels(nn,7)-CS(2)) - ...
53              panelsR(nn,3)*F_pR*(panelsR(nn,7)-CS(2)) + panels(nn,4)*F_p* ...
54              (panels(nn,6)-CS(1)) + panelsR(nn,4)*F_pR*(panelsR(nn,6)-CS(1));
55      end
56      end
57      w = WaveDat(ii,5);
58      % Radiation loads, part of pressure forces
59      % Forces for entire wet body
60      FradW(:,ii) = ADDMASS(:,:,ii)*(-w^2*etaW(:,ii)) ...
61          + DAMPING(:,:,ii)*(1i*w*etaW(:,ii)); % Wadam
62      FradWBex(:,ii) = ADDMASS(:,:,ii)*(-w^2*etaW_Bex(:,ii)) ...
63          + DAMPING(:,:,ii)*(1i*w*etaW_Bex(:,ii)); % Wadam with extra damping
64      Frad(:,ii) = ADDMASS(:,:,ii)*(-w^2*etaM1(:,ii)) ...
65          + DAMPING(:,:,ii)*(1i*w*etaM1(:,ii)); % True
66  end % All wave freq calculated in Wadam
67  % Excitation loads
68  Fexc = FpW + FradWBex;
69
70  % Interpolate pressure forces for better resolution
71  for r = 1:6
72      Fp(r,:) = interp1(waveW,FpW(r,:),waveWhr,'spline');
73  end
74
75  for ii = 1:length(waveWhr) % For all frequencies
76      % Inertia forces
77      % Only column 1
78      w = waveWhr(ii); % Wave freq
79      mz_g=0; % Mass moment for colum 1
80      for e=[1 4 19 22] % NB! only want colum, hp, WT, ballast
81          fix = elem(e).mass * -w^2 * ...
82              (eta1(1,ii)+eta1(5,ii)*elem(e).COG(3)-eta1(6,ii)*elem(e).COG(2));
83          fiz = elem(e).mass * -w^2 * ...
84              (eta1(3,ii)+eta1(4,ii)*elem(e).COG(2)-eta1(5,ii)*elem(e).COG(1));
85          FI(1,ii) = FI(1,ii) + fix;
86          FI(3,ii) = FI(3,ii) + fiz;
87          FI(5,ii) = FI(5,ii) + fix*(elem(e).COG(3)-CS(3))...
88              - fiz*(elem(e).COG(1)-CS(1));
89          mz_g = mz_g + elem(e).mass*elem(e).COG(3); % Mass center z
90      end
91      % Restoring loads (as external force)
92      Fc(1,ii) = 0; % -C(1,1)*eta1(1,i); Neglect!
93      % C33, C34, C35
94      Fc(3,ii) = -env.rho*env.g*elem(1).A *...
95          (eta1(3,ii)+eta1(4,ii)*elem(1).COG(2)-eta1(5,ii)*elem(1).COG(1));
96      % C53, C54, C55
97      z_b = (elem(1).Vwet*(-p.draft+p.hhp)/2+elem(4).Vwet*elem(4).COG(3)) ...
98          / (elem(1).Vwet+elem(4).Vwet); % Buoyancy center z
```

```matlab
 99         Fc(5,ii) = -Fc(3,ii)*(elem(1).COG(1)-CS(1)) - ...
100             (env.rho*env.g*(elem(1).Vwet+elem(4).Vwet)*z_b-mz_g*env.g)*eta1(5,ii);
101         % Morison drag loads on heave plate
102         % Moments are about global origin
103         F_Mhp1(:,ii) = F_hp1(:,ii) - B_hp1(:,:,ii)*(1i*w*eta1(:,ii));
104     end % Wave freq
105
106     % External forces
107     Fex = Fp + Fc + F_Mhp1;
108     % Forces at cross section from part A:
109     Fcs = (FI - Fex);
110     toc
111     fprintf('Internal forces calculated. numEl = %d\n', numEl);
112     end
```

Kallåk, Vetle

Parametric Design and Analysis of Wave-Induced Responses of a Semi-Submersible Floating Wind Turbine Platform

NTNU
Norwegian University of
Science and Technology